

INVESTIGATION OF STRUCTURAL AND MAGNETIC PROPERTIES OF NICKEL DOPED MANGANESE FERRITE NANOPARTICLES

M.Sc. (Physics) Project Dissertation

Submitted By

Shantadurga R. Desai

Richesh M. Parab



**School of Physical and Applied Sciences,
Goa University,
Taleigao Plateau, 403206**

DECLARATION

We hereby declare that this project thesis entitled “INVESTIGATION OF STRUCTURAL AND MAGNETIC PROPERTIES OF NICKEL DOPED MANGANESE FERRITE NANOPARTICLES” completed as a part of M.Sc. Physics course is our original work and that it has not been submitted to any other University or Institution for the award of any Degree, Diploma, Associateship and fellowship or any other similar title to the best of my knowledge.

Date:

Miss. Shantadurga Desai

(Candidate)

Mr. Richesh Parab

(Candidate)

CERTIFICATE

This is to certify that the project entitled

INVESTIGATION OF STRUCTURAL AND MAGNETIC PROPERTIES OF NICKEL DOPED MANGANESE FERRITE NANOPARTICLES

being submitted by

Shantadurga R. Desai

Richesh M. Parab

in the partial fulfilment of the degree of

MASTER OF SCIENCE IN PHYSICS

Goa University

is a record of their own work carried out in the department

Project Supervisor

Dr. Pranav Naik

Programme Director

Dr. Sudhir Cherukulappurath

ACKNOWLEDGEMENT

We are immensely pleased to place on record profound gratitude and heartfelt thanks to our project guide and mentor **Dr. Pranav P. Naik**, Assistant professor, Department of Physics, Goa University, for his guidance and constant support during our research work. He provided us with the necessary guidance for the successful completion of our research work. It was a privilege to work under his supervision.

We would like to express our thanks for the technical support received from the Department of Chemistry, for allowing us to use XRD equipment. We are grateful to the Director of IIT Roorkee, for providing us with VSM data. We would also like to thank our Dean **Dr. Kaustubh Priolkar**, Programme director **Dr. Sudhir Cherukulappurath**, Faculty members, and laboratory assistants for being very kind and cooperative to us throughout our project work and to all the people who contributed directly and indirectly to the completion of this project.

CONTENTS

DECLARATION	i
CERTIFICATE	ii
ACKNOWLEDGEMENT.....	iii
CONTENT	iv
ABSTRACT.....	1
CHAPTER I: INTRODUCTION	2
1.1 Introduction	2
1.2 Spinel Ferrite	3
1.3 Applications of ferrites	5
1.4 Nickel Manganese Ferrites	7
1.5 Literature Review	9
1.6 References	19
CHAPTER II: METHODS OF MATERIAL PREPARATION.....	23
2.1 Co-precipitation method	23
2.2 Spray pyrolysis method	24
2.3 Hydrothermal synthesis method	25
2.4 Sol-gel method	27
2.5 High Energy Ball Milling Method	28
2.6 Thermal Decomposition Method	29
2.7 Ultrasonic (Sono-chemical) Method	30
2.8 Micro-emulsion	32
2.9 Combustion Method	33
2.10 References	38
CHAPTER III: CHARACTERISATION TECHNIQUES	41
3.1 X-ray Powder Diffraction	41
3.1.1 Introduction	41
3.1.2 Basic Principle of X-ray Diffraction	41
3.1.3 Instrumentation	43
3.2 Scanning Electron Microscope (SEM)	45
3.2.1 Introduction	45

3.2.2 Basic Principle of SEM	45
3.2.3 Instrumentation	46
3.3 Energy-dispersive X-ray spectroscopy	48
3.3.1 Introduction	48
3.3.2 Basic Principle Of EDS	48
3.3.3 Instrumentation	49
3.4 Vibrating Sample Magnetometer (VSM)	52
3.4.1 Introduction	52
3.4.2 Basic Principle of VSM	52
3.4.3 Instrumentation	53
3.5 References	56
CHAPTER IV: RESULTS AND DISCUSSION	58
4.1 X-ray diffraction	58
4.2 Scanning Electron Microscope Analysis	67
4.3 Energy-dispersive X-ray Spectroscopy Analysis	70
4.4 Vibrating Sample Magnetometer Analysis	75
4.5 References	80
CHAPTER V: CONCLUSION	86

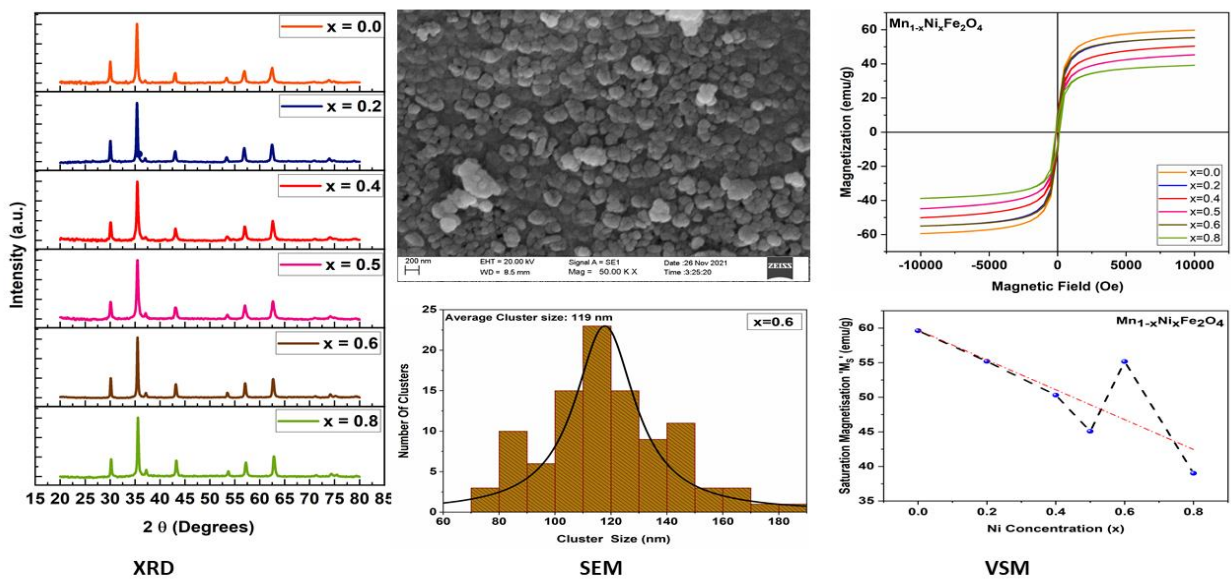
LIST OF ILLUSTRATIONS

Figure 1.1 - Structure of magnetic spinel ferrite showing tetrahedral sites (yellow), octahedral sites (green), and oxygen atoms (red) units (a). Unit cell structure of (b) normal spinel ferrite, and (c) inverse spinel ferrite	4
Figure 2.1 - Synthesis of spinel ferrite nanoparticles by co-precipitation method	23
Figure 2.2 - Set-up of Spray pyrolysis technique	25
Figure 2.3 - Schematic Representation of Hydrothermal technique	26
Figure 2.4 - Synthesis of Nano-ferrite by Sol-gel method	27
Figure 2.5 - Schematic Representation of Ball milling Method	28
Figure 2.6 - Setup of Ultrasonic technique	31
Figure 2.7 - Schematic representation of Micro emulsion method	32
Figure 2.8 - Flowchart for the synthesis of spinel ferrite by Combustion method	35
Figure 2.9 - Glimpses of the Sample preparation process	37
Figure 3.1 - X-ray Diffractometer	41
Figure 3.2 - Formation of Cone	42
Figure 3.3 - Diffracted cones of each plane of powder crystalline samples and their Photograph.	43
Figure 3.4 - Carl Zeiss Scanning Electron Microscope Setup.....	45
Figure 3.5 - Components of SEM	47
Figure 3.6 - Ejection of Core electrons in EDS	48
Figure 3.7 - EDS Detector Components	50
Figure 3.8 - Lakeshore VSM Setup	52
Figure 3.9 - Components of VSM	53
Figure 4.1 - Rigaku X-ray Diffractometer	58
Figure 4.2 - X-ray Diffraction patterns of $Mn_{1-x}Ni_xFe_2O_4$ (a) $x=0$ (b) $x=0.2$ (c) $x=0.4$ (d) $x=0.5$ (e) $x=0.6$ (f) $x=0.8$	59
Figure 4.3 - Lattice Constant as function of Nickel concentration.....	63
Figure 4.4 - Crystallite Size as a function of Ni Concentration	63
Figure 4.5 - Strain as a function of Ni Concentration	63
Figure 4.6 - X-ray density as a function of Ni Concentration	65
Figure 4.7 - Mass density as a function of Ni Concentration	65
Figure 4.8 - Porosity as a function of Ni Concentration.....	65
Figure 4.9 - Carl Zeiss Scanning Electron Microscope	67

Figure 4.10 - SEM micrographs and their respective histograms of $Mn_{1-x}Ni_xFe_2O_4$ [(a) $x = 0.0$, (b) $x=0.2$, (c) $x=0.4$, (d) $x=0.6$ and (e) $x=0.8$]	68
Figure 4.11 - Variation of Cluster size with increasing Ni concentration	69
Figure 4.12 - EDX image and EDX spectrum of $Mn_{1-x}Ni_xFe_2O_4$ ($x = 0.0, 0.2, 0.4, 0.5, 0.6, 0.8$) nanoparticles	70
Figure 4.13 - Lakeshore Vibrating sample magnetometer	75
Figure 4.14 - Plots of Magnetic Hysteresis loops of $Mn_{1-x}Ni_xFe_2O_4$ ($x = 0.0, 0.2, 0.4, 0.5, 0.6, 0.8$) nanoparticles	76
Figure 4.15 - Variation of Saturation Magnetization (M_s) with Nickel concentration (x).....	76
Figure 4.16 - Variation of Magnetic moment with Nickel concentration (x)	76
Figure 4.17 - Variation of Coercivity with Nickel concentration (x)	78
Figure 4.18 - Variation of Retentivity with Nickel concentration (x)	78
Table 4.1 - Diffraction angle, Miller indices, interplanar spacing and lattice constant of all the prepared samples of $Mn_{1-x}Ni_xFe_2O_4$ [(a) $x = 0.0$, (b) $x=0.2$, (c) $x=0.4$, (d) $x=0.6$ and (e) $x=0.8$].....	60
Table 4.2- Structural parameters of $Mn_{1-x}Ni_xFe_2O_4$ ($x=0.0, 0.2, 0.4, 0.5, 0.6, 0.8$) samples.....	62
Table 4.3 - Cluster size of $Mn_{1-x}Ni_xFe_2O_4$	69
Table 4.4 - Calculated and Observed Atomic percentage of Mn, Fe, O in $Mn_{1-x}Ni_xFe_2O_4$ [(a) $x = 0.0$, (b) $x=0.2$, (c) $x=0.4$, (d) $x=0.6$ and (e) $x=0.8$]nanoparticles using EDS data.....	70
Table 4.5 - Magnetic properties: Saturation Magnetisation (M_s), Retentivity (M_r), Coercivity (H_c), Magnetic Moment(μ), Squareness Ratio (M_{rs}) of $Mn_{1-x}Ni_xFe_2O_4$ ($x = 0.0, 0.2, 0.4, 0.5, 0.6$ & 0.8) nanoparticles	77

ABSTRACT

The present work describes the successful synthesis of spinel magnetic ferrite $\text{Mn}_{1-x}\text{Ni}_x\text{Fe}_2\text{O}_4$ ($x = 0.0, 0.2, 0.4, 0.5, 0.6 \& 0.8$) nanoparticles via the combustion method using metal salts such as Manganese (II) Acetate, Nickel (II) Nitrate, Ferric Nitrate along with NTA as a complexing agent and Urea as Combustion Fuel. The structural and magnetic properties were studied using X-ray diffraction (XRD), Scanning electron microscopy (SEM), Energy-dispersive X-ray spectroscopy (EDS), and Vibrating sample magnetometer (VSM) techniques. The XRD results reveal that Nickel substituted Manganese ferrite possesses a well-crystalline pure cubic spinel phase with Lattice parameter ranging from 8.4125 Å to 8.3645 Å. The lattice parameter showed a fairly linear dependence on nickel concentration in accordance with Vegard's law. In the case of crystallite size, a random trend was observed with overall crystallite size increasing with Ni doping. Crystallite size and Crystallite strain were found to exhibit an inverse trend of each other. A similar inverse trend was obtained from mass density and porosity plots. The x-ray density was found to be higher than the mass density. Scanning electron microscope images indicated that the samples consist of nearly spherical-shaped nanoparticles with fairly uniform size and narrow size distribution. The elemental composition of Mn, Ni, Fe, and O was confirmed by the EDS analysis. Magnetic measurements showed decrease in saturation magnetisation (M_s) with increasing nickel concentration. The behaviour of Magnetic moment was analogous to saturation magnetization. The coercivity values indicated that the prepared samples have soft ferrite nature and the squareness ratios indicated that the particles were heading towards single domain magnetic nanoparticles.



SOME MAJOR RESULTS

CHAPTER I: INTRODUCTION

1.1 Introduction

Since recent times, spinel ferrite nanoparticles are found to be of pronounced interest for many researchers due to their exceptional properties which make them promising candidates for potential applications in the electronic and biomedical industry [1]. The structural, optical, electronic and magnetic properties of the spinel ferrites are significantly improved in the nanoscale scale range due to its rise in surface to volume ratio and decrease in the crystallite size. Spinel ferrites have been extensively explored to produce nanoparticles having the qualities of an ideal drug delivery agent. The core drive of targeted drug delivery is to spot and carry a drug directly to the affected areas of human tissue and treat it effectively without any side effects [2]. In biomedicine, Nanomedicine is found to effectively detect and treat cancer. The focus of Nanomedicine is to provide an effective way in the health sector so as to get rid of dangerous diseases [3]. Spinel ferrites have also brought a revolutionary change in the electronics sector about building more compact and efficient devices [1,4]. These uses are based upon important properties of ferrites: high saturation magnetisation and electrical resistivity, low coercivity and electrical losses and great chemical stability. In turn, these factors are governed by the distribution of cations over the two sites and the electronic configuration between tetrahedral and octahedral sites within the crystalline structure [4]. The cationic distribution in spinels is determined by various factors such as the degree of distortion of the crystal structure, electrostatic energy (Madelung energy), which affects the electrical charge distribution. In simpler terms, octahedral sites (larger coordination number) should be occupied by cations with higher electrical charge and tetrahedral sites should be occupied by cations with smaller valency for greater stability. Crystal field stabilization energy also accounts for cation preference site which is responsible for the geometry of the d orbitals and its arrangement within the crystal structure. Thus, the fundamental understanding of crystal chemistry in Spinel ferrite nanoparticles is the very essential and appropriate selection of the synthesis route becomes crucial in obtaining desired properties [4]. An incredible property of spinel structure is that it is able to form an exceptionally wide-ranging variety of total solid solutions which indicates that the configuration of a particular ferrite can be intensely altered, while the basic crystalline arrangement rests the same. This composition has different characteristics as compared to pure ferrite. Manganese ferrites doped with Nickel establishes an important class of ceramic materials that has been under exploration for years [5]. Manganese ferrite $\{MnFe_2O_4\}$ is initially considered to be an inverse spinel, but later found to be 80% normal and 20% inverse structure [6]. The replacement of the Nickel ions with Manganese ions can increase magnetisation in ferrites owing to the larger magnetic moment and different

distribution of cation into the spinel structure, which has also lead to a higher electrical resistivity that is essential for high frequencies applications [7].

Supercapacitance has gained much attention because of its ability in providing high power density and energy densities, which makes them potential candidate to replace batteries in near future. Binary metal oxide ferrites (MFe_2O_4) have been extensively studied for supercapacitor applications including MFe_2O_4 ($M = Fe, Co, Ni, Mn, Cu, Zn$), $NiCo_2O_4$, $MnFe_2O_4$, and $CoFe_2O_4$. It is because of its ability to exhibit different redox states and electrochemical stability which helps in supercapacitance. It is expected that the ferrites could offer richer redox reactions, including contributions from both M and Fe ions (in MFe_2O_4) than those of the single-metal oxide. The cation distribution of the mixed ferrites significantly affects their surface properties, making them catalytically active. Therefore, it is worthwhile investigating suitable ferrite which would provide optimum properties for supercapacitor applications [8].

1.2 Spinel Ferrite

Spinel ferrite is made up of composite oxide crystal structure having a face-centred cubic core and having a unit formula of $\{AFe_2O_4\}$. These ferrites can be formed from the mixture of a trivalent cation (Fe^{3+}) and another divalent metallic cation, like either a transition or post-transition metal cation ($A = Mn, Ni, Zn, Mg, Co$ or the mixture of such ions). With dissimilarities in charge state, chemical nature and stabilization energy, these cations may be arranged in accordance to two different crystallographic sites which are tetrahedral sites and octahedral sites placed between the cations and adjacent oxygen ions. Although having a simple structure, the spinel ferrite consists of a huge number of atoms or ions related with each lattice point in its Bravais lattice. One unit-cell of spinel structured compound consists of eight formula units of AB_2O_4 determined by the distributions of cations in the voids whose occupancy is partial. In such a crystal structure, two types of cations occupy the tetrahedral and the octahedral sites in an FCC lattice made by anions i.e. O atoms. Since one-unit cell has Eight FCC structures, a total of 32 octahedral voids and 64 tetrahedral voids are available per unit cell. Because of stoichiometry, the octahedral voids have half of the occupancy while tetrahedral voids have 1/8 the occupancy by the cations [3]. The magnetic moments of cations occupying tetrahedral sites are opposite concerning the cations occupying the octahedral sites and hence these are essentially ferrimagnetic materials with a Curie transition and soft magnet like behaviour.

The cubic spinel structure can be classified, depending on the distribution of cations in the octahedral and tetrahedral voids, as:

Normal spinel ferrites

Inverse spinel ferrites and

Mixed spinel ferrites

and are depicted in figure 1.1

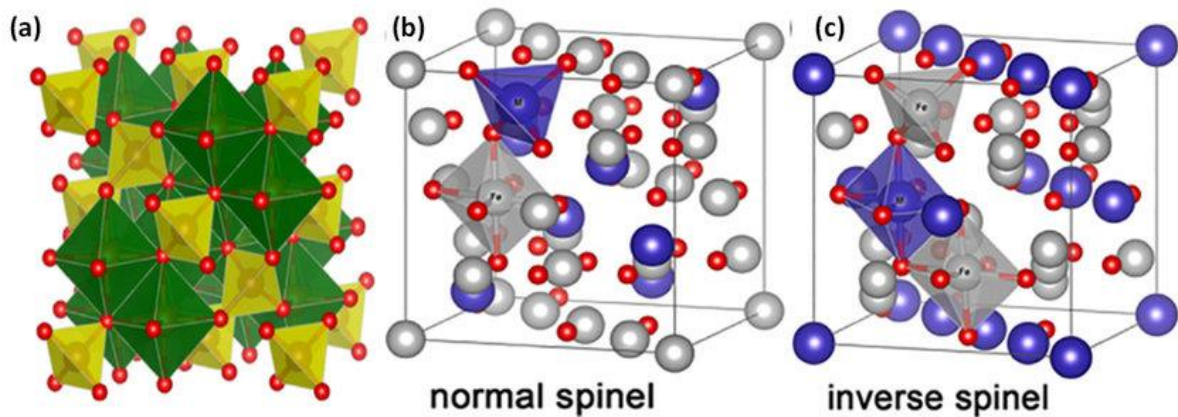


Figure 1.1 - Structure of magnetic spinel ferrite showing tetrahedral sites (yellow), octahedral sites (green), and oxygen atoms (red) units (a). Unit cell structure of (b) normal spinel ferrite, and (c) inverse spinel ferrite ^[9,10]

1) Normal Spinel Ferrites

The chemical formula of Normal spinel ferrite can be understood as $A_{\text{tetrahedral}}(B_2)_{\text{octahedral}}O_4$. In these compounds, all the A atoms occupy the tetrahedral sites (1/8 th occupancy) while all the B atoms occupy the octahedral sites (1/2 the occupancy). Thus, in the unit cell of the spinel structure, a total of 8 tetrahedral sites are engaged by divalent ions and 16 Octahedral sites are engaged by Trivalent ions. Ferrites that show normal spinel structure are $CoAl_2O_4$, $ZnFe_2O_4$, $MgAl_2O_4$, etc.

2) Inverse Spinel Ferrites

The chemical formula of Inverse spinel ferrite can be understood as $A_{\text{Tetrahedral}}(AB)_{\text{Octahedral}}O_4$. in these compounds, all the A cations occupy the Octahedral sites while half of B cations occupy the tetrahedral sites and the remaining half of the B cations occupy the octahedral sites. Thus, the trivalent ions occupy 8 tetrahedral sites and 16 octahedral sites are shared equally among divalent and trivalent ions. Most of the iron-containing spinel show inverse spinel structure such as $NiFe_2O_4$, Fe_3O_4 , $CoFe_2O_4$ etc.

3) Mixed Spinel Ferrites

When the cation distribution is mixed and both metal and Fe^{3+} cations are present on octahedral and tetrahedral sites then we obtain Mixed spinels. An inversion parameter $\bar{\alpha}$ is used to define the degree of inversion. It is represented by the formula $(\text{M}_x\text{N}_{1-x}\text{B}_2\text{O}_4)$ where M and N are metallic cations [3].

1.3 Applications of ferrites

1.3.1 Ferrites as Gas Sensors/Radiation Sensors

Increasing population and industrialization has led to pollution of ecology and hence need for effective gas sensors are essential in detecting leaks to avoid accidents. The large surface area of ferrites ensures that they can sense gases from ppm to ppb levels. These are two types based on the chemical properties of the gas to which the sensor is sensitive as oxidizing gas sensors (O_2 and Cl_2) and reducing gas sensors (H_2 , CO , NH_3 and CH_4). The oxidizing gas sensors cause the formation of acceptor surface states in the semi-conductive sensors and the reducing one causes the formation of donor surface states. The resistance of these sensors is a function of gas atmosphere, which is detected by exposing the ferrite surface to gas exposure. Ferrites find ample of applications in humidity sensors, temperature sensors and gas sensors. They find ample applications in UV sensors and robust optical sensors based nanostructures. They are applicable in ice detectors in aircraft wings, smoke detectors in industries and in protective layers that sense harmful radiations [11-13]

1.3.2 Ferrites as Adsorbents for Waste Water Treatment

With shrinking freshwater sources, the governments of all nations are imposing strict safety measures and rules for the disposal of toxic effluents from industries into water sources. Hence this field requires a lot of research. Ferrites are good adsorbents for a large category of pollutants especially toxic heavy metals as they interact by ion-exchange phenomena and help remove these heavy metals from solutions. Ion exchange may be defined as the exchange of ions between the substrate and the surrounding medium. The ion exchange technique can remove traces of ion impurities from water and process streams and give a product of desired quality. Since nano ferrites have a large surface-to-volume ratio, they adsorb the pollutants on the surface more effectively and enhance the purification process. The most useful ion exchange reaction is reversible, wherein the ion exchanger can be reused many times. Thus, the filtered nanoparticles can be desorbed of the pollutant and reused, which brings in the idea of recycling into the whole process [11-14].

1.3.3 Catalytic applications

Ferrites find applications as photo-catalysts and water purifiers due to their better selectivity and lifetime in chemical transformations. They can be used as precursors to cortex-catalysts and can be used as stereoselective catalysis surfaces. Some catalytic materials are sensitive to one particular orientation of atoms and some reactants are selectively reactive depending on the structure. Stereo selective catalysis is described as the process that proceeds with catalyst control but without the need to synthesize preformed chiral catalysts or ligands. The property of nanomaterials that make them useful as catalysts is the high reactivity on the surface ^[12,13].

1.3.4 Medical diagnostics and Biomedical applications

The property of ferrites to produce heat when placed in an alternating magnetic field can be used to target and burn down cancer cells. They can also be used as markers to be attached to cancerous cells which can be removed later from the body. Magnetic ferrites can be linked with carbohydrates and finds immense application for the detection of bacteria ^[13]. Magnetic ferrite nanoparticles can be used as MRI contrast agent for transplanted neural stem cell detection for imaging of biomedical cells. The controlled drug delivery and drug release can be performed with the use of ferrites. Ferrites also act like biocompatible coating for various medical applications ^[11-14].

1.3.5 Energy storage and Optical applications

Novel solar cells, smart windows based on photo-chrome effect or electrical magnetic orientation effect, window cells in classical solar cells to increase bandgap, better thermal insulation material and nanocrystalline hydrogen storage materials are a few energy storage related applications of ferrites. They are also used in the synthesis of special plastic lenses for graded refractive index optics, in antifogging and anti-reflective coatings for spectacles and automobile windows, cost-effective coloured glasses for optical fibres ^[11-14].

1.3.6 Electronics

Nanophosphors find applications in flat-screen panel displays and high-definition television. Single-electron nanoparticle quantum dots, efficient voltage-controlled LED's with tuneable output, optical switches and fibres based on non-linear behaviour, single-electron tunnelling

transistors, electrically conducting nano-ceramics, capacitive materials for dynamic random-access memories etc. are some of the other innovative electronic applications of ferrites [11-14].

1.3.7 Protective coatings

Ferrites can act as cost-effective corrosion protection material, elimination of pollutants in catalytic converters utilizes large surface area of nanomaterials, they are also used in scratch-resistant coatings for sensitive devices, rust-resistant, dirt-resistant clothing and germ-resistant films for industrial purposes [11-13]

1.4 Nickel Manganese Ferrites

The properties of the ferrites can be tuned by varying the cation substitution and their distribution among the tetrahedral site and octahedral site. In Ni²⁺-substituted MnFe₂O₄, the Ni²⁺ ions occupy octahedral (B) sites and Mn²⁺ ions occupy tetrahedral (A) and octahedral (B) sites. These samples usually have good crystallinity [15]. Besides the pure nickel ferrite, NiFe₂O₄, the nickel substituted ferrites Ni_{1-x}Me_xFe₂O₄ are also of great interest due to the increase of some characteristics such as magnetisation and/or electrical resistivity offered by the new chemical composition. Doping nickel with Manganese ferrites can improve magnetisation of ferrites due to the larger magnetic moment and/or different cation distribution into the spinel structure, and it can also lead to a higher electrical resistivity that is critical for high frequency applications [16].

Mn-Ni Spinel ferrites are very interesting and technologically important materials. Many researchers are extensively studying Mn-Ni ferrites in nano form because their structural, magnetic and dielectric properties can be altered depending upon composition, particle size and sintering temperature [17]. These ferrite nanoparticles of Mn Ni ferrites in their different phases are being currently explored for their diverse range of applications such as in magnetic fluids, magnetic recording media, microwave devices, magnetic resonance imaging, magnetic carriers for drug targeting, magnetic storage media, environment protection, catalysis, clinical diagnosis and chemical sensors. The attention which is being focused on their preparation and characterization is well deserved as they have the capability to exhibit certain superior properties like superparamagnetism [7,18]. Superparamagnetism is a form of magnetism which appears in small ferromagnetic or ferrimagnetic nanoparticles. In sufficiently small nanoparticles, magnetization can randomly flip direction under the influence of temperature. The typical time between two flips is called the Neel relaxation time. The main difference between paramagnetic and superparamagnetic

particles is that the magnetic moments of paramagnetic atoms can have almost any orientation in the space, while the superparamagnetic particles have the most stable states (directions) associated with the axes of easy magnetization due to magnetic anisotropy of crystalline particles or due to their shape anisotropy.

The secondary phase sometimes obtained in Mn-Ni ferrites, (α -Fe₂O₃), is the most stable iron oxide, with n-type semiconducting properties under ambient conditions, has been investigated as chemical gas sensors. The system of nickel ferrites is suitable for hyperthermia applications owing to their soft magnetic nature. hyperthermia is defined as Abnormally high body temperature. This may be caused as part of treatment, by an infection, or by exposure to heat. super paramagnetic particles exactly align themselves to the applied field (if you trace the hysteresis loop there is no loss). suppose these particles are deposited on damaged cell and then you subject this part of the body to alternating magnetic field. So as the magnetic field direction changes, the direction of the spins will also change but being very close to each other, due to friction the temperature of the surrounding will raise and it will destroy the damaged cell.

A low value of the coercive field is desirable since it indicates minimum energy loss during the switching of the magnetic field. These particles form the basis of Ferro fluids which have important applications in rocket propulsion and optical filters ^[19].

All the Nano sensors are highly accessible, thermally stable for sundry gases. In particular, nickel ferrite is an excellent material for sensing the gases such as LPG, H₂S, methane, Cl₂ and NH₃ ^[21] these Mn-Ni ferrites can also be used as microwave absorbers. These ferrites can be exploited as good optical limiters ^[22,23].

Compared with CoFe₂O₄ ferrite anodes, MnFe₂O₄ and NiFe₂O₄ ferrite anodes show lower cost and less toxicity. Among them, nickel-based and manganese-based oxides have received increased attention as very promising anode materials for Li-on batteries because of their high theoretical capacity, low cost, non-toxicity, and improved safety ^[24].

1.5 Literature Review

Sharareh Mirzaee et. Al. [5] synthesized the manganese doped nickel ferrite nanoparticles by the modified co-precipitation method. The structure and magnetic properties of the as synthesized samples have been studied by X-ray diffraction (XRD), Field emission electron microscopy (FESEM), Fourier transform infrared spectroscopy (FT-IR) and Vibrating sample magnetometer (VSM). The results indicated that the preferred orientation peak of the XRD patterns changed due to different ions distribution and strain in the spinel structure. adding the Mn^{2+} cations to the reaction medium after the formation of the nucleation centers could change the ion vibrations in the spinel structures and The magnetic measurement showed that the M_s value of the samples decreased with increasing the manganese ion concentration because of the Mn ion distribution in the spinel sites and strain in the structure. EDX and the elemental mapping analysis revealed the presence of all chemical elements in the samples (Mn, Fe, Ni, O) without any additional element.

Kumar Ranjit .et al [7] have investigated the influence of Mn substitution in $NiFe_2O_4$ ferrite nanoparticles ($Mn-NiFe_2O_4$), which were synthesized by the auto-combustion method at different fuel ratios (50%, 75% and 100%) and the Characterisation techniques used were X-ray powder diffraction, scanning electron microscopy and transmission electron microscopy, VSM. The XRD measurements confirmed spinel structure. SEM, XRD and TEM clearly identified that the size of the particles is increased with the increase of fuel ratio due to the variation of reaction time. The crystallite size of the samples was found to increase with respect to increase in fuel ratio. From the EDX spectrum analysis the presence of the elements with atomic percentage of the ferrite nanoparticles was confirmed. The effect of particle size due to annealing temperature and fuel ratio of combustion process on the magnetic and dielectric properties of manganese substituted $NiFe_2O_4$ samples were analysed. VSM data analysis revealed that the saturation magnetization was computed and found to lie between 6 emu/g and 57 emu/g depending on the particle size of the studied sample. The coercivity was found to exhibit nonmonotonic behaviour with the particle size.

R. Kesavamoorthi and C. Ramachandra Raja [15] studied various properties of Mn^{2+} substituted Ni ferrite nanoparticles which were synthesized by sol-gel auto combustion method. The characterization studies include XRD, VSM, electron paramagnetic resonance (EPR), field emission scanning electron microscopy (FE-SEM) and FT-IR spectroscopy. From the XRD the usual cubic spinel phase was confirmed. The Lattice constant and average crystallite sizes found to be decreased with increasing Mn^{2+} ion concentration. The X-ray density values were found to decrease with an increase in Mn^{2+} concentration. VSM analysis revealed that the Mn substituted Ni ferrites were in a superparamagnetic state at room temperature. The coercivity, remanent magnetization and g value values were found to decrease with increasing Mn^{2+} concentration. FE-

SEM results showed that Mn^{2+} -substituted Ni ferrite were composed of agglomerated spherical particles.

Traian Florin Marinca et al ^[16] studied the Manganese substituted nickel ferrites, $\text{Ni}_{1-x}\text{Mn}_x\text{Fe}_2\text{O}_4$ ($x = 0, 0.3, 0.5$ and 0.7) by a combined method, heat treatment and subsequent mechanical milling. X-ray diffraction, differential scanning calorimetry and magnetic measurements were the Characterisation techniques used. The increase of the amount of the Mn^{2+} cation into the spinel structure leads to a significant expansion of the cubic spinel structure and lattice parameter. The crystallite size was found to decrease with increasing milling time up to 120 minutes, more rapidly for the nickel-manganese ferrites with a large amount of Mn^{2+} cations ($x=0.7$). The magnetisation of the ferrite was found to increase by introducing more manganese cations into the spinel structure, a behaviour assigned to the spin canted effect occurring at the grain surface. It was observed that the Mn^{2+} for Ni^{2+} substitution limits the magnetic disorder.

E. Ranjith Kumar et. Al. ^[17] studied the The structural and magnetic properties of manganese substituted nickel ferrite nanoparticles that were synthesized by auto-combustion and evaporation methods for $600\text{ }^\circ\text{C}$ and $900\text{ }^\circ\text{C}$. The characterisation techniques used were X-ray Diffraction (XRD), Scanning Electron Microscopy (SEM), and Transmission Electron Microscopy (TEM). The X-ray diffraction patterns indicated that the annealed samples were amorphous and resulted in the formation of Mn–Ni ferrite and the presence of $\alpha\text{-Fe}_2\text{O}_3$ as a secondary phase. The average crystallite sizes of the annealed samples were in the range from 25 to 65 nm for auto combustion method and 45 to 98 nm for evaporation method. The morphology and particle size of the annealed samples are examined by SEM and TEM which showed agglomeration of irregular morphology and open porosity of the samples. The annealing effect on the magnetic properties of Mn–Ni ferrites were analysed by using a Vibrating Sample Magnetometer (VSM). The impact of particle size, the saturation magnetization of Mn–Ni ferrite nanoparticles increased with increasing annealing temperature.

R.S. Pandav et. Al. ^[18] prepared the nanocrystalline $\text{NiFe}_{2-x}\text{Mn}_x\text{O}_4$ ($2 \geq x \geq 0$) ferrites by sol-gel method. X-ray diffraction patterns revealed that synthesized compounds are in single phase cubic spinel lattice for all the compositions. Using scanning electron microscopy, the surface morphology of all the samples was studied. The particle size measured from TEM and XRD confirmed the nanosized dimension of the as-prepared powder. From the energy dispersive X-ray analysis technique, the elemental analysis was carried out. Magnetic properties such as saturation magnetization, coercivity and remanence were studied as a function of increasing Mn concentration at room temperature. The saturation magnetization showed a decreasing trend with increase in Mn content. The decrease in magnetic saturation was reported with increase in Mn^{3+} substitution due to

the fact that replacement of Fe^{3+} by less magnetic Mn^{3+} ions causes a demagnetizing field. The observed and calculated values of magnetic moment depicted large variation which was due to canting of spins at octahedral site.

Akash et al. [19] reported the synthesis of Mn-doped nickel ferrite having the generic formula $\text{Ni}_{1-x}\text{Mn}_x\text{Fe}_2\text{O}_4$ ($x = 0.05, 0.10, 0.15$) through the chemical co-precipitation technique. The characterisation techniques used were x-ray diffraction (XRD), Raman spectroscopy, dc magnetization studies and Mössbauer spectroscopy. XRD measurements confirmed the formation of a pure spinel phase with particle size homogeneity. The investigation of the Williamson-Hall plot indicated the presence of strain in all the samples. Dc magnetization studies revealed the sample possessed negligible coercivity coupled with ferrimagnetic nature. The samples that possessed low magnetocrystalline anisotropy along with ferrimagnetic behaviour were found to be a potential candidate for biomedical industries.

Prashant Bhimrao Koli et. al. [20] prepared the inverse spinel nanocrystalline pure and doped nickel ferrite particles by the co-precipitation method. The preparation of thick films of both pure and doped nickel ferrite nanoparticles was done by coating the material on glass substrate via screen printing method. confirmation of cubic, crystalline nickel ferrites was done using XRD. The scanning electron microscopy revealed nanosized, cubic nanoparticles of nickel ferrite, and their morphology was investigated. EDX was used to comprise elemental composition for pure and doped ferrites and data obtained attested the formation of pristine and doped nickel ferrite nanocrystals. TEM images investigated surface morphology, crystal structure of nickel ferrites.

Maisnam et. Al. [21] prepared ferrite sample with the representative formula $\text{Li}_{0.45}\text{Mn}_{0.1}\text{Ni}_{0.1}\text{Fe}_{2.35}\text{O}_4$ by microwave processing. The sample so prepared was found to have lower lattice constant, higher density compared to that of the conventionally sintered sample of same composition. XRD pattern for the sample showed the formation of well-defined single-phase spinel structure. the SEM photomicrographs obtained on the fractured surfaces of the Conventionally Sintered samples(CS) and Microwave Sintered samples(MS) revealed that MS sample shows the microstructures to consist of relatively smaller and more uniform grains in comparison to CS sample and the average grain size was greatly reduced. Magnetic properties like Curie temperature (T_c) and saturation magnetisation ($4\pi M_s$) were found to be slightly lower for the MS sample. The slight reduction in the saturation magnetisation was attributed to the lowering of magnetic moments of the ferrite samples, as result of the lesser loss of oxygen or Lithia during sintering. Also, the reason for lower magnetization values was attributed to the smaller grain size of the sample, and possibly containing lesser domain walls.

Yali Qi et. Al. [22] synthesized magnetic nanocomposite of $\text{Ni}_x\text{Mn}_{1-x}\text{Fe}_2\text{O}_4$ /carbonized chaff ($x = 0.3, 0.5, \text{ and } 0.7$) via the co-carbonization and hydrothermal method. The microstructure, morphology, complex permittivity and permeability, and microwave absorbing properties were systematically studied by X-ray diffraction, scanning electron microscopy, and a vector network analyser. Compared to the pure $\text{Ni}_{0.5}\text{Mn}_{0.5}\text{Fe}_2\text{O}_4$ NPs, the $\text{Ni}_{0.3}\text{Mn}_{0.7}\text{Fe}_2\text{O}_4$ /carbonized chaff- N_2 composite exhibited an optimal microwave absorption property at 4 mm as the mass per cent of carbonized chaff was 10 wt %, the maximum reflection loss of which can reach -14.58 dB at 1.91 GHz with the -10 dB frequency bandwidth in the range of 1.46– 2.41 GHz. The enhanced electromagnetic wave absorbing performance was ascribed to the good synergistic effect among laminated structures, better impedance matching condition, strong natural resonance loss, Debye dipolar relaxation to some extent, and so forth. The study provided a novel way to prepare easily degradable, environment-friendly, and high-efficiency electromagnetic wave absorbers by utilizing the structural property of renewable biomaterials.

S. Yuvaraj et. Al. [23] adopted the Chemical co-precipitation method to obtain phase pure nickel substituted manganese ferrites using chloride precursors at temperatures around 100°C . XRD studies revealed the phase purity and crystallite size reduction with increasing concentration of nickel ions. The reduced crystallite size was confirmed by the SEM analysis. Optical bandgap values were found to increase with the increase in concentration and decrease in grain size which was attributed to the quantum confinement effect observed due to the addition of nickel. The IR absorption bands depicted the presence of tetrahedral and octahedral complexes of the spinel ferrites. Optical limiting studies on these materials showed that the clamping threshold varied from 8 mW to 2.5 mW with addition of nickel in manganese ferrite indicating them to be exploited as good optical limiters.

Zailei Zhang et. al. [24] studied the solvothermal method and alternate filtration process to synthesize flexible and binder-free, free-standing $\text{Ni}_{0.5}\text{Mn}_{0.5}\text{Fe}_2\text{O}_4$ nanoparticles grown on oxidised graphene film (OGP film) and NMFO/ OGP coated polypropylene microporous film with high mechanical flexibility as anode materials. XRD patterns indicated formation of cubic spinel structure. SEM images indicated that most of the NMFO nanoparticles were agglomerated together due to the high surface energy of the nanoparticles. The TEM image of NMFO nanoparticles indicated that the particle size was in the range of 5–30 nm. The EDX spectrum of NMFO nanoparticles proved the presence of Ni, Mn, Fe, and O elements. The homogeneous distribution of all the four elements (Ni, Mn, Fe, and O) was found from the elemental mapping images. The atomic ratio of Ni, Mn, and Fe elements was found to be approximate 1: 1: 4 from the ICP-OES analysis. The introduced OGP could highly disperse NMFO nanoparticles, preventing their aggregation, buffering the volume

change, and providing efficient Li⁺ diffusion and electronic conduction pathway, which were also beneficial for better cycling stability and high rate performances.

Zhou Kaiwen et. Al. [25] prepared Li_{0.5x} Mn_{0.4} Ni_{0.6-x} Fe_{2+0.5x} O₄ (0.0 ≤ x ≤ 0.3) by calcining oxalates precursor method at 600 °C in air. The characterisation techniques used were thermogravimetry, differential scanning calorimetry, X-ray powder diffraction, scanning electron microscopy, and vibrating sample magnetometer. The XRD analysis showed that a cubic Mn_{0.4}Ni_{0.6}Fe₂O₄ with space group Fd-3m (227) was obtained by calcining Mn_{0.4} Ni_{0.6} C₂O₄·2FeC₂O₄·8.3H₂O over 600°C in air. Magnetic characterization indicated that magnetic properties of Li_{0.5x} Mn_{0.4} Ni_{0.6-x} Fe_{2+0.5x} O₄ depend on the composition and calcination temperature. the Mn_{0.4}Ni_{0.6} Fe₂O₄ calcined at 600 °C had the highest coercivity value, 130.32 Oe. The magnetic properties of these samples, in particular the specific saturation magnetizations (M_s) and coercivity (H_c), could be precisely tailored by controlling the composition as well as the calcination temperature.

Jian-Jun Gu et al [26] prepared Ni_{1-x} Mn_x Fe₂O₄ (x = 0.0, 0.25, 0.5, 0.75) nanowire arrays into nanopores of anodic aluminium oxide (AAO) template using the sol-gel technique. XRD technique was used to confirm the formation of single-phase nickel manganese ferrites. SEM and TEM images indicated that the nanowire arrays were composed of prolate spheroids with different crystal orientations. From the Magnetic measurements data, the saturation magnetization (M_s) of nickel ferrite nanowire arrays was found to be lower than that of bulk ones. But the M_s of the samples doped with Mn was found to be greater than that of bulk ones due to non-collinear structure in nanowires. On the other hand, with the increasing of Mn²⁺ ions concentration, the amount of Mn³⁺ derived from oxygenated Mn²⁺ increased then part of Fe³⁺ (5μ_B) on the B sites would be substituted by Mn³⁺(4μ_B) and resulted in the decrease of the magnetization. It was seen that increase in doping of Mn decreased the strength of exchange interactions.

B.V. Tirupanyam et al [27] conducted a systematic study on structural and magnetic properties of Ni_{1-x} Mn_x Fe₂O₄ (x=0.5, 0.6, 0.7) ferrite nanoparticles annealed at 800 °C using the Co-precipitation method. XRD, FE-SEM, VSM techniques were used for characterisation. XRD analysis revealed the presence of the Anti-ferromagnetic α-Fe₂O₃ phase and magnetic spinel phase in the XRD patterns. It was observed that both lattice parameter and crystallite size of spinel phase increases with increasing concentration of Mn²⁺ along with the amount of α-Fe₂O₃ phase. The saturation magnetization (M_s) was found to decrease while coercivity (H_c) increased with increasing Mn²⁺ ion concentration. The results were interpreted in terms of observed anti-ferromagnetic α-Fe₂O₃ phase, core-shell interactions and cation redistribution.

Rajesh Iyer et al. [28] synthesized Nano-sized $Mn_{1-x}Zn_x Fe_2O_4$ ($x = 0, 0.1, 0.3, 0.5, 0.6, 0.7, 0.9$) mixed ferrite samples using the co-precipitation technique. The autoclave was used to maintain a constant temperature and a constant pressure. The spinel phase formation and cation distribution were confirmed with X-ray analysis and the IR spectrum analysis in the ferrite samples. There was a gradual decrease in the particle size, Curie temperature and magnetization with the increasing Zn^{2+} ion doping, measured using magneto thermal gravimetric analysis (MTGA) and vibrating sample magnetometer (VSM). The lattice constant was found to be decreasing constantly till $x = 0.6$ and beyond this, an unusual slight increase in the lattice constant was found.

Chandana Rath et al. [29] studied the dependence of particle size on cation distribution, lattice parameter, and magnetic properties in nanosized Mn–Zn ferrite prepared by the Hydrothermal method. PXRD confirmed the formation of the ferrite phase in all samples. The hematite phase was detected in $MnFe_2O_4$. The average crystallite size and lattice constant were found to decrease with increasing Zn doping. From the M-H loop, it was found that M_s for Bulk Mn ferrite exhibits 80 emu/g whereas the nanoparticles of the same composition have M_s 53 emu/g. M_s and M_r increase with increasing Mn^{2+} concentration. Magnetization decreased monotonically with an increase in temperature. Magnetisation showed a cusp before T_c in some specific compositions instead of approaching zero which indicated the occurrence of an irreversible phase transition in this system.

P Mathur et al. [30] studied a series of $Zn_xMn_{1-x} Fe_2O_4$ ferrites, where $x = 0.1, 0.3, 0.5, 0.7$ and 0.9 , prepared by the citrate precursor technique. Both the normal pressing technique and the hot-pressing technique were used to prepare these ferrite samples. The XRD analysis revealed that the samples have a single-phase spinel structure with no unreacted constituents. With increasing Zn doping, lattice constants were found to gradually reduce from 8.534 to 8.406 Å for hot-pressed ferrites and from 8.611 to 8.428 Å for normally pressed ferrites, respectively. The average grain size was found to be ~70 nm in the normally pressed ferrites and ~90 nm in the hot-pressed ferrites. Cation distribution of different samples was determined. The variation of Saturation Magnetisation with the Zn^{2+} content was attributed to cation distribution and Neel's two sublattice model. Hot-pressed ferrites were found to have a considerably higher value of saturation magnetization as compared with the normally prepared ferrites of the same composition.

Ionel Chicina et al. [31] synthesized the nanocrystalline/nanosized mixed manganese–nickel spinel ferrite $Mn_{0.5}Ni_{0.5} Fe_2O_4$ by the classical ceramic method followed by mechanical milling. The Neel temperature of the ferrite was found to decrease with increasing milling time as a result of the structural disorder and it was found to be larger when compared with the manganese ferrite one and lower when compared with the nickel ferrite one. The saturation magnetization and spontaneous magnetization decreased with increasing milling time. The spontaneous magnetization was reduced

more severely as compared to saturation magnetization. This was attributed to the spin canted effect induced at the surface of the particle by the milling process.

Chicinaş et. Al. [32] synthesised the Mixed nickel-manganese ferrites, $Mn_{1-x}Ni_xFe_2O_4$ ($x=0, 0.3, 0.5, 0.7$) by ceramic route in the polycrystalline state. The reduction of particles size and refining of the crystallite size was obtained by mechanical milling of the ferrites. After 120 minutes of mechanical milling, the mean crystallite size was found to be 6-8 nm. The SEM investigation revealed the presence of micrometric particles alongside the nanometric ones. All the prepared mixed nickel-manganese ferrites were in a nanocrystalline/nanosized state after the mechanical milling procedure.

Sharifa et. Al. [33] conducted their study on various properties of Mn-doped $NiCuFe_2O_4$ prepared using the combustion technique. Two different samples $Ni_{0.5}Cu_{0.5}Fe_2O_4$ and $Mn_{0.35}Ni_{0.15}Cu_{0.5}Fe_2O_4$ were taken into consideration in this paper. The Diffraction peaks from XRD analysis confirmed that there is no other phase than the spinel phase in the patterns. Lattice constant and bulk density showed an increasing trend with Mn doping. Porosity follows the opposite trend of bulk density. From optical micrographs, it was found the average grain size increases with Mn doping at sintering temperature 1200C. The grain size was found to increase with increasing sintering temperature. Magnetisation studies revealed that saturation magnetisation increases with Mn concentration. Due to the substitution of Mn the real part of the complex permeability and relative quality factor increases whereas the relative loss factor decreases.

Abid Hussain et. Al. [34] studied Mn-doped $NiFe_2O_4$ nanoparticles synthesized by sol-gel method. The phase identification and estimation of cation distribution were the main focus of the paper. The X-ray diffraction lines confirmed the formation of a pseudo solid solution of the $Ni_{1-x}Mn_xFe_2O_4$ ferrites. With increasing Mn concentration, interatomic spacing d and lattice parameter were found to increase according to Vegard's law. The particle size which was determined using Scherer's equation showed an increasing trend from 23.86 nm to 38.30 nm with increasing Mn concentration. The oxygen parameter and inversion parameter were determined from the computer program in FORTRAN-77. The parameters indicated that the ferrites system belonged to a family of mixed or partially inverse spinel ferrites. Cation distribution was determined using the R-Factor method. The magnetic moment was found to increase with increasing Mn doping.

K. Sasikumar et. Al. [35] investigated the Structural, Optical, and Magnetic Properties of Mn-Doped Nickel Ferrite thin films which were prepared using the Jet Nebulizer Spray Pyrolysis Technique. The X-ray diffraction peaks confirmed the formation of the cubic spinel structure. The average crystallite size (D) was found to increase from 13 to 30 nm with increasing Mn concentration till

$x=0.6$. The FESEM micrographs exhibit randomly arranged plate-like and rice-like grains with thicknesses ranging from 20-150 nm. As the ferrite was doped with Mn, the ferrite crystallites were found to agglomerate. The expected elements such as Mn, Ni, Fe, and O were confirmed from EDX spectra. From the VSM results, $\text{Ni}_{1-x}\text{Mn}_x\text{Fe}_2\text{O}_4$ film prepared with 3 wt% of Mn exhibits superior ferrimagnetic behaviour with the highest value of η_B (57.31) due to the high crystallinity, packing density, and smooth surface of the film.

Kwang Pyo Chae et. Al. [36] studied the effects of sintering and substitution on the crystallographic and magnetic properties of Nickel Substituted Manganese Ferrites Synthesized by Sol-gel Method. Sintering at 523 K showed a superparamagnetic phase mainly because of its small size. Coercivity and Saturation magnetization was found to increase drastically with hotter sintering. The X-ray diffraction patterns of the $\text{Mn}_{1-x}\text{Ni}_x\text{Fe}_2\text{O}_4$ ($0.0 \leq x \leq 0.6$) ferrites sintered at 773 K indicated typical spinel structures. Lattice constant decreases but particle size increases with increasing Ni substitution. Particle sizes were confirmed by FESEM results. The hysteresis curves obtained from VSM revealed typical soft ferrite patterns. Saturation magnetization and coercivity increased with increasing Ni concentration which was explained using the changes of particle size.

M.K. Shobana and S. Sankar [37] studied the structural, thermal and magnetic properties of $\text{Ni}_{1-x}\text{Mn}_x\text{Fe}_2\text{O}_4$ nano ferrites synthesised by sol-gel combustion technique. The peaks in the XRD pattern indicated the presence of spinel structure with no other reflections. The particle size was found to decrease with increasing Mn doping. Observed results of thermal studies revealed that substitution of Mn reduces the ferritization process which may be attributed to decreasing particle size with Mn concentration. VSM results showed that saturation magnetisation and coercivity decreases with an increase in Mn doping which may be attributed to the reduction of crystallite size under the influence of Mn^{2+} in B sub lattice.

JinAh Hwang et. Al. [38] investigated structural and magnetic properties of Zn doped Ni ferrite which was synthesised by thermal decomposition method. XRD analysis showed the presence of a pure spinel ferrite structure. Crystallite size was calculated to be 46-51 nm in diameter which was supported by the FE-SEM measurements. The lattice parameter of the ferrite nanoparticles increased from 8.34 to 8.358 Å with an increase in zinc concentration from 0.5 to 0.7. Also with increasing Zinc concentration, decrease in saturation magnetization and the coercivity were reported from 83 to 71 emu/g and from 18.54 to 16.48 Oe respectively. The high saturation magnetization was attributed to the arrangement of cations on the sub-lattices A and B. The transition temperature between the paramagnetic and ferromagnetic phase was found to decrease rapidly with increasing nonmagnetic Zn ions. The cut-off frequency of the ferrite toroidal samples

was estimated to be about 20 MHz which seemed to be associated with domain wall resonance and spin resonance. With increasing Zn doping, the crystalline anisotropy decreased but permeability was increased. An increase in real permeability with Zn ion concentration was attributed to domain wall mobility.

Kamellia Nejati and Rezvanh Zabihi ^[39] examined nanosized Ni ferrite for various structural and magnetic properties synthesised with and without surfactant by hydrothermal method. Investigations were performed using XRD, FT-IR, TEM, ICP-AES and VSM techniques. XRD analysis showed that in the samples prepared without surfactant, the peaks become sharper as the temperature is increased which indicates increased crystallinity. The crystallinity of NiFe₂O₄ nanoparticles was reduced in comparison with the surfactant-free sample. Clearly visible peaks at higher temperatures confirmed the formation of cubic spinel structure with some impurities when surfactants were added. An increase in temperature increases the crystallite size. VSM measurements showed prepared samples to be soft magnetic with negligible coercivity which indicates the presence of small magnetic particles exhibiting superparamagnetic behaviours at room temperature. The coercivity at 100 °C and 130 °C prepared without surfactant showed coercivity of 15.67 Oe. The increase in saturation magnetization with temperature was attributed to increasing in crystallinity and particle size of the samples.

G. Vasuki and T. Balu ^[40] investigated structural, compositional and magnetic properties of Cu_{0.5}Mn_{0.5}Fe₂O₄ through SEM, EDX, powder XRD and VSM analysis. Sample was prepared using the Co-precipitation method. XRD pattern revealed the formation of a single-phase cubic spinel nanoferrite. The estimated particle size was found to be 30nm. The lattice constant value is found to be 8.4196 Å. Lattice constant value is found to be less than that of bulk material. The X-ray density was reported to be 5.239 (g/cm³). The SEM micrograph showed fine crystalline rod-like morphology. The agglomeration of particles was reported due to the permanent magnetic moment possessed by the particle. EDX pattern indicated the presence of copper, manganese, iron, oxygen and traces of sulphur in the ferrite samples. VSM analysis showed a low value of coercivity and squareness (Retentivity /Saturation Magnetisation) ratio which confirmed the isotropic nature of the material. This property of the material finds its potential applications as an absorbing material and in biomedicine.

Irfan Elahi et al. ^[41] studied the physical and magnetic properties of manganese ferrite powder prepared by the Co-precipitation method. The XRD pattern of powder exhibited all the peaks related to the single-phase cubic spinel structure of Mn Ferrite. The lattice parameter and particle size were found to be 8.493 Å and 23.53 nm respectively. SEM image indicated that the microstructure of the grains of the sample was ultra-small with an average grain size of 10 µm. From the VSM data, the

value of magnetic saturation 16.36 emu/g, was obtained at an applied field of 6.7 kOe. With low coercivity and low area hysteresis curve, the material indicated soft magnetism which is applicable for magnetic memory purposes.

Saima Rani and Syed Shahbaz Ali ^[42] investigated structural, magnetic and optical properties of Mn-Zn ferrites annealed at different temperatures by using the Co-precipitation method. From XRD analysis lattice parameter, phase structure and particle size were determined. XRD pattern confirmed the formation of the cubic spinel structure of particles. The particle size and lattice parameter increased with temperature with no change recorded in the interplanar spacing d . With increasing temperature, particles were found to gain more crystallinity. The SEM images show that the as-deposited particles were more agglomerated. EDX graph shows the existence of Zn, Mn, Fe and O₂ atoms in the formed samples. Reverse quantization phenomena was revealed from XRD results and the UV-Vis results. The hysteresis curve from VSM analysis revealed that all samples with different saturation magnetization M_s values showed ferromagnetic behaviour with M_s and coercivity increasing with annealing. With high Magnetisation saturation, low coercivity and low remanence, these materials showed soft magnetic nature.

In the present work, we report the structural and magnetic properties of Nickel doped Manganese ferrite ($\text{Ni}_x\text{Mn}_{1-x}\text{Fe}_2\text{O}_4$) have been extensively studied in the scope of various applications. Particularly Manganese is used as a doping candidate because of its oxidation states and significant increase of the atomic magnetic moment. The combustion route is used for the synthesis of the samples of different concentration. Characteristic studies are done with the help of Powder X-Ray diffraction technique (P-XRD), Scanning electron microscopy (SEM), Energy dispersive X-ray spectroscopy (EDX) and Vibrating Sample Magnetometer (VSM).

Chapter 1 includes the introductory explanation of spinel ferrites, the application of spinel ferrites in general, the specific importance of Nickel Manganese ferrite and the literature review.

Chapter 2 represents the different methods of sample preparation with emphasis on the combustion method. Also, the advantages and disadvantages of these methods are discussed in this chapter.

Chapter 3 deals with the experimental details of the various characterisation techniques used for structural and magnetic studies of the prepared samples.

Chapter 4 illustrates the results of all the characterisation techniques and interprets the behaviour of different parameters.

Chapter 5 includes concluding remarks of the present work and the related future scope of study.

1.6 References

- [1] T. Tatarchuk, M. Bououdina, J. Judith Vijaya., 2017. "Spinel Ferrite Nanoparticles: Synthesis, Crystal Structure, Properties, and Perspective Applications." 305- 325. Research Gate 305-325. doi: 10.1007/978-3-319-56422-7_22.
- [2] P.P. Naik, R.B. Tangsali, B. Sonaye, S. Sugur. 2015. Journal of Magnetism and Magnetic materials (Elsevier) 378-385. doi: 10.1016/j.jmmm.2015.03.032.
- [3] A.T. Odularu, 2018. "Metal Nanoparticles: Thermal Decomposition, Biomedical Applications to Cancer Treatment, and Future Perspectives." Bioinorganic Chemistry and Applications (Hindawi) 1-6. doi: 10.1155/2018/9354708.
- [4] R. Valenzuela, 2012. "Novel Applications of Ferrites." Physics Research International (Hindawi Publishing Corporation) 1-9. doi:10.1155/2012/591839.
- [5] S. Mirzaee, Y. Azizian-Kalandaragh, P. Rahimzadeh. 2019. "Modified co-precipitation process effects on the structural and magnetic properties of Mn- doped nickel ferrite nanoparticles." Solid-State Sciences (Elsevier) 99: 1-24. doi:10.1016/j.solidstatesciences.2019.106052.
- [6] T. Shanmugavela, S. Gokul Rajb, G. Ramesh Kumar, G. Rajarajan. 2014. "Synthesis and Structural Analysis of Nanocrystalline MnFe₂O₄." physics Prodecia 159-163.
- [7] R. E. Kumar, A., S. Kamzin, T. Prakash. 2014. "Effect of particle size on structural, magnetic and dielectric properties of manganese substituted nickel ferrite nanoparticles." Journal of Magnetism and Magnetic Materials (ELSEVIER) 389-396. doi:https://doi.org/10.1016/j.jmmm.2014.11.019.
- [8] S. Sharifi, A. Yazdani and K. Rahimi. 2020. "Incremental substitution of Ni with Mn in γ -NiFe₂O₄ to largely enhance its supercapacitance properties." Scientific reports (Nature search) 1-15. doi: 10.1038/s41598-020-67802-z.
- [9] A. B. Mapossa, W. Mhike, J. L. Adalima and S. Tichapondwa. 2021. "Removal of Organic Dyes from Water and Wastewater Using Magnetic Ferrite-Based Titanium Oxide and Zinc Oxide Nanocomposites: A Review." Catalysts (MDPI) 11 (12): 1-32. doi: 10.3390/catal11121543.
- [10] K. Pubby, S. B. Narang and. 2021. "Nickel Spinel Ferrites: A review." Journal of Magnetism and Magnetic Materials (Elsevier) 519: 1-58. doi: 10.1016/j.jmmm.2020.167163.
- [11] S.A.V. Prasad, M. Deepty, P.N. Ramesh, Ch. Srinivas, and N. KrishnaMohan. 2018. "Synthesis of MFe₂O₄ (M=Mg,Zn,Mn)spinel ferrites and their structural, elastic and electron magnetic

resonance properties." *Ceramics International* (Elsevier) 44 (9): 10517-10524. doi: 10.1016/j.ceramint.2018.03.070.

[12] R. S. Duncan, and H. A. Stone. 1956. "A Survey of the Application of Ferrites to Inductor Design." *Proceedings of the IRE (IEEE)* 4-13. doi:10.1109/JRPROC.1956.274843.

[13] Sugimoto, M. 2004. "The Past, Present, and Future of Ferrites." *Journal of the American Ceramic Society (The American Ceramic Society)* 82 (2): 269-280. doi:10.1111/j.1551-2916.1999.tb20058.x.

[14] M.A. Willard, L.K. Kurihara, E.E. Carpenter, S. Calvin & V.G. Harris. 2013. "Chemically prepared magnetic nanoparticles." *International Materials Reviews (Taylor & Francis)* 49 (3-4): 125-170. doi:10.1179/095066004225021882.

[15] R. Kesavamoorthi, C. Ramachandra. 2016. "Studies on the Properties of Manganese Substituted Nickel Ferrite Nanoparticles." *Springer (Springer)*. doi:10.1007/s10948-016-3792-8.

[16] T.F. Marinca, I. Chicinaş, O. Isnard, B. V. Neamţu. 2015. "Nanocrystalline/nanosized manganese substituted nickel ferrites – $\text{Ni}_{1-x}\text{Mn}_x\text{Fe}_2\text{O}_4$ obtained by ceramic-mechanical milling route." *Ceramics International*. doi:http://dx.doi.org/10.1016/j.ceramint.2015.11.155.

[17] R.E. Kumar, R. Jayaprakash, S. Kumar. 2013. "Effect of annealing temperature on structural and magnetic properties of manganese substituted NiFe_2O_4 nanoparticles." *Materials Science in Semiconductor Processing* 173-177. doi:https://doi.org/10.1016/j.mssp.2013.09.003.

[18] R.S. Pandav, R.P. Patil, S.S. Chavan, I.S. Mulla, P.P. Hankare. 2016. "Magneto-structural studies of sol-gel synthesized nanocrystalline manganese substituted nickel ferrites." *Journal of Magnetism and Magnetic Materials*. doi:https://doi.org/10.1016/j.jmmm.2016.04.090.

[19] Aakash, R. Choubey, D. Das, S. Mukherjee. 2016. "Effect of doping of manganese ions on the structural and magnetic properties of ni ferrite." *Journal of Alloys and Compounds*. doi:https://doi.org/10.1016/j.jallcom.2016.01.198.

[20] P.B. Koli, K.H. Kapadnis, U. G. Deshpande. 2019. "Nanocrystalline modified nickel ferrite films: an effective sensor for industrial and environmental gas pollutant detection." *Journal of Nanostructure in Chemistry (Springer)*. doi:https://doi.org/10.1007/s40097-019-0300-2.

[21] M. Mamata, S. Phanjoubam, C. Prakash. 2008. "Microwave Sintering of Lithium Nickel Manganese Ferrites and their properties." *International Conference on Microwave (IEEE)*. doi:978-1-4244-2690-4444/08.

- [22] Y. Qi, P. Yin, L. Zhang, J. Wang, X. Feng. 2019. "Novel Microwave Absorber of $\text{Ni}_x\text{Mn}_{1-x}\text{Fe}_2\text{O}_4$ /Carbonized Chaff ($x = 0.3, 0.5, \text{ and } 0.7$) Based on Biomass." ACS OMEGA 12376-12384. doi:<https://doi.org/10.1021/acsomega.9b01568>.
- [23] S. Yuvaraj, N. Manikandan, G. Vinitha. 2018. "Structural and nonlinear optical properties of nickel substituted manganese ferrite nanoparticles." Ceramics International 34-39. doi:<https://doi.org/10.1016/j.ceramint.2018.09.033>.
- [24] Z. Zhang, Q. Tan, Z. Zhong, F. Su. 2015. "High-performance nickel manganese ferrite/oxidized graphene composites as flexible and binder-free anodes for Li-ion batteries." Royal Society Of Chemistry 40018-40025. doi: 10.1039/c5ra03556b.
- [25] Z. Kaiwen, Q. Liqin, W. Xuehang, W. Wenwei, S. Yuexiao, T. Yulin, L. Jieyue. 2014. "Structure and magnetic properties of manganese-nickel ferrite with lithium substitution." Ceramics International 1-23. doi:<https://doi.org/10.1016/j.ceramint.2014.09.052>.
- [26] J. Gu, L. Liu, Y. Qi, Q. Xu, H. Sun. 2012. "Synthesis and Magnetic Characterization of Nickel Ferrite Nanowire Arrays Doped with Manganese." Advanced Materials Research (Trans Tech Publications) 233-235. doi:<https://doi.org/10.4028/www.scientific.net/AMR.233-235.1799>.
- [27] B. V. Tirupanyam, Ch. Srinivas, S. S Meena, S.M. Yusuf, A. S. Kumar, D.L. Sastry. 2015. "Investigation of structural and magnetic properties of co-precipitated Mn–Ni ferrite nanoparticles in the presence of $\alpha\text{-Fe}_2\text{O}_3$ phase." Journal of Magnetism and Magnetic Materials (Elsevier) 392: 101-106. doi:<https://doi.org/10.1016/j.jmmm.2015.05.010>.
- [28] R. Iyer, R. Desai, R. V. Upadhyay. 2009. "Low temperature synthesis of nanosized $\text{Mn}_{1-x}\text{Zn}_x\text{Fe}_2\text{O}_4$ ferrites and their characterizations." Bulletin Material Science (Indian Academy of Sciences) 32: 141–147.
- [29] C. Rath, S. Anand, R. P. Das. 2002. "Dependence on cation distribution of particle size, lattice parameter and magnetic properties in nanosize Mn–Zn ferrite." JOURNAL OF APPLIED PHYSICS 91 (4). doi:10.1063/1.1432474.
- [30] P. Mathur, A. Thakur, M. Singh. 2008. "A study of nano-structured Zn–Mn soft spinel ferrites by the citrate precursor method." Physica Scripta (Iop Publishing) 77. doi:10.1088/0031-8949/77/4/045701.
- [31] I. Chicina, T.F. Marinca, B.V. Neamtu, F. Popa, O. Isnard, V. Pop. 2014. "Synthesis, Structural, and Magnetic Properties of Nanocrystalline/Nanosized Manganese-Nickel Ferrite–

[32] I.Chicinaş, T.F.Marinca,B.V.Neamţu,F.Popa,O.Isnard. 2014. "Nanocrystalline/nanosized mixed nickel-manganese ferrites obtained by mechanical milling." *Solid State Phenomena* 50 (4): 243-248. doi:<https://doi.org/10.4028/www.scientific.net/SSP.216.243>.

[33] S. Nasrin, D. Rahaman, A.K.M. Akther Hossain. 2017. "Synthesis the Ni substituted Mn Ferrite and study the applications of ferrite." *Journal of chemical engineering* 21-26.

[34] A. Hussain, T. Abbas, S. B. Niaz. 2012. "Preparation of Ni_{1-x}Mn_xFe₂O₄ ferrites by sol–gel method and." *Ceramics International* 1221-1225.

[35] K. Sasikumar, · R. Bharathikannan, G. Sujithkumar, S. Raja, G. Johnsy Arputhavalli, · M. Vidhya, R. Marnadu, R. Suresh. 2021. "32) Structural, Optical, and Magnetic Properties of Mn Doped Nickel Ferrite (Ni_{1-x}Mn_xFe₂O₄) Thin Films Deposited by Jet Nebulizer Spray Pyrolysis Technique." Springer.

[36] K. P. Chae, W. O. Cho, J.-Gwang Lee, B.-S. Kang, S. H. Choi. 2013. "Crystallographic and Magnetic Properties of Nickel Substituted Manganese." *Journal of Magnetism and Magnetic Materials* 21-23.

[37] Sankar, M. K. Shobana S. 2008. "Structural, thermal and magnetic properties of Ni_{1-x}Mn_xFe₂O₄ nanoferrites." *Journal of Magnetism and Magnetic Materials* 2125–2128.

[38] Jinha Hwang, Moonhee Choi, Hyosoon shin, Byeong kwon, Myoung Pyo Chun. 2020. "35) Structural and Magnetic Properties of NiZn Ferrite Nanoparticles Synthesized by a Thermal Decomposition Method." *applied sciences* 1-11.

[39] Zabini, K. Nejati and Rezvanh. 2012. "Preparation and magnetic properties of nano size nickel ferrite particles using hydrothermal method." *Chemistry Journal* 1-6.

[40] G. Vasuki and T. Balu, 2017. "Structural And Magnetic Characterization Of Copper Manganese Ferrite Nanoparticles Synthesized By Chemical Co-precipitation Route." *International Journal of Latest Trends in Engineering and Technology* 132-134.

[41] I. Elahi, R. Zahira, K. Mehmood, A. Jamil and N. Amin. 1-5. "Co-precipitation synthesis, physical and magnetic." *African Journal of Pure and Applied Chemistry* 2012.

[42] S. Rani and S. Ali. n.d. "Synthesis and characterization of Zn doped Mn ferrites." Department of Physics, The University of Lahore, Lahore Pakistan.

CHAPTER II: METHODS OF MATERIAL PREPARATION

The properties of the particles at the nanoscale are greatly influenced by the technique used for its synthesis. The size and shape of the Spinel Ferrites can regulate their physical and chemical properties to a great extent ^[1]. Hence the selection of suitable techniques to obtain the desired nanoparticle becomes essential. Here we have mentioned some of the common and effective methods of preparation of ferrite nanoparticles with their advantages and disadvantages.

2.1 Co-precipitation method

Co-precipitation is one of the oldest and most quoted synthesis methods to obtain nanoparticles, especially Spinel ferrite nanoparticles. This method has gained attention as a simple, cost-effective, and fast process, easily transposable on a larger scale for industrial applications ^[2]. The process of Co-precipitation is shown in figure 2.1. The relevance of co-precipitation lies in the key factors, the two major steps involved in the process: (a) a chemical co-precipitation of constituents (b) heat treatment to obtain spinel ferrites.

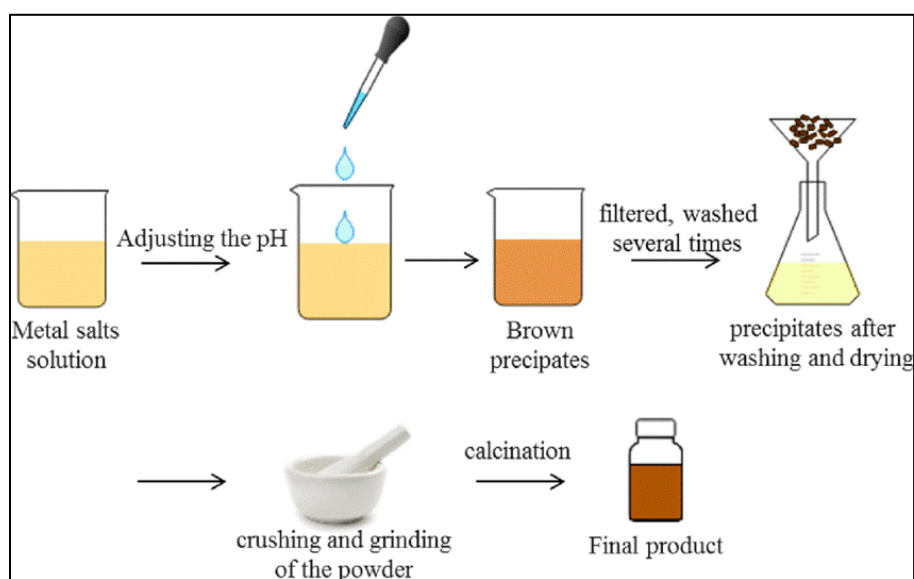


Figure 2.1 - Synthesis of spinel ferrite nanoparticles by co-precipitation method ^[2].

In the Synthesis of iron oxides and metal ferrite nanoparticles by co-precipitation, aqueous solutions of Fe (III) and M(II) salts (where M(II) is a *d*-block transition metal) are usually mixed in an alkaline solution, leading to the formation of the magnetic precipitate. Stoichiometric quantities of analytical grade reagents are mixed in double-distilled deionized water which is used as a solvent to avoid the

production of impurities in the final product. To regulate the particle growth, an appropriate amount of capping agent such as Canola oil is used. The pH maintained for the alkaline solution is a deciding factor in the reaction completion. NaOH can be used as a precipitating agent as well as for controlling the pH of the solution depending upon the precursors used [3]. The reactants are continuously stirred maintaining a pH level of 11-12 [3,4]. The reaction mixture is heated at 80°C for an hour to convert the co-precipitate into spinel ferrite. The product is then cooled to room temperature and the precipitates are separated and washed with water and ethanol. In some cases, the centrifugation technique is also used to collect the precipitate [3]. The precipitate is dried overnight at 100°C. The obtained substance is grinded into fine powder. The residual water is removed by heating the powder at 450 °C for 10 hours [4].

- Advantages

- a) It is an eco-friendly route that grants nanomaterial with high purity without requiring hazardous organic solvents.
- b) Homogeneous mixing of reacting materials, decrease in the reaction temperature, and formation of uniform-sized nanoparticles.

- Disadvantages

- a) Probability of impurity formation, incomplete precipitation, time-consuming.
- b) Little or no control over morphology and non-homogeneous particle size [2,5].

2.2 Spray pyrolysis method

Spray pyrolysis is a process in which an aerosol-containing precursor is sprayed or injected using a nano-porous nebulizer onto the hot substrate in the furnace as shown in figure 2.2. This leads to the decomposition of the precursor to form the final product on the substrate. Chemical substances are selected such that compounds other than the desired product are volatile at the deposition temperature. The steps involved in the spray pyrolysis technique include precursor solution composition, aerosol generation transport, and synthesis. The structural properties of the particles are dependent on the concentration of reactants in the precursor solution, the nature of additives, the flow rate of droplets, and other preparatory conditions. The homogeneity of the particles is expected as each droplet acts like a microreactor in which the constituents are mixed on the atomic level [6]. A wide range of chemical compositions can be formed including complex, multi-

component systems. Spray pyrolysis is very useful in synthesizing Nano-ferrite thin films and clusters at a large scale.

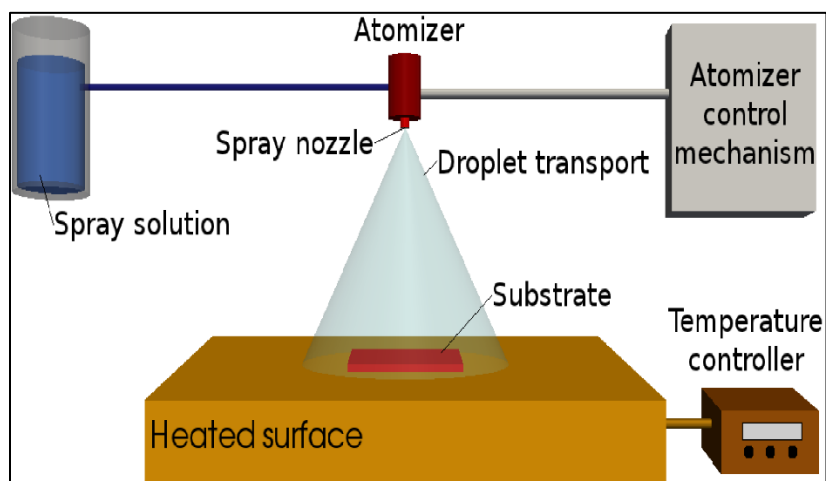


Figure 2.2 - Set-up of Spray pyrolysis technique [7].

All the required reagents are dissolved in stoichiometric amounts in deionized water with constant stirring for ensuring homogeneous mixing. To prevent high-velocity hydrolysis, a few drops of Nitric acid are added to this solution. The solution of Polyvinyl-Alcohol in the ethanol-water mixture is prepared by constant stirring and heating at a constant temperature of 40°C until the final solution obtained is clear and homogeneous. A proportionate amount of this solution is mixed into the main precursor solution. The mixtures are vigorously stirred then used for the spray procedure. The aerosol of the resultant solution is created by a pneumatic glass nebulizer and is transferred to the substrate heated at 300-400°C. The glass substrate is slowly cooled and the sample is peeled out from the substrate [8,9].

- Advantages
 - a) Comparatively pure particles in the submicron range can be produced.
 - b) The narrow distribution of drops and the control on the average size of particles [6].
- Disadvantages
 - a) Phase segregation and in-homogeneity lead to the appearance of unwanted phases in the particles, despite the initial atomic-level mixing of the precursor solution.
 - b) Improper mixing also affects particle morphology.

2.3 Hydrothermal synthesis method

The hydrothermal method is one of the most ecological and promising synthesis methods. Depending upon the requirements of the particle size distribution and morphology, different solvents can be used instead of water which will then be termed as Solvo-thermal method. A typical

Hydrothermal synthesis method is depicted in figure 2.3. The term hydrothermal is defined as performing chemical reactions in solvents contained in sealed vessels in which the temperature of solvents can be regulated to their critical points via heating simultaneously with autogenous pressures. An aqueous mixture of precursors is heated in a sealed stainless-steel autoclave above the boiling point of water and consequently, the pressure within the reaction autoclave is intensely increased above atmospheric pressure [2,10]. The method has been most successfully applied to produce ferrites nanoparticles.

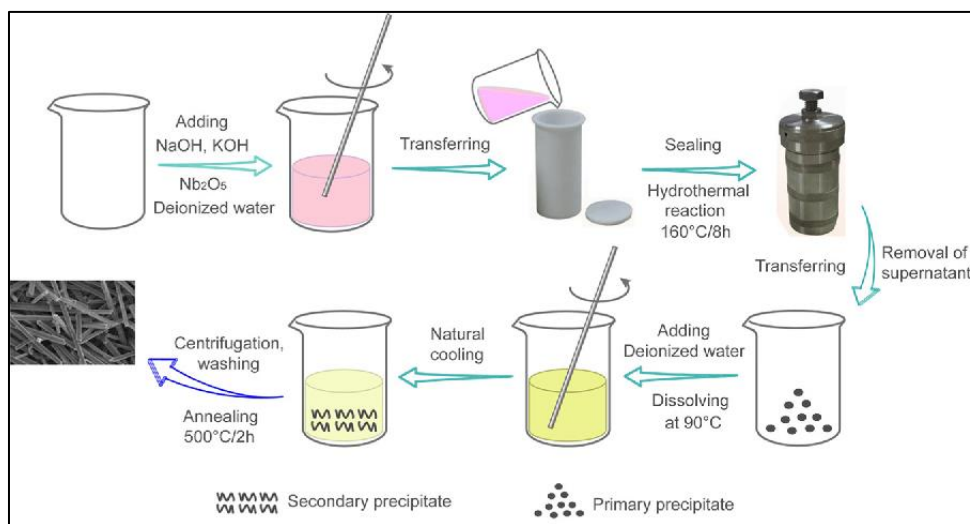


Figure 2.3 - Schematic Representation of Hydrothermal technique [11].

This process is carried out in a specific style of a strong vessel called ‘Autoclave’, which intends to face up to high temperatures and pressure levels from within. Stoichiometric amounts of analytical grade precursors are dissolved in deionized (DI) water and then pH is maintained by adding sodium hydroxide solution into the resultant solutions. The prepared precipitate is washed many times with DI water until a neutral pH value is obtained. The suspension solution is then transferred into a Teflon-lined stainless steel high-pressure autoclave reactor for hydrothermal synthesis and the temperature is maintained at 150°C for about 18 hrs [12]. The obtained materials are centrifuged, washed, and dried to obtain the desired ferrite nanoparticles.

- Advantages
 - a) The ability to synthesize substances that are unstable near the melting point.
 - b) The ability to produce large crystals of high quality.
 - c) The ability to generate crystalline phases which are not stable at the melting point.

- Disadvantages
 - a) Expensive and High pressure, special reactor required (autoclave).
 - b) The slurry formed is highly corrosive [2,10].

2.4 Sol-gel method

Sol-gel is one of the well-established synthetic approaches to prepare novel metal oxide nanoparticles as well as mixed oxide composites. This method can control the textural and surface properties of the materials. The final product can be produced within a few steps using this method. This method is also recognized as sol-gel auto-combustion, sol-gel autoignition, auto-ignition, or self-propagation as well as gel-thermal decomposition [2]. The synthesis process is presented in figure 2.4. The formation of metal oxide involves different successive steps, initially, the corresponding metal precursor undergoes rapid hydrolysis to produce the metal hydroxide solution, followed by instantaneous condensation which leads to the creation of three-dimensional gels. Afterward, the obtained gel is subjected to the drying process, and the resulting product is readily converted to Xerogel or Aerogel based on the mode of drying.

Stoichiometric quantities of metal precursors are dissolved in a minimum amount of distilled water. Then the appropriate amount of organic fuel (chelating/combustion agents) is added to assist the combustion process. Examples of organic fuels are Citric acid ($C_6H_8O_7$), urea (CH_4N_2O), glycine ($C_2H_5NO_2$), ethylene glycol ($C_2H_6O_2$), hydrazine (N_2H_4), carbonylhydrazide (CH_6N_4O), alanine ($C_3H_7NO_2$), acetic acid (CH_3COOH) and acrylic acid ($C_3H_4O_2$), hexamethylenetetramine ($C_6H_{12}N_4$), polyvinyl alcohol (C_2H_4O)_x, etc. For the synthesis of spinel ferrite nanoparticles, citric acid is the most commonly used combustion fuel because of its cost-effectiveness. The addition of a dilute ammonia solution helps in correcting the pH of the resultant solution. Further, this solution is heated to allow it to evaporate till gels are formed, which on continuous heating under combustion produces dry powder [2,3]. The Solid powder is annealed at different temperatures in the furnace.

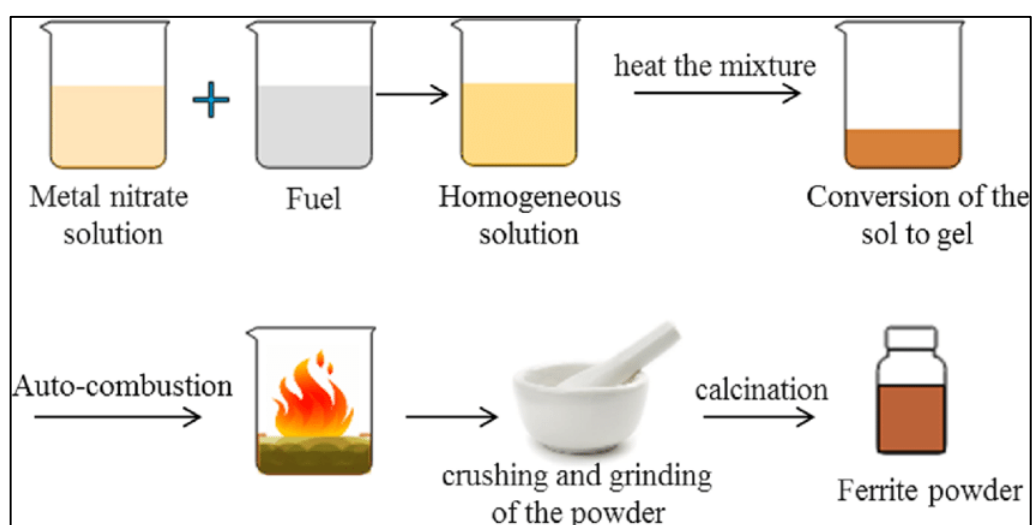


Figure 2.4 - Synthesis of Nano-ferrite by Sol-gel method [2].

- Advantages
 - a) It provides better homogeneity compared to the usual ceramic method.
 - b) It helps in gaining high purity, lower processing temperature, and more uniform phase distribution in multicomponent systems ^[10,13].
 - c) It increases the possibility of obtaining better size and morphological control.

- Disadvantages
 - a) Use of organic solutions that can be toxic.
 - b) Lengthy processing Time.
 - c) High cost of the Precursors.
 - d) Residual hydroxyl and/or carbon groups ^[10]

2.5 High Energy Ball Milling Method

High energy ball milling is one of the commonly used techniques among the top-down approach. It is one of the simplest methods of synthesizing nanoparticles. Ball milling is the process of grinding a material into a fine powder using a cylindrical device filled with both the material to be processed and the grinding medium as shown in figure 2.5 ^[14]. Nanoparticles are produced by mechanical attrition. Attrition is the collision between metal and material. The kinetic energy of the grinding medium i.e., balls is imparted to the sample material placed in the container along with the balls. Ultimately this helps in the size reduction of the materials.

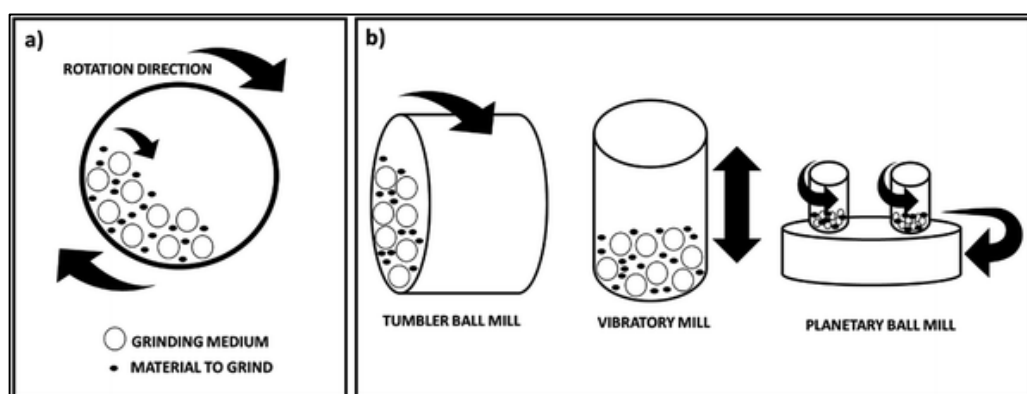


Figure 2.5 - Schematic Representation of Ball milling Method ^[14]

Precisely weighed powder samples are poured into the container along with hardened steel or tungsten carbide balls. The grinding balls to the material ratio is 10:2. Then the container is rotated at high speed (a few hundreds of RPM) around their axis. Additionally, it may also rotate around

some central axis which is then termed as ‘Planetary ball mill’. The high-speed rotation of the container causes differential movements between the balls and there is a collision between the balls and the material. As high energy is generated during this process, it is also named ‘High energy ball milling’. So, during the process of collision between the balls and the material, the materials get crushed and their size is reduced ultimately leading to nano-size particles. Balls used can be made up of various materials such as stainless steel, hardened steel, tungsten carbide, zirconia, alumina, and silicon nitride. High density and larger balls give better outcomes because they increase impact energy on the collision. Balls should be heavier than the material to be milled. The ball to powder mass ratio represents the weight ratio of milling balls to powder. A wide range of BPRM has been used in different experiments ^[14,15]. About 50% of the space of the container should be left empty to ensure that enough space is there for the balls and the material to move around freely in the container. If the container is more than half-occupied, then the efficiency of milling is reduced. The impurities will surge with milling time and some undesirable phases may form if the material is milled for a longer time. Different types of mills have different milling speeds. Above a certain critical speed, the ball gets attached to the walls of the container and they do not execute any impact force on the material. Below this critical speed, if the milling speed is higher, then the milling intensity will be higher.

- Advantages

- a) Nano-powder of 2-20 nm in size can be produced.
- b) It is an inexpensive and easy process.

- Disadvantages

- a) The shape of the Nano-material may be irregular.
- b) There may be contaminants imparted from the balls and milling additives.
- c) This method may produce crystal defects ^[10].

2.6 Thermal Decomposition Method

Thermal decomposition also known as thermolysis is a chemical decomposition that is triggered by heat. This is an endothermic reaction in which the thermal energy is supplied to break chemical bonds in the compound undergoing decomposition. This method can be used for the synthesis of various ferrite Nano-particles.

All the analytical grade reagents consisting of divalent and trivalent transition metal salts are uniformly mixed in appropriate concentrations concerning their chemical form. Different chemicals such as a reducing agent (1,2-hexadecandiol), surfactant (Oleylamine and Oleic acid), and Solvent (Benzyl ether) are used in this method. In some cases, according to the precursors used, it is found that Oleylamine which is one of the best surfactants for thermal decomposition, also plays the role of a solvent as well as a mild reducing agent in the chemical reaction. Precisely weighed precursors are dissolved in Oleylamine and other chemicals under constant stirring to prepare a Homogeneous mixture. For evaporation of water, this precursor solution is heated to 200°C for about 1 hr under the N₂ atmosphere. The temperature is then increased to 300°C and maintained for 1 hr. The solution is cooled to room temperature and then centrifuged for half an hour at a speed of 4000 rpm. The product is washed with hexane and ethanol to separate the organic remains from ferrite particles. Hexane is used to dissolve fat acids such as oleylamine and oleic acid. The final product of Nano-particles is then collected and dried at 100°C for 24 hours ^[1,16].

- Advantages
 - a) Suitable size control and narrow distribution range
 - b) Excellent crystallinity of individual NPS and ability of the method to be used for mass production.

- Disadvantages
 - a) High cost of precursors/surfactants and their possible toxicity in this method
 - b) Absolute controlling of size, shape, and distribution in this method is very difficult and the formation mechanism of the fabricated magnetic NPS is vague ^[10].

2.7 Ultrasonic (Sono-chemical) Method

Sono-chemical synthesis is the process that utilizes the principles of sonochemistry to make molecules undergo a chemical reaction with the application of powerful ultrasound radiation (20kHz- 70kHz) as shown in figure 2.6. Sonochemistry is understanding the effect of ultrasound in forming acoustic cavitation means a reduction of pressure to or below the liquid's vapour pressure which leads to the formation of small vapour-filled cavities in the liquid. This results in the initiation or enhancement of the chemical activity in the solution. This process is widely used for the synthesis of Spinel ferrite nanoparticles due to facial control of reaction conditions ^[13]. The temperature and intensity of the Ultrasonic waves are the major factors that directly impact the particle size of the Spinel ferrites.

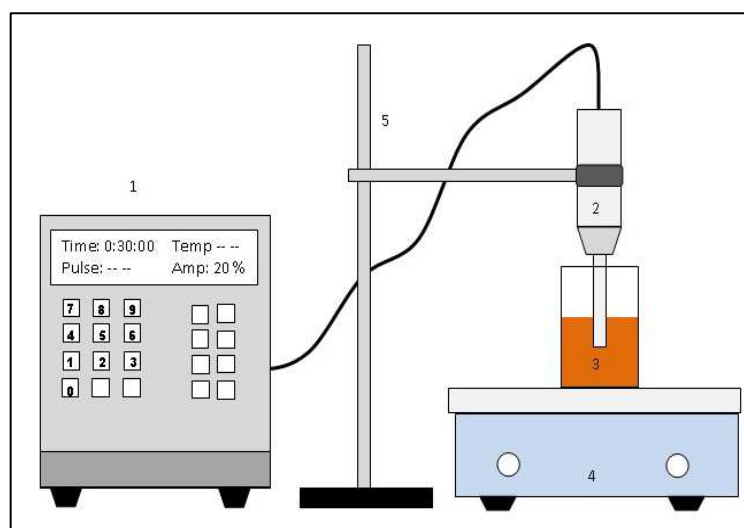


Figure 2.6 - Setup of Ultrasonic technique ^[17]

Compounds of Analytical grade of the required spinel ferrite are chosen. An aqueous solution of starting precursors is prepared in their stoichiometric ratio by dissolving in deionized water. An aqueous solution of NaOH (reagent) is mixed in this prepared starting precursor solution with constant stirring using a magnetic stirrer. Further, the aqueous mixture is subjected to high-intensity ultrasonic irradiation (frequency: 20 kHz and power: 70 W). The composition of the liquid medium changes as the reaction proceeds. This can lead to a change in the acoustic impedance of the system, due to which the power delivered by the sonicator probe to the system also varies giving rise to artifacts. Therefore, it is advisable to use automatic frequency tuning and amplitude compensation, which ensures constant power delivery to the reaction system during sonication, irrespective of the changes occurring in the medium ^[17]. The irradiation is passed till temperature reaches around 100°C and powder form is obtained. The obtained nanoparticles are then separated by the centrifuge process. These nanoparticles are washed several times in distilled deionized water for the removal of residual sodium ions. They are further dried at 60 °C for 24 hours. There are numerous ways of synthesizing nanoparticles from this method using other chemicals. The process will alter to some extent according to the chemicals used but the basic principle remains the same ^[1,3].

- Advantages

- a) Better control over reaction condition and the particle size distribution
- b) Helps in achieving homogeneous mixture.
- c) Reduced no. of reaction steps and improves reaction rate ^[10,13].

- Disadvantages

- a) Low efficiency and low yield ^[10].

2.8 Micro-emulsion

IUPAC defines micro-emulsion as dispersion made of water, oil, and surfactant(s) that is an isotropic and thermodynamically stable system with dispersed domain diameter varying approximately from 1 to 100 nm, usually 10 to 50 nm [18]. That's the reason they are termed nanoparticles. This method is broadly used for the production of inorganic nanoparticles. When oil is mixed in water, they form two different phases as they are immiscible. In order to mix the two phases, energy input is required which can be provided by adding surfactants. Surfactants contain hydrophilic (water-loving) and lipophilic (oil-loving) groups which can reduce the interfacial tension between oil and water. After adding a surfactant, a solution of monodispersed liquid is formed [1].

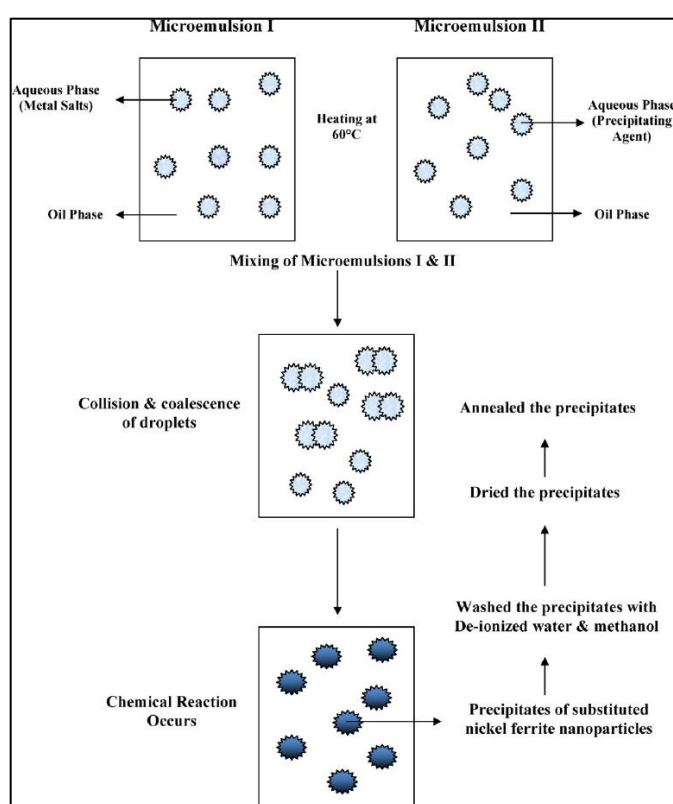


Figure 2.7 - Schematic representation of Micro emulsion method [19]

Schematic diagram of Micro emulsion method is depicted in figure 2.7. Metallic nanoparticles can be synthesized by simple mixing of two water-in-oil micro emulsions, one containing an aqueous phase of salt or a complex of metal with the oil phase (Micro emulsion I) and the other containing an aqueous phase of a precipitating agent with oil phase (Micro emulsion II). After mixing the two emulsions, Brownian motion is formed because of the exchange of the reactants (collision) between micelles. These formed particles collide continuously resulting in the formation of short-lived aggregates. Hence it will rapidly disintegrate into its original size. Good collisions lead to

coalescence, fusion, and homogeneous mixing of reactants. Metal nuclei are formed from the reaction between solubilizates. The growth stage happens around the nucleation point, where a successful collision occurs between a reverse micelle moving a nucleus and another one moving the product monomers with the arrival of more reactants due to inter-micellar exchange. The morphology and size of nanoparticles depend upon the type of surfactant and the size and shape of the nanodroplets. The surfactant is usually used to stabilize the particle and guard them against further growth.

In some cases, heating is required for obtaining the final product whereas in some cases centrifugation is required. It all depends upon the chemical reagents used in the process. Sometimes a co-surfactant is used which expands the microemulsions stability region, which makes it possible to produce more nanoparticles as well as a larger particle size ^[1,13].

- Advantages

- a) The particle size can be controlled by optimizing the concentration of surfactants and co-surfactant combination and oil-to-water ratio.
- b) This reaction is known for being eco-friendly and favourable at low temperatures ^[13].

- Disadvantages

- a) Poor crystalline nature of synthesized Spinel Ferrites.
- b) Requirement of larger amounts of solvents and high polydisperse due to the slower nucleation rate at low temperature.
- c) Large amounts of surfactant and/or cosurfactant, generally irritating at high concentrations, and temperature-dependent ^[2,10].

2.9 Combustion Method

Self-propagating High-Temperature (SHT) combustion synthesis is a low-cost, high throughput method that is currently used on an industrial scale at least in 65 countries. It has gained attention because of the simplicity of the method and cost-effective processing. The solution-combustion method which is favoured for the production of nanosized powders contains two processes. First, the constituents of the precursor are intimately blended and then the precursor is subjected to combustion. Due to the exothermal nature of the synthesis method either a flame or fire is produced.

The most important parameters surrounding the reaction are the fuel source properties as well as the miscibility and decomposition temperature of the precursors. The fuel should maintain the compositional homogeneity of the precursors and have a low ignition temperature. Combustion helps to crystallize the precursor and form the desired phase.

- Advantages
 - a) Easy control of particle size and composition.
 - b) The particle surface state and overall homogeneity can be easily modified.
 - c) Versatile and rapid preparation with no use of organic solvent.

- Disadvantages
 - a) It does not work efficiently if the reactants have very different precipitation rates.
 - b) Trace impurities may also get precipitated with the product.
 - c) Time-consuming.

Careful control of the above factors must be maintained or it will result in loss of size and dispersity control of the crystallites. Method refinement is needed to produce agglomeration-free particles with a predictable morphology ^[20,21].

Sample Preparation by Combustion Method:

Six different concentration of Mn-Ni ferrite nanoparticles were prepared using combustion route according to general formula $Mn_{1-x} Ni_x Fe_2 O_4$ ($x = 0, 0.2, 0.4, 0.5, 0.6, 0.8$). The flowchart of this method is shown in figure 2.8. The metal salts were weighed such that the final product obtained will be 5 grams. The Metal salts used in sample preparation are Manganese (II) Acetate, Nickel (II) Nitrate, Ferric Nitrate along with NTA as a complexing agent, and Urea as Combustion Fuel. All the precursors were taken in stoichiometric ratios to meet the requirement of the particular concentration. NTA was weighed equal to the total mass of all the metal salts and Urea was weighed to be 140% of NTA mass. After accurate weighing, the reagents were carefully poured into a 600ml dry beaker. The residual contents on the butter paper were washed with distilled water in the beaker itself. After adding all the reagents, the beaker was filled with distilled water up to 400 ml.

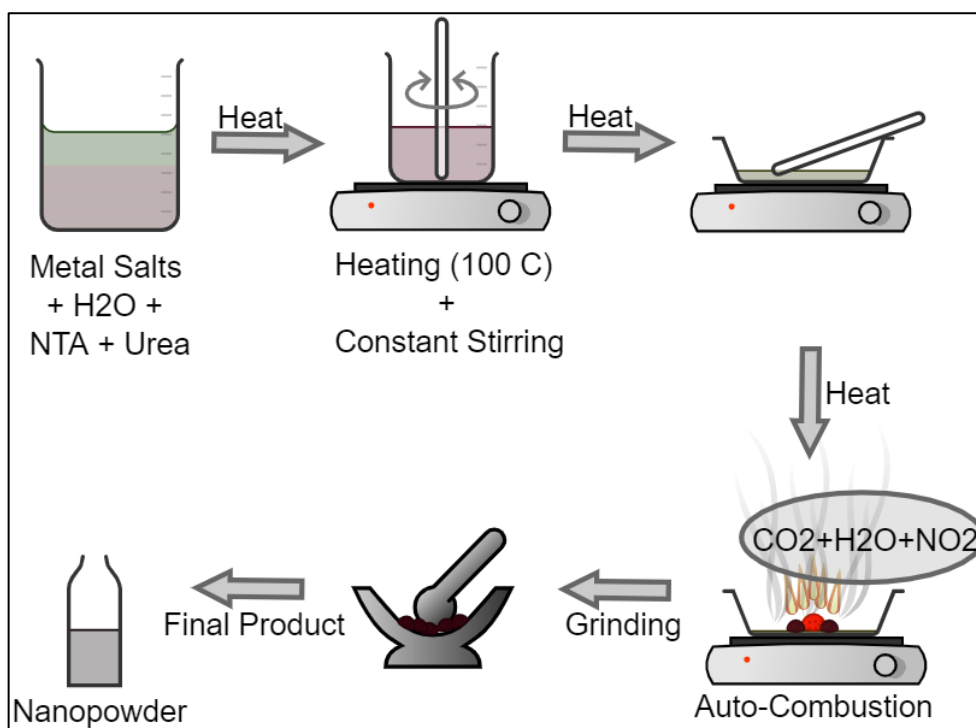
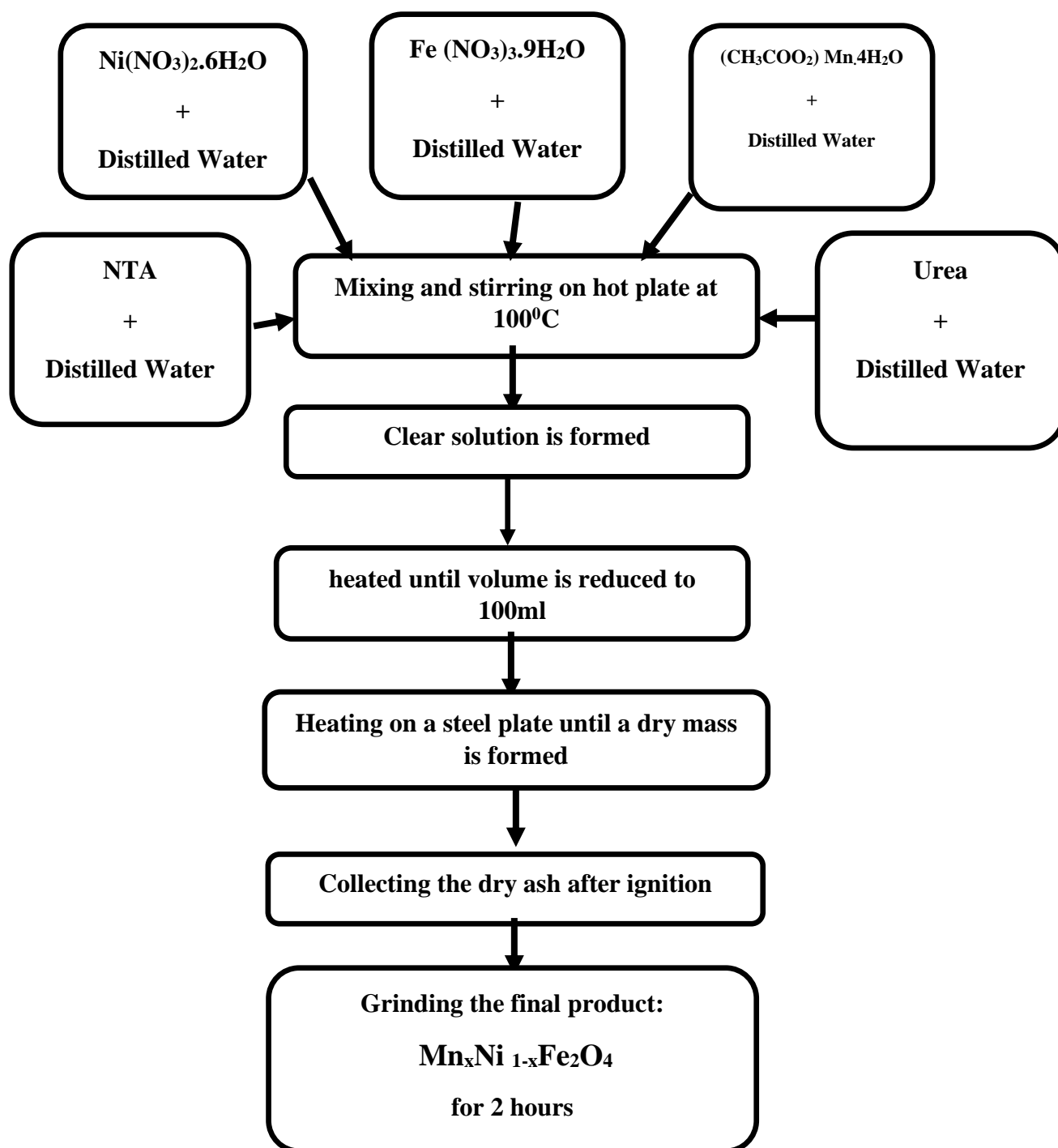


Figure 2.8 - Flowchart for the synthesis of spinel ferrite by Combustion method.

The resultant solution is subjected to the heat of about 100°C with constant stirring. An electrical stirrer was specially designed for uniform stirring to obtain a homogeneous mixture of clear solution. A magnetic stirrer was not used in this case as its angular frequency changes with an increase in temperature which will resist us from obtaining the desired outcome. With constant stirring, this solution was subjected to conventional heating for volume reduction resulting in a viscous mass. After about 2 hours of constant heating and stirring, the volume of the viscous mass is reduced to 200ml which was then transferred to the plate and heated till the ignition temperature of the fuel is reached. At this temperature, auto combustion was triggered which turns the black paste into a reddish dry mass which then turns into black dry powder indicating total combustion of the mixture. This residual dry powder is properly collected neglecting some unburnt particles at the edge of the plate. The collected powder is then grinded into ultrafine nano-powder for 1 hr [22-24]. The same process is followed for other samples with varying concentrations. Stepwise procedure of the prepared sample is depicted in figure 2.9.

Schematic of flow chart of sample preparation:



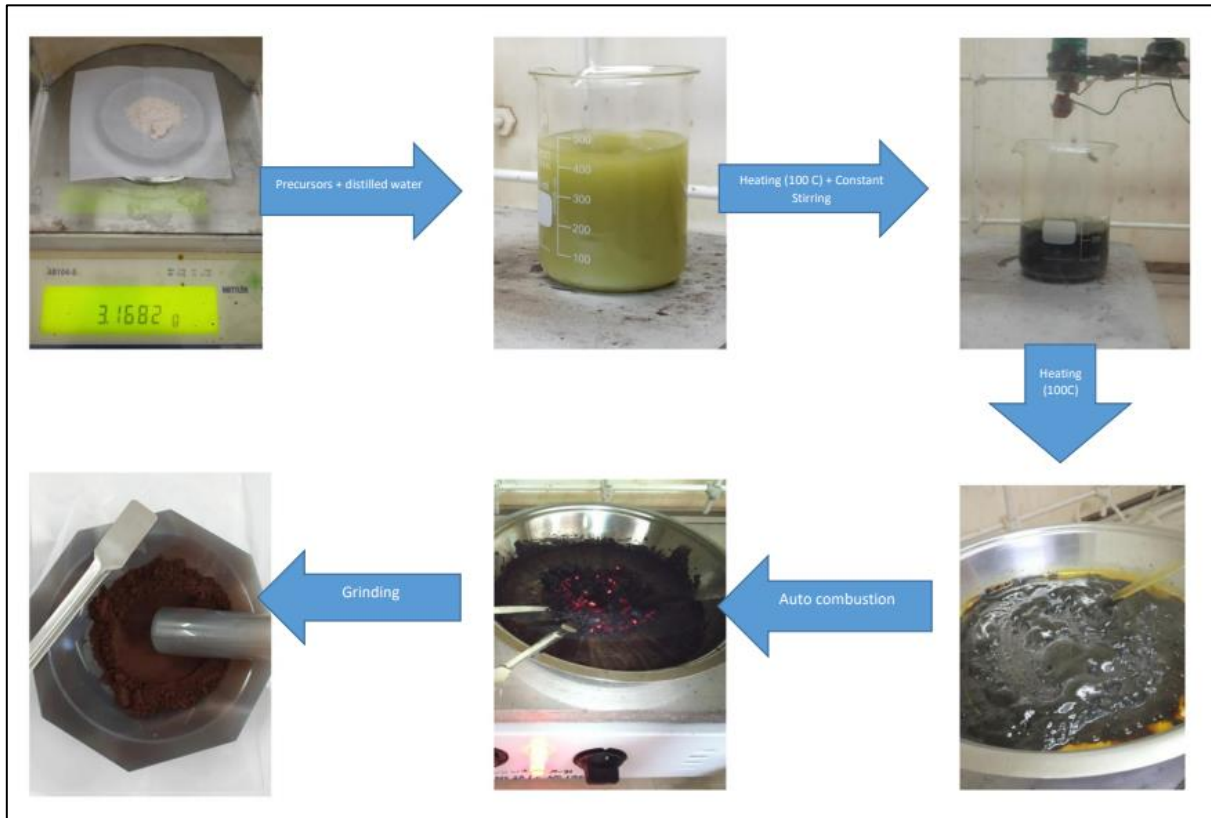


Figure 2.9 - Glimpses of the Sample preparation process

2.10 References

- [1] T. Cele, 2019. "Preparation of Nanoparticles." In Engineered Nanomaterials, 1-14. IntechOpen. doi: [10.5772/intechopen.90771](https://doi.org/10.5772/intechopen.90771)
- [2] A. Soufi, H. Hajjaoui, R. Elmoubarki, M. Abdennouri, S. Qourzal, N. Barka. 2021. "Spinel ferrites nanoparticles: Synthesis methods and application in heterogeneous Fenton oxidation of organic pollutants." Applied Surface Science Advances (Sciencedirect) 1-18. doi: [10.1016/j.apsadv.2021.100145](https://doi.org/10.1016/j.apsadv.2021.100145)
- [3] M. I. Din, F. Rafique, M. S. Hussain, H. A. Mehmood and S. Waseem. 2019. "Recent developments in the synthesis and stability of metal ferrite nanoparticles." Science Progress (Sage Journals) 102: 61-72. doi:[10.1177/003685041982679](https://doi.org/10.1177/003685041982679)
- [4] M. I. M. Omer, Y. A. Alsabab, A. E. Adam, A. A. Elbadawi. 2020. "Synthesis, Structural and Magnetic properties of Mg_{0.25}Co_{0.75} Fe₂O₄ Nanoparticles Ferrites using Wet chemical routes." Researchgate 1-8. https://www.researchgate.net/publication/344375369_Synthesis_Structural_and_Magnetic_properties_of_Mg_025_Co_075_Fe_2_O_4_Nanoparticles_Ferrites_using_Wet_chemical_routes.
- [5] A. V. Rane, K. Kanny, V.K. Abitha and S. Thomas. 2008. "Methods for Synthesis of Nanoparticles and Fabrication of Nanocomposites." In Synthesis of Inorganic Nanomaterials, 121-139. Elsevier. doi: [10.1016/B978-0-08-101975-7.00005-1](https://doi.org/10.1016/B978-0-08-101975-7.00005-1).
- [6] M. Tripathi and B. Singh. 2022. "Synthesis of green nanocomposite material for engineering application." In Sustainable nanotechnology for environmental remediation, 135-156. Elsevier. doi: [10.1016/B978-0-12-824547-7.00012-6](https://doi.org/10.1016/B978-0-12-824547-7.00012-6).
- [7] Filipovic, L. 2015. "Topography Simulation of Novel Processing Techniques." TU Wien. <https://www.iue.tuwien.ac.at/phd/filipovic/node56.html>.
- [8] V.N. Blaskov, I.D. Stambolova, S.V. Vassilev, C.D. Dushkin. 2013. "Photocatalytic degradation of malachite green by zinc oxide sprayed films." Bulgarian Chemical Communications (Bulgarian Academy of Sciences) 45: 263 – 267. http://www.bcc.bas.bg/bcc_volumes/Volume_45_Number_2_2013/Volume_45_Number_2_2013_PDF/BCC-54-2-263-267.pdf.
- [9] I. Anila, S. P. John, J. Mathew. 2017. "Synthesis and Characterisation of Nickel Ferrite Nanoparticles Prepared by Spray Pyrolysis Method." International Journal of Scientific Research in Science and Technology (IJSRST) (ResearchGate) 3 (11): 212-219.

https://www.researchgate.net/publication/336916486_Synthesis_and_Characterisation_of_Nickel_Ferrite_Nanoparticles_Prepared_by_Spray_Pyrolysis_Method.

[10] E. M. Modan, A. G. Plăiașu. 2020. “Advantages and Disadvantages of Chemical Methods in The Elaboration of Nanomaterials.” *Metallurgy And Materials Science (The Annals Of “Dunarea De Jos” University Of Galati)* 53-60. doi: [10.35219/mms.2020.1.08](https://doi.org/10.35219/mms.2020.1.08).

[11] Z. Deqing, F. Shia, J. Chengc, Z. Chenga, X. Yanga, G. Zhengd and M. Caob. 2015. Modified hydrothermal synthesis and structural characterization of monoclinic ($K_x Na_{1-x}$) NbO_3 ($0.05 < x < 0.15$) rods." *Semantic Scholar*. <https://www.semanticscholar.org/paper/Modi-fi-ed-hydrothermal-synthesis-and-structural-of-Zhanga-Shia/b4c80de96c4f687b3383da8e2ce91de6a4eccc0d>.

[12] C. Y. Tsay, Y. C. Chiu and C. M. Lei. 2018. “Hydrothermally Synthesized Mg-Based Spinel Nanoferrites: Phase Formation and Study on Magnetic Features and Microwave Characteristics.” *Materials (MDPI)* 11 (11): 1-11. doi: [10.3390/ma11112274](https://doi.org/10.3390/ma11112274).

[13] T. Tatarchuk, M. Bououdina, J. J. Vijaya and L. J. Kennedy. 2017. “Spinel Ferrite Nanoparticles: Synthesis, Crystal Structure, Properties, and Perspective Applications.” In *Nanophysics, Nanomaterials, Interface Studies, and Applications*, 305-325. Springer International Publishing. doi: [10.1007/978-3-319-56422-7_22](https://doi.org/10.1007/978-3-319-56422-7_22).

[14] C. C. Piras, S. F. Priet, W. M. De Borggraeve. 2019. “Ball milling: a green technology for the preparation and functionalization of nanocellulose derivatives.” *Nanoscale Advances (Royal Society of Chemistry)* (3): 937–947. doi: [10.1039/C8NA00238J](https://doi.org/10.1039/C8NA00238J).

[15] S.K. Pradhan, S. Bid, M. Gateshki, V. Petkov. 2005. “Microstructure characterization and cation distribution of nanocrystalline magnesium ferrite prepared by ball milling.” *Materials Chemistry and Physics (Sciencedirect)* 93 (1): 224-230. doi: [10.1016/j.matchemphys.2005.03.017](https://doi.org/10.1016/j.matchemphys.2005.03.017)

[16] J. Hwang, M. Choi, H. S. Shin, B. K. Ju and M. Chun. 2020. “Structural and Magnetic Properties of Ni-Zn Ferrite Nanoparticles Synthesized by a Thermal Decomposition Method.” *Applied Sciences (MDPI)* 10 (18): 1-11. doi: [10.3390/app10186279](https://doi.org/10.3390/app10186279).

[17] P. P. Goswami, H. A. Choudhury, S. Chakma, and V. S. Moholkar. 2013. “Sonochemical Synthesis and Characterization of Manganese Ferrite Nanoparticles.” *Industrial & Engineering Chemistry Research (ACS Publications)* 52 (50): 17848–17855. doi: [10.1021/ie401919x](https://doi.org/10.1021/ie401919x).

[18] S. N. Kale, S. L. Deore. 2017. “Emulsion Micro Emulsion and Nano Emulsion: A Review.” *Systematic Reviews in Pharmacy (Sys Rev Pharm.)* 39-47. doi: [10.5530/srp.2017.1.8](https://doi.org/10.5530/srp.2017.1.8).

- [19] Muhammad, M. Ehsan and I. n.d. “Synthesis, Structural and Electrical Characterization of Sb³⁺ Substituted Spinel Nickel Ferrite (NiSb_xFe_{2-x}O₄) Nanoparticles by Reverse Micelle Technique.” 509. doi: 10.1016/j.jallcom.2011.01.193. <https://www.researchgate.net/figure/Schematic-diagram-for-the-microemulsion-method>
- [20] T. Shanmugavel, S. Gokul Raj, G. Rajarajan, G. Ramesh Kumar. 2014. “Tailoring the structural and magnetic properties and of nickel ferrite.” *Procedia Materials Science (Sciencedirect)* 6: 1725 – 1730. doi: [10.1016/j.mspro.2014.07.158](https://doi.org/10.1016/j.mspro.2014.07.158).
- [21] A. K. Tyagi, 2007. “Combustion Synthesis: A Soft-Chemical Route For Functional Nano-Ceramics.” *BARC Newsletter (285)*: 39-48. doi: [10.1.1.508.7890](https://doi.org/10.1.1.508.7890).
- [22] P. P. Naik, R.B. Tangsali, S.S. Meena, S.M. Yusuf. 2017. “Influence of rare earth (Nd³⁺) doping on structural and magnetic properties of nanocrystalline manganese-zinc ferrite.” *Materials Chemistry and Physics (Elsevier)* 191: 215-224. doi: [10.1016/j.matchemphys.2017.01.032](https://doi.org/10.1016/j.matchemphys.2017.01.032).
- [23] P. P. Naik, R.B. Tangsali. 266-275. “Enduring effect of rare earth (Nd³⁺) doping and gamma-radiation on electrical properties of nanoparticle manganese zinc ferrite.” *Journal of Alloys and Compounds (Elsevier)* 723: 2017. doi: [10.1016/j.jallcom.2017.06.207](https://doi.org/10.1016/j.jallcom.2017.06.207).
- [24] S. H. P. Keluskar, P. P. Naik and S. S. Hasolkar. 2019. “Effect of Sintering on Structural and Morphological Properties of Nanoparticle Manganese Zinc Ferrite Synthesized using combustion Method.” *International Journal of Nano Materials and Chemistry (Natural Sciences Publishing Cor.)* 3: 37-40. doi: [10.18576/ijnc/050301](https://doi.org/10.18576/ijnc/050301).

CHAPTER III: CHARACTERISATION TECHNIQUES

3.1 X-ray Powder Diffraction

3.1.1 Introduction

X-rays are electromagnetic radiation of exactly the same nature as light but of very much shorter wavelength about 1 Å. Max Von Laue in 1912, discovered that the crystalline substances act as three-dimensional diffraction gratings for X-ray wavelengths similar to the spacing of planes in a crystal lattice. X-ray powder diffraction (XRD) is a powerful technique used to uniquely identify the crystalline phases present in materials and to measure the structural properties of these phases. XRD is also used to determine the thickness of thin films and multilayer and atomic arrangements in amorphous materials (including polymers) and at interfaces. The intensities measured with XRD can provide quantitative, accurate information on the atomic arrangements at interfaces (e.g., in multilayers). It may be used to determine its structure, average particle size, unit cell dimensions and sample purity ^[1].



Figure 3.1 - X-ray Diffractometer

3.1.2 Basic Principle of X-ray Diffraction

X-ray powder diffraction is based on the constructive interference of monochromatic X-rays and a crystalline material. These X-rays are generated when electrons moving at high speed are directed to a metal target; a small percentage of their kinetic energy is converted into X-rays. The X-rays emitted by the target consist of a continuous range of wavelength and is called white radiation. The minimum wavelength in continuous spectrum is inversely proportional to the applied voltage, which accelerates the electron towards the target. If the applied voltage is sufficiently high in addition to the white radiation, the target also emits a characteristic radiation of specific wavelength and high intensity.

The radiation emitted by a target includes both types of radiation. In spectroscopic notation, the characteristic radiations are named as $K_\alpha K_\beta K_\gamma$ etc. K_α radiation has high intensity and is commonly used for diffraction studies. The wavelength of this radiation for a typical copper metal target is 1.54056 \AA . A beam of X-rays directed at a crystal as shown in figure 3.1 interacts with the electron of the atom that constitutes the crystal that is incident on a sample creates secondary “diffracted” beams actually generated in the form of cones as shown in figure 3.2

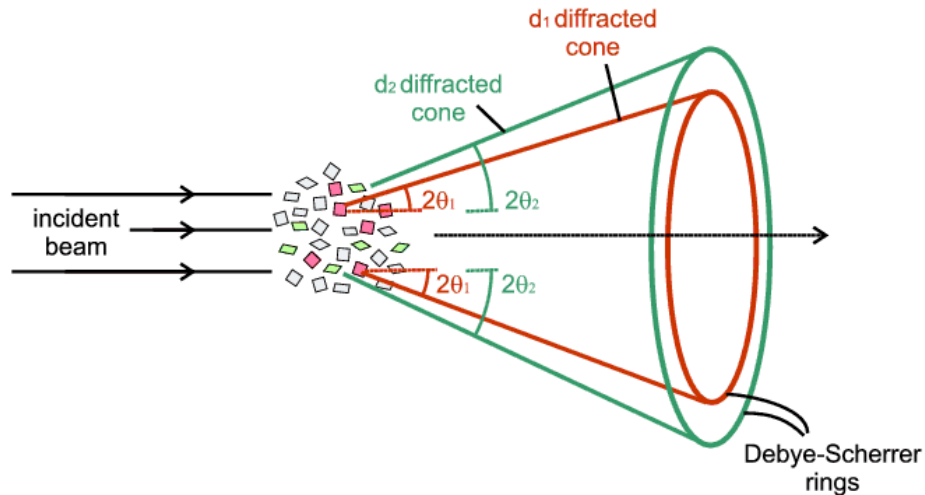


Figure 3.2 - Formation of Cone [2]

According to a mathematical relation called Bragg’s Law

$$n\lambda = 2d \sin\theta \quad \text{Eq. [1]}$$

Where n is an integer, λ is the wavelength, d is the interplanar spacing and θ is the diffraction angle. The intensity of the diffracted x-rays was measured and plotted as a function of diffraction angle 2θ . From the 2θ values of the peaks, the lattice spacing (d) values are calculated using Equation 1.

We can derive the Bragg law for a powder specimen in a diffractometer having a statistically infinite amount of randomly oriented crystallites. Diffraction peaks are measured along the 2θ diffractometer circle. The “angle” of the diffraction is related to the interplanar spacing ‘ d ’ through Bragg’s law and the intensity of the diffraction maximum is related to the strength of those diffractions in the specimen. Diffracted cones of each plane of powder crystalline samples and their Photograph are shown in figure 3.3. X-ray data are recorded in terms of 2θ (x-axis) vs. intensity (y-axis). The angles and intensities of diffractions are recorded electronically using a detector, electronics and specialized software resulting in a plot of 2θ v/s intensity for the specimen.

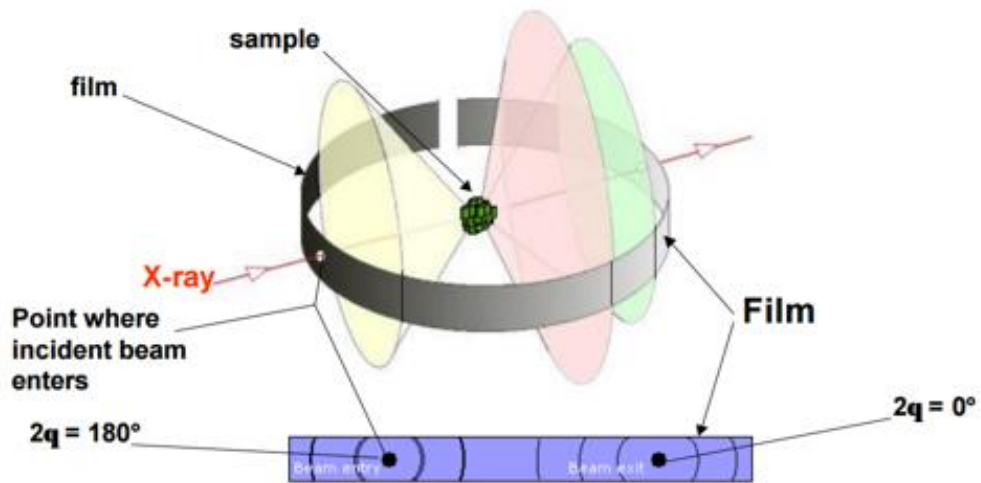


Figure 3.3 - Diffracted cones of each plane of powder crystalline samples and their Photograph ^[3]

The simplest and most widely used method for estimating crystallite size is from the Full Width at Half Maximum (FWHM) of a diffraction peak by Debye-Scherrer's formula (Equation 3.2)

$$D = \frac{0.9\lambda}{\beta \cos\theta} \quad \text{Eq. [2]}$$

Where 'D' is the crystallite size, λ is the wavelength of the X-ray radiation, β is the angular width (in radians) which is equal to the (FWHM). Rigaku Smart Lab X-ray Powder Diffractometer was used here to obtain the X-ray diffraction pattern of the samples using Cu K α lines.

The lattice parameter 'a' was then computed by assuming cubic symmetry that is when a = b = c, sample identification can be easily done by comparing the experimental pattern to that in the International Centre for Diffraction Data (ICDD) file. For single crystalline particles, the randomly oriented crystals in nanoparticles cause broadening of the diffraction patterns when the crystalline sizes are in the order of few nanometers ^[1]

3.1.3 Instrumentation

A powder X-ray diffractometer consists of

- an X-ray source (usually an X-ray tube)
- a sample stage
- detector

The X-ray is focused on the sample at some angle θ , while the detector opposite the source reads the intensity of the X-ray it receives at 2θ away from the source path. The incident angle is then increased over time while the detector angle always remains 2θ above the source path.

1. X-ray source

X-ray tube is a common source of x-rays. It comprises of an evacuated tube which contains a copper block anode bearing a metal target made of any of the metals such as molybdenum, tungsten, copper, rhodium, silver or cobalt. The cathode is a tungsten filament. On passage of electric current through the filament electrons are generated which move towards the anode under the highly accelerated voltage typically 30 – 150 kV. The accelerating electrons on striking the metal surface knock out electrons from the inner shells and the vacancies created are filled by electrons from the outer shells. In the process metal atoms emit x-rays. However, this involves heating of the metal block and x-rays constitute only a small fraction of the total energy liberated. The emitted x-rays exit the tube through a beryllium window. The copper block needs to be cooled with a supply of water to dissipate the excessive heat generated. The Be window helps transmit a monochromatic beam of x-rays. Further monochromatization can be achieved by making use of a zirconium filter when using molybdenum as metal target. It absorbs the unwanted emissions while allowing the desired wavelengths to transmit.

2. Sample Stage

Sample stage is also known as sample holder or a goniometer. Single crystal diffractometers make use of 4 circle goniometers. These circles help position the crystal planes for optimum x-ray diffraction settings. The sample stage can be a simple needle that holds the crystal in place or glass plate or fibre on which the crystal is mounted using an epoxy resin. Only sufficient quantity of epoxy resin is used so that the crystal is clearly mounted and not embedded in the resin. The fibre is mounted on a brass mounting pin and then inserted into the goniometer head. The sample is then centred with an optical arrangement such as a microscope or video camera and making adjustments along X, Y and Z directions to achieve optimum centering under the crosshairs of the viewer.

3. Detector

In earlier days photographic films were used for recording the absorption pattern of diffracted beams. With the advances in detection technology more sensitive detector options were incorporated in advanced instruments. Such detectors include gas filled transducers, scintillation counters and semiconductor transducers. Solid state detectors offer highest levels of sensitivity and speed of analysis^[4,5]

3.2 Scanning Electron Microscope (SEM)

3.2.1 Introduction

Scanning electron microscope (SEM) is one of the most widely used techniques in characterization of nanomaterials and nanostructures. The signals that derive from electron-sample interactions reveal information about the sample including surface morphology (texture) and chemical composition of the sample. In most applications, data are collected over a selected area of the sample surface and a two dimensional image is generated that displays spatial variations in these properties. The resolution of the SEM approaches a few nanometres, and the instruments can operate at magnifications that are easily adjusted from - 10 to over 3,00,000. Not only does the SEM produce topographical information as optical microscopes do, it also provides the chemical composition information near the surface. As well as, it is capable of performing analyses of selected point locations on the sample; this approach is especially useful in qualitatively or semi-quantitatively determining chemical compositions ^[6]

3.2.2 Basic Principle of SEM

The Scanning electron microscope works on the principle of applying kinetic energy to produce signals on the interaction of the electrons. These electrons are secondary electrons, backscattered electrons, and diffracted backscattered electrons which are used to view crystallized elements and photons. Secondary and backscattered electrons are used to produce an image. The secondary electrons are emitted from the specimen play the primary role of detecting the morphology and topography of the specimen while the backscattered electrons show contrast in the composition of the elements of the specimen ^[6,7].



Figure 3.4 - Carl Zeiss Scanning Electron Microscope Setup

The source of the electrons and the electromagnetic lenses are from tungsten filament lamps that are placed at the top of the column and it is similar to those of the transmission electron Microscope.

The electrons are emitted after thermal energy is applied to the electron source and allowed to move in a fast motion to the anode, which has a positive charge. The beam of electrons activates the emission of primary scattered (Primary) electrons at high energy levels and secondary electrons at low-energy levels from the specimen surface. The beam of electrons interacts with the specimen to produce signals that give information about the surface topography and composition of the specimen.

The specimen does not need special treatment for visualization under the SEM, even air-dried samples can be examined directly. However, microbial specimens need fixation, dehydration, and drying in order to maintain the structural features of the cells and to prevent collapsing of the cells when exposed to the high vacuum of the microscope.

The samples are mounted and coated with a thin layer of heavy metal elements to allow spatial scattering of electric charges on the surface of the specimen allowing better image production, with high clarity. Scanning by this microscope is attained by tapering a beam of electrons back and forth over a thin section of the microscope. When the electrons reach the specimen, the surface releases a tiny stream of electrons known as secondary electrons which are then trapped by a special detector apparatus. When the secondary electrons reach and enter the detector, they strike a scintillator (a luminescence material that fluoresces when struck by a charged particle or high-energy photon). This emits flashes of light which get converted into an electric current by a photomultiplier, sending a signal to the cathode ray tube. This produces an image that looks like a television picture that can be viewed and photographed. The quantity of secondary electrons that enter the detector is highly defined by the nature of the specimen i.e raised surfaces to receive high quantities of electrons, entering the detector while depressed surfaces have fewer electrons reaching the surface and hence fewer electrons enter the detector. Therefore, raised surfaces will appear brighter on the screen while depressed surfaces appear darker.

3.2.3 Instrumentation

The major components of the Scanning Electron Microscope include;

1. The Electron Source

This is where electrons are produced under thermal heat at a voltage of 1-40kV. the electrons condense into a beam that is used for the creation of an image and analysis. There are three types of electron sources that can be used i. e Tungsten filament, Lanthanum hexaboride, and Field emission gun (FEG)

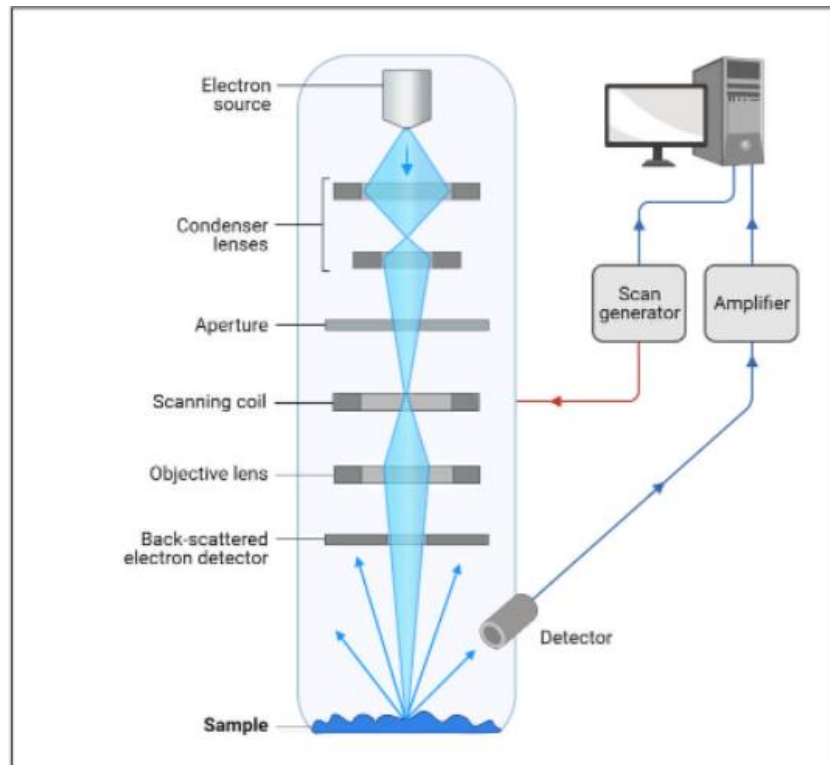


Figure 3.5 - Components of SEM^[7]

2. Lenses

it has several condenser lenses that focus the beam of electrons from the source through the column forming a narrow beam of electrons that form a spot called a spot size.

3. Scanning Coil

They are used to deflect the beam over the specimen surface.

4. Detector

It's made up of several detectors that are able to differentiate the secondary electrons, backscattered electrons, and diffracted backscattered electrons. The functioning of the detectors highly depends on the voltage speed, the density of the specimen.

5. The display device and vacuum system

Scanning electron microscope should be free from vibrations and any electromagnetic elements. Vacuums are needed to prevent electrical discharge in the gun assembly (arcing), and to allow the electrons to travel within the instrument unimpeded ^[6,7,8].

3.3 Energy-dispersive X-ray spectroscopy

3.3.1 Introduction

Energy-dispersive X-ray spectroscopy (EDS or EDX) is a widely used analytical technique for the investigation of elemental or chemical characterization of the specimen. It relies on exciting core electrons of the atom causing the electrons in higher energy levels to drop down and fill that generated hole which results in the emission of X-rays. Each element emits a different set of X-ray frequencies because of its electronic configuration which helps in the identification of different elements present in the specimen. This principle is known as Moseley's Law, which determined that there was a direct correlation between the frequency of light released and the atomic number of the atom. Measuring these emissions can provide both qualitative and quantitative information about the near-surface makeup of the sample [9].

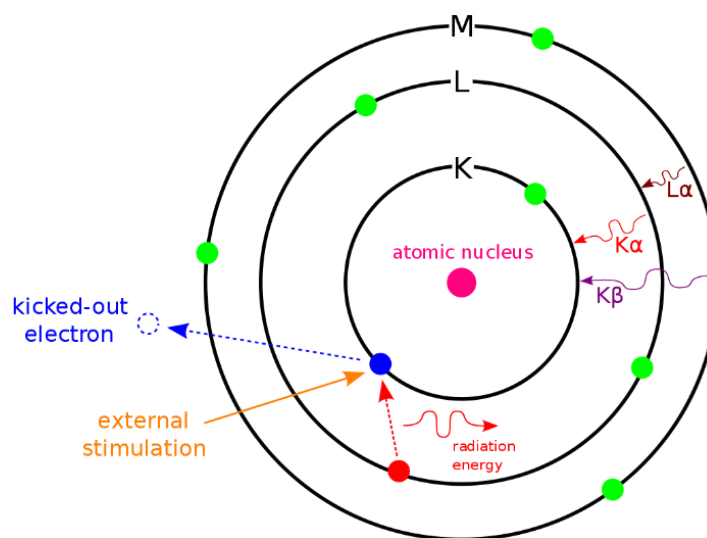


Figure 3.6 - Ejection of Core electrons in EDS [10]

3.3.2 Basic Principle Of EDS

EDS makes use of the X-ray spectrum emitted by a solid sample bombarded with a focused beam of electrons to obtain a localized chemical analysis. All elements from atomic number 4 (Be) to 92 (U) can be detected in principle, though not all instruments are equipped for 'light' elements ($Z < 10$). The fundamental principle is that each element has a unique atomic structure allowing a unique set of peaks on its electromagnetic emission spectrum which are emitted as a result of filling up vacant places of the inner shells. When a sample is irradiated with a highly energetic beam of electrons then a characteristic X-ray is generated. Due to irradiation when an electron is excited from the inner shell of its parent atom, the vacant place is occupied by the higher energy electron from the outer shell, and the energy difference between the two shells is emitted as an X-ray. The

amount of energy released in electron transfer is dependent upon the electron energy level which fills the inner vacant place.

These emitted X-rays are known as characteristic X-rays because their energies (wavelength) are specific to the element from which it is emitted. Thus, this technique can be used for elemental analysis. When K shell electrons are excited, they emit characteristic X-rays which are termed “K Lines” as shown in figure 3.6 and those emitted from L and M shells are called “L Lines” and “M Lines” respectively. When the element is heavy then its characteristics X-rays energies are also higher, therefore incident electrons of higher energy are required. Different types of X-rays are emitted when incident electrons strike the atomic nucleus and these are known as “continuous X-rays”, “white X-rays” and “background X-rays”. Qualitative analysis involves the identification of the lines in the spectrum and Quantitative analysis (determination of the concentrations of the elements present) involves measuring line intensities for each element in the sample and for the same elements in calibration Standards of known composition ^[11].

3.3.3 Instrumentation

EDS instrument is mainly composed of four components as shown in figure 3.7.

- Electron beam source
- X-ray Detector
- Pulse Processor
- Analyzer

These parts are typically equipped with an electron microscope such as SEM or TEM. The combination of these pieces enables analysis of both how many X-rays are released, as well as to measure their energies. As the X-rays are emitted after the electron beam is being incident on the specimen, Detector is used to convert X-ray energy into voltage signals; this information is sent to a pulse processor, which measures the signals and passes them onto an analyser for data display and analysis.

1. Electron beam source:

As EDS is equipped with the scanning electron microscope, the same electron gun (Field Emission) is used as the incident electron source and to focus the beam, lenses are used along with aperture. The energy of the electron beam has to be carefully selected to overcome the adjustment between the resolution requirements and the production efficiency of X-rays.

2. X-ray Detector:

The X-rays counts (which is the abundance of emitted X-rays) versus X-rays energies are measured by the EDS detector. Detector is a solid-state device that is based on lithium drifted silicon. As X-rays strike the surface of the detector, a charge pulse is created. This charge pulse is directly proportional to the energy of the incident X-ray.

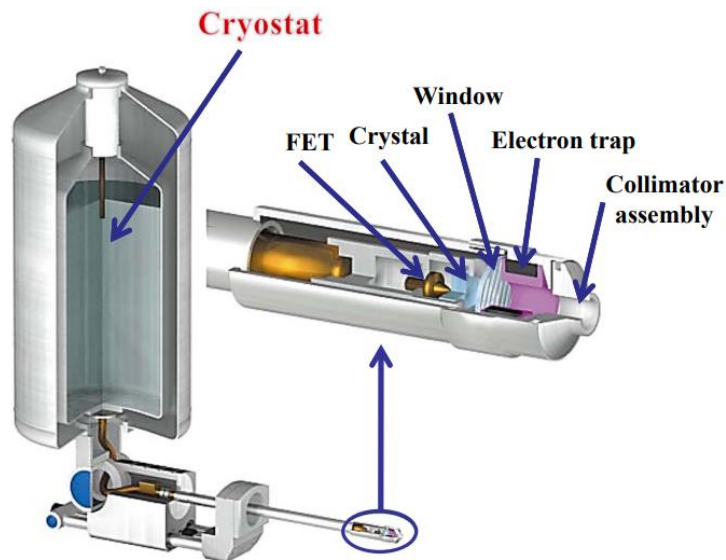


Figure 3.7 - EDS Detector Components ^[12]

Parts of the detector

- i. Collimator assembly: The purpose of the collimator is to provide a restrictive aperture through which X-rays should pass in order to make a way to the detector. The collimator ensures that only X-rays from the region being excited by the beam of the electron are detected.
- ii. Electron trap: Electrons that penetrate the detector cause background artifacts and also overload the measurement chain. The purpose of the electron trap is to guarantee that only X-rays should enter the detector. It comprises a pair of permanent magnets to strongly deflect the passing electrons.
- iii. Window: The purpose of the window is to provide a barrier to maintain vacuum within the detector whilst being as transparent as possible to low energy X-rays. The two main types of window materials are Beryllium (Be) and Polymer-based.
- iv. Crystal
The crystal is a semiconductor device that converts an X-ray of particular energy into electric charge of proportional size through the process of ionization. The most common is silicon (Si), into which is drifted lithium (Li) to compensate for small levels of impurity.

v. FET

The field effect transistor, normally referred to as the FET, is positioned just behind the detecting crystal. It is the first stage of the amplification process that measures the charge liberated in the crystal by an incident X-ray and converts it to a voltage output.

vi. Cryostat

It is used to reduce the effects of the leakage current. The charge signals generated by the detector are small and can only be separated from the electronic noise of the detector if the noise is reduced by cooling the crystal and FET.

3. Pulse Processor:

A charge-sensitive preamplifier is employed to convert the charge pulse to a voltage pulse.

4. Analyzer:

Multi-channel analyser is used to sort pulses by voltage in the signals which are received by the analyser. The energy of the X-ray can be obtained by measuring the voltage of the charge pulses. This energy is then sent for display and data processing. Here, data is displayed as histogram of intensity vs voltage [\[11,13\]](#).

3.4 Vibrating Sample Magnetometer (VSM)

3.4.1 Introduction

Vibrating sample Magnetometer invented by S. Foner is a widely used technique for characterizing properties of magnetic materials. The most fundamental quantity in magnetism i.e. the magnetic moment can be measured using this instrument. It can measure field as small as 10^{-5} to 10^{-6} emu. It operates on Faraday's Law of Induction, which describes that changing magnetic field will produce an electric field. This electric field can be used measured and used to interpret the changing magnetic field. The VSM converts the dipole field of the sample into an ac electrical signal. The sample is placed inside a uniform magnetic field and then vibrated sinusoidally. That creates a corresponding variation of the magnetic flux in pickup coils placed nearby, inducing a sinusoidal voltage ^[14]. The latest lakeshore VSM is depicted in figure 3.8.

3.4.2 Basic Principle of VSM

If a sample of any material is placed in a uniform magnetic field produced between the poles of an electromagnet, a dipole moment will be induced. If the sample vibrates with sinusoidal motion a sinusoidal electrical signal can be induced in suitably placed pick-up coils. The signal has the same frequency of vibration and its amplitude will be proportional to the magnetic moment, amplitude, and relative position with respect to the pick-up coils system.



Figure 3.8 - Lakeshore VSM Setup ^[15]

The VSM technique is based on Faraday's law of induction which relies on the detection of the induced voltage in a coil of wire given by

$$V(t) = -N \frac{\partial}{\partial t} \varphi(t) \quad \text{Eq. [3]}$$

Where,

N is the number of turns in the detection coil,

$\varphi = \mu\mu_0H$ (μ is point dipole and H is the magnetic field)

The induced voltage depends upon (a) Number of turns (b) gradient of H.

On further solving the gradient along the direction of vibration, it is found that the induced voltage depends upon the sensitivity function which represents the derivative along the direction of sample motion, the velocity of the moving sample, and point dipole μ . If the amplitude and frequency of the vibration are known, along with the sensitivity constant, the voltage induced in the detection coil is proportional to the magnetic moment and hence magnetization of sample [16].

The operation of the VSM is fairly simple. The magnetic sample is mounted on the sample holder and placed between the electromagnet poles to which detection coils have been mounted. There are a few types of sample holders as shown in figure 3.9, depending on the types of measurement to be performed. There are both in-plane and/or out-of-plane sample holders.

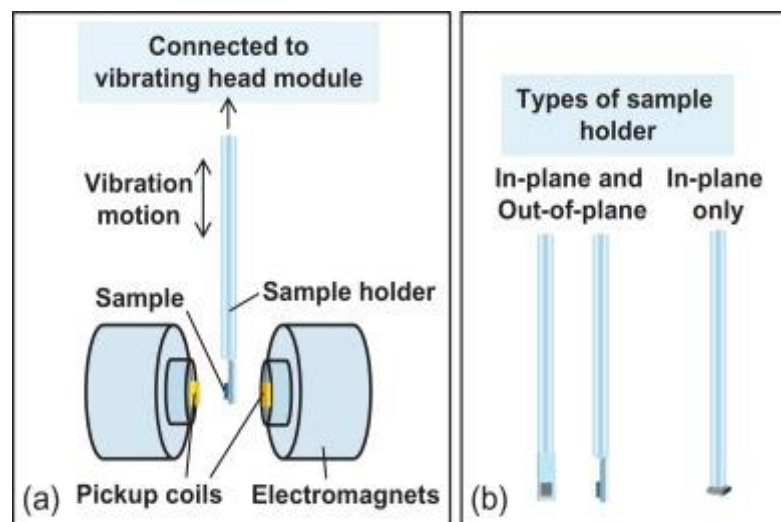


Figure 3.9 - Components of VSM [14]

The sample holder is then driven by a mechanical vibrator. The oscillatory motion of the magnetized sample will induce a voltage in the detection coils. The induced voltage is proportional to the sample's magnetization, which can be varied by changing the dc magnetic field produced by the electromagnet.

3.4.3 Instrumentation

The different constituent parts of the VSM are

1. The vibrating system
2. Lock-In amplifier
3. Electromagnet and power supply
4. Pick up coil or Detection coil

The various components are connected to a computer interface. Using controlling and monitoring software, the susceptibility of the sample can be determined. A typical measurement of a sample is taken in the following manner:

- The strength of the constant magnetic field is set.
- The sample begins to vibrate
- The signal received from the probe is translated into a value for the magnetic moment of the sample
- The strength of the constant magnetic field changes to a new value. No data is taken during this transition
- The strength of the constant magnetic field reaches its new value
- The signal from the probe again gets translated into a value for the magnetization of the sample
- The constant magnetic field varies over a given range, and a plot of magnetization (M) versus magnetic field strength (H) is generated.

6. The vibrating system

The vibration of the sample must be driven by a unit that vibrates harmonically, with low noise and without damping.

7. Lock-in Amplifier

Lock-in amplifiers are used to detect and measure very small AC signals, all the way down to nano volts. These use a technique called phase-sensitive detection to single out the component of the signal at a single reference frequency and phase. Noise signals at frequencies other than the reference frequency are rejected and do not affect the measurements.

8. Electromagnet and Power Supply

Electromagnet is used for producing the uniform magnetic field and suitable power supply is connected to it.

9. Detection Coil

Besides sample position and dimension, another thing that affects the magnitude of the induced voltage is the coil geometry. The parameter which describes the dependence of the output voltage on the coil and sample geometry and their relative displacement is the

sensitivity function. By the principle of reciprocity “Magnetic flux produced by magnetic moment in a coil of arbitrary geometry is equivalent to the field B (at the position of the moment) produced by the same coil carrying a current I.”

$$B \cdot \mu = I\varphi \quad \text{Eq. [4]}$$

For a transverse design or set up, in which the direction of moment vibration is perpendicular to the applied magnetic field, in which the requirement of insensitivity due to sample position and geometry is to be fulfilled: Place the sample at the saddle point of sensitivity function. However, be the design of the detection coil, the winding must be done in series opposite so that the induced voltage gets added up and also the effect of the external magnetic field is zero ^[16,17]

3.5 References

- [1] H. Stanjek, and W. Häusler . 2004. "Basics of X-ray Diffraction." SpringerLink 107–119. doi: [10.1023/B:HYPE.0000032028.60546.38](https://doi.org/10.1023/B:HYPE.0000032028.60546.38).
- [2] Paul Barnes, Simon Jacques, Martin Vickers. 2019. Powder Diffraction on the WEB. <http://pd.chem.ucl.ac.uk/pdnn/diff2/kinemat2.htm>.
- [3] Benvenuti. 2022. "Laue Diffraction." physics open lab. <https://physicsopenlab.org/2018/01/18/laue-diffraction/>.
- [4] B. Udriștioiu, and H. Aboul-Enein. 2015. "X-Ray Diffraction: Instrumentation and Applications." Critical Reviews in Analytical Chemistry 289-299. doi: [10.1080/10408347.2014.949616](https://doi.org/10.1080/10408347.2014.949616).
- [5] Andrei A. Bunaciu, Elena gabriela Udriștioiu, Hassan Y. Aboul-Enein. 2015. "X-Ray Diffraction: Instrumentation and Applications." Critical Reviews in Analytical Chemistry 45 (4). doi: <https://doi.org/10.1080/10408347.2014.949616>.
- [6] Vernon-Parry, K.D. 2000. "Scanning electron microscopy: an introduction." Elsevier Science (Elsevier Science) 40-44. Doi : [10.1016/S0961-1290\(00\)80006-X](https://doi.org/10.1016/S0961-1290(00)80006-X).
- [7] S. Aryal, 2021. "Electron Microscope." Microbe Notes. November 4. <https://microbenotes.com/scanning-electron-microscope-sem/>.
- [8] W. Zhou, R. Apkarian, Z. Wang, and D. Joy . 2006. "Fundamentals of Scanning Electron Microscopy (SEM)." Scanning Microscopy for Nanotechnology (Springer, New York, NY). Doi : [10.1007/978-0-387-39620-0_1](https://doi.org/10.1007/978-0-387-39620-0_1).
- [9] A.V. Gira, G. Caputo, and M. C. Ferro. 2017. "Application of Scanning Electron Microscopy Energy Dispersive X-Ray Spectroscopy." In Characterization and Analysis of Microplastics, by Armando Duarte Teresa Rocha-Santos, 153-168. Elsevier. doi:10.1016/bs.coac.2016.10.002.
- [10] Protter, Bobby Gaston & Connor. 2020. Chemistry Libretexts. 7 May. [https://chem.libretexts.org/Courses/Franklin and Marshall College/Introduction to Materials Characterization CHM 412 Collaborative Text/Spectroscopy/Energy-Dispersive X-ray Spectroscopy \(EDS\)](https://chem.libretexts.org/Courses/Franklin_and_Marshall_College/Introduction_to_Materials_Characterization_CHM_412_Collaborative_Text/Spectroscopy/Energy-Dispersive_X-ray_Spectroscopy_(EDS)).
- [11] Russ, John C. 1984. "Energy Dispersive Spectrometers." In Fundamentals of Energy Dispersive X-Ray Analysis, by John C. Russ, 17-41. Elsevier.

- [12] 2022. West Campus Materials Characterization Core- Yale University. <https://ywcmatsci.yale.edu/edx-principle>.
- [13] A.Pratap. 2012. “Energy dispersive analysis of Xrays.” Pathshala Deshbandu College. [https://www.deshbandhucollege.ac.in/pdf/resources/1585214200_PHY\(H\)-VI-NANO_MATERIAL-1-AJAYPRATAP.pdf](https://www.deshbandhucollege.ac.in/pdf/resources/1585214200_PHY(H)-VI-NANO_MATERIAL-1-AJAYPRATAP.pdf).
- [14] A.O. Adeyeye, G. Shimon. 2015. Magnetism of Surfaces, Interfaces, and Nanoscale Materials. Vol. 5. Elsevier. <https://www.sciencedirect.com/handbook/handbook-of-surface-science>.
- [15] 2022. Quantum Designs - Vibrating Sample Magnetometer (VSM) with electromagnet. <https://qd-europe.com/hu/en/product/vibrating-sample-magnetometer-vsm-with-electromagnet/>.
- [16] D.P Pattnaik. 2014. Design and fabrication of Vibrating Sample Magnetometer. Integrated Masters of Science Thesis, Department of Physics and astronomy, NIT, Roukela Odisha: Department of Physics and astronomy, 1-65. <http://ethesis.nitrkl.ac.in/5906/>.
- [17] S.A.H.Shah 2013. Vibrating Sample Magnetometry: Analysis and Construction. PhD Thesis, Department of Physics, Syed Babar Ali School of Science and Engineering, Research Gate, 1- 45. https://www.researchgate.net/publication/355336773_Vibrating_Sample_Magnetometry_Analysis_and_Construction.

CHAPTER IV: RESULTS AND DISCUSSION

4.1 X-ray diffraction

The structural properties of Nickel doped Manganese ferrite were studied using an X-ray powder diffraction (XRD) analysis, conducted on Rigaku Smart Lab Diffractometer using Cu-K α radiation ($\lambda = 1.5418 \text{ \AA}$) as shown in figure 4.1



Figure 4.1 - Rigaku X-ray Diffractometer

The X-ray diffraction patterns of the series of samples $\text{Mn}_{1-x}\text{Ni}_x\text{Fe}_2\text{O}_4$ ($x = 0.0, 0.2, 0.4, 0.5, 0.6, 0.8$) are depicted in figure 4.2. The structural parameters of all the samples are listed in detail in table 1 and table 2. The XRD result indicates the good crystalline nature of all the samples through the well-defined positions of the diffraction lines and relative intensities of all observed peaks. The diffraction peaks at 2θ are attributed to reflection planes (220), (311), (222), (400), (422), (511) and (440) which confirms the formation of cubic spinel structure with space group $Fd\bar{3}m$ and is well supported by the literature reports [1-7]. The absence of any additional peaks indicates the formation of single phase with the most intense peak observed at $\sim 35^\circ$ corresponding to (311) diffraction plane. These peaks are well determined and clearly show the polycrystalline nature of the ferrite. Small peak shifts have been noticed particularly along (311), (400), (511) and (440) peaks towards higher diffraction angles with increasing Ni concentration. This feature can be attributed to the difference in ionic radius and distribution of cations throughout the nickel-manganese (Ni-Mn) ferrites [8-10].

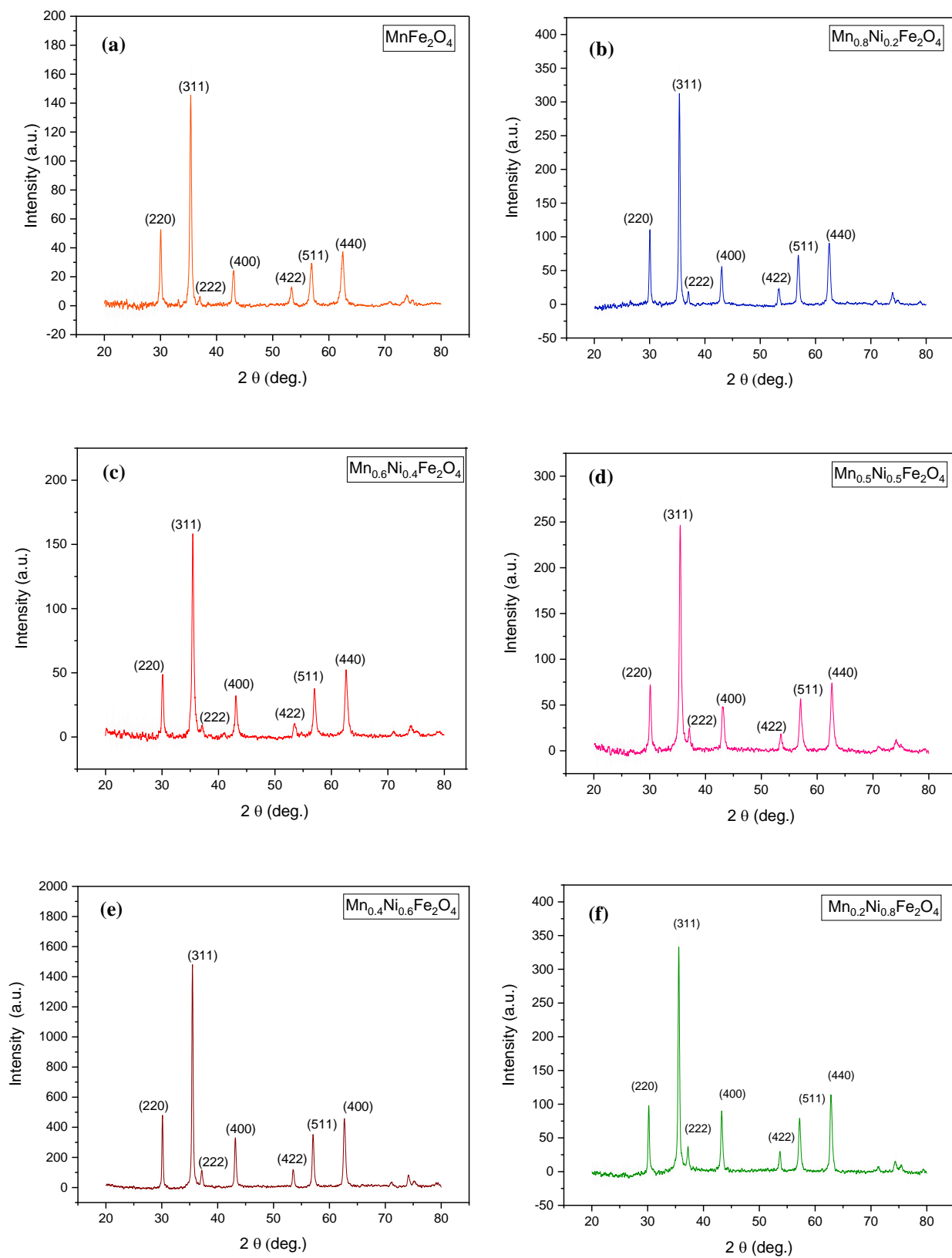


Figure 4.2 - X-ray Diffraction patterns of $\text{Mn}_{1-x}\text{Ni}_x\text{Fe}_2\text{O}_4$ (a) $x=0$ (b) $x=0.2$ (c) $x=0.4$ (d) $x=0.5$ (e) $x=0.6$ (f) $x=0.8$

Table 4.1 - Diffraction angle, Miller indices, interplanar spacing and lattice constant of all the prepared samples of Mn_{1-x}Ni_xFe₂O₄ [(a) x = 0.0, (b) x=0.2, (c) x=0.4, (d) x=0.6 and (e) x=0.8]

Table 4.1-(a) MnFe₂O₄

Sr. No.	2 Θ (Degrees)	Θ (Degrees)	(hkl) Miller Indices	d Interplanar spacing (\AA)	a Lattice Constant (\AA)
1	30.04	15.02	{220}	2.9745	8.4133
2	35.39	17.69	{311}	2.5366	8.4129
3	37.01	18.51	{222}	2.4286	8.4130
4	43.01	21.51	{400}	2.1029	8.4116
5	53.34	26.67	{422}	1.7175	8.4142
6	56.89	28.45	{511}	1.6185	8.4098
7	62.45	31.22	{440}	1.4871	8.4124

Average Lattice constant

$$= (8.412 \pm 0.001) \text{\AA}$$

Crystallite Size (311)

$$= (25.3 \pm 0.3) \text{ nm}$$

Table 4.1-(b) Mn_{0.8}Ni_{0.2}Fe₂O₄

Sr. No.	2 Θ (Degrees)	Θ (Degrees)	(hkl) Miller Indices	d Interplanar spacing (\AA)	a Lattice Constant (\AA)
1	30.06	15.03	{220}	2.9732	8.4094
2	35.40	17.70	{311}	2.5355	8.4094
3	37.03	18.51	{222}	2.4277	8.4099
4	43.03	21.52	{400}	2.1018	8.4074
5	53.38	26.69	{422}	1.7162	8.4076
6	56.90	28.45	{511}	1.6182	8.4085
7	62.49	31.24	{440}	1.4863	8.4078

Average Lattice constant

$$= (8.4090 \pm 0.001) \text{\AA}$$

Crystallite Size (311)

$$= (28.2 \pm 0.2) \text{ nm}$$

Table 4.1-(c) Mn_{0.6}Ni_{0.4}Fe₂O₄

Sr. No.	2 Θ (Degrees)	Θ (Degrees)	(hkl) Miller Indices	d Interplanar spacing (\AA)	a Lattice Constant (\AA)
1	30.21	15.10	{220}	2.9583	8.3674
2	35.42	17.71	{311}	2.5342	8.4050
3	37.19	18.60	{222}	2.4174	8.3740
4	43.09	21.54	{400}	2.0994	8.3974
5	53.37	26.68	{422}	1.7167	8.4100
6	56.93	28.46	{511}	1.6175	8.4046
7	62.54	31.27	{440}	1.4851	8.4010

Average Lattice constant

$$= (8.394 \pm 0.017) \text{\AA}$$

Crystallite Size (311)

$$= (23.5 \pm 0.4) \text{ nm}$$

Table 4.1-(d) Mn_{0.5}Ni_{0.5}Fe₂O₄

Sr. No.	2 Θ (Degrees)	Θ (Degrees)	(hkl) Miller Indices	d Interplanar spacing (Å)	a Lattice Constant (Å)
1	30.12	15.06	{220}	2.9670	8.3921
2	35.48	17.74	{311}	2.5298	8.3902
3	37.10	18.55	{222}	2.4231	8.3939
4	43.15	21.57	{400}	2.0966	8.3864
5	53.53	26.76	{422}	1.7119	8.3865
6	57.06	28.53	{511}	1.6140	8.3865
7	62.67	31.33	{440}	1.4824	8.3860

Average Lattice constant

$$= (8.389 \pm 0.003) \text{ \AA}$$

Crystallite Size (311)

$$= (23.2 \pm 0.3) \text{ nm}$$

Table 4.1-(e) Mn_{0.4}Ni_{0.6}Fe₂O₄

Sr. No.	2 Θ (Degrees)	Θ (Degrees)	(hkl) Miller Indices	d Interplanar spacing (Å)	a Lattice Constant (Å)
1	30.14	15.07	{220}	2.9652	8.3870
2	35.50	17.75	{311}	2.5286	8.3863
3	37.17	18.58	{222}	2.4189	8.3792
4	43.19	21.59	{400}	2.0948	8.3791
5	53.55	26.77	{422}	1.7113	8.3835
6	57.09	28.55	{511}	1.6132	8.3822
7	62.71	31.36	{440}	1.4815	8.3804

Average Lattice constant

$$= (8.382 \pm 0.003) \text{ \AA}$$

Crystallite Size (311)

$$= (34.2 \pm 0.2) \text{ nm}$$

Table 4.1-(f) Sample Mn_{0.2}Ni_{0.8}Fe₂O₄

Sr. No.	2 Θ (Degrees)	Θ (Degrees)	(hkl) Miller Indices	d Interplanar spacing (Å)	a Lattice Constant (Å)
1	30.21	15.11	{220}	2.9582	8.3671
2	35.59	17.79	{311}	2.5226	8.3664
3	37.22	18.61	{222}	2.4156	8.3679
4	43.28	21.64	{400}	2.0903	8.3612
5	53.68	26.84	{422}	1.7075	8.3650
6	57.24	28.62	{511}	1.6095	8.3633
7	62.88	31.44	{440}	1.4780	8.3608

Average Lattice constant

$$= (8.364 \pm 0.003) \text{ \AA}$$

Crystallite Size (311)

$$= (29.6 \pm 0.3) \text{ nm}$$

Table 4.2 - Structural parameters of Mn_{1-x}Ni_xFe₂O₄ (x=0.0, 0.2, 0.4, 0.5, 0.6, 0.8) samples.

Sample	Lattice Constant a (Å)	Crystallite Size D (nm)	Strain ε	X-ray Density D_x (g/cc)	Mass Density D_m (g/cc)	Porosity P (%)
MnFe ₂ O ₄	8.4125	25.3476	0.0015	5.1450	2.2697	55.8850
Mn _{0.8} Ni _{0.2} Fe ₂ O ₄	8.4086	28.2393	0.0014	5.1689	2.4321	52.9467
Mn _{0.6} Ni _{0.4} Fe ₂ O ₄	8.3942	23.5324	0.0016	5.2124	2.4472	53.0508
Mn _{0.5} Ni _{0.5} Fe ₂ O ₄	8.3888	23.2204	0.0016	5.2309	2.3627	54.8307
Mn _{0.4} Ni _{0.6} Fe ₂ O ₄	8.3825	34.1861	0.0011	5.2511	2.6611	49.3230
Mn _{0.2} Ni _{0.8} Fe ₂ O ₄	8.3645	29.6192	0.0013	5.3021	2.5470	51.9631

The interplanar spacing ‘d’ and the lattice parameter ‘a’ were calculated using Bragg’s Condition (Equation-1) and (Equation-2) ^[11]

$$n\lambda = 2d \cdot \sin\theta \quad \text{Eq. [1]}$$

$$d = \frac{a}{\sqrt{h^2+k^2+l^2}} \quad \text{Eq. [2]}$$

The evolution of the lattice parameter of the Nickel-manganese spinel structure as a function of Nickel concentration is presented in figure 4.3. The lattice constant was found to decrease almost linearly from 8.412 nm to 8.364 nm with increasing Nickel Concentration obeying Vegard’s law. The result is in agreement with the earlier report ^[7]. This observed trend can be attributed to the difference in ionic radius of cations and the overall cation distribution within ferrite ^[6,7,9,12-16]. The chemical affinity of the Divalent and Trivalent cation towards tetrahedral (A) and octahedral (B) sites plays a significant role in determining the Lattice parameter. The B-site cations are $\sqrt{3}$ times more effective as compared to A-site in influencing the lattice constant ^[17]. The replacement of the Mn²⁺ ions having larger ionic radius (Tet: 0.655 Å; Oct: 0.80 Å) by Ni²⁺ ions having smaller ionic radius (Tet.: 0.55 Å; Oct.: 0.69 Å) ^[7,16,18] reduces the interatomic spacing ‘d’ which results in compression of lattice dimensions and hence the unit cell volume. A similar trend has been observed in previous studies when smaller ions are substituted in place of larger ions in different ferrite systems ^[6].

The crystallite size ‘D’ of each composition was calculated using Debye–Scherrer formula (Equation-3). The Crystallite strain ‘ε’ was determined using equation 4 ^[19,20].

$$D = \frac{0.9\lambda}{\beta \cos\theta} \quad \text{Eq. [3]}$$

$$\varepsilon = \frac{\beta}{4\cos\theta} \quad \text{Eq. [4]}$$

Here β denotes the full width at half maximum (FWHM) of the most intense peak (311) measured in radians and θ is the angle of diffraction. The Variation of Crystallite size and Crystallite strain is depicted in figure 4.4 and figure 4.5 respectively.

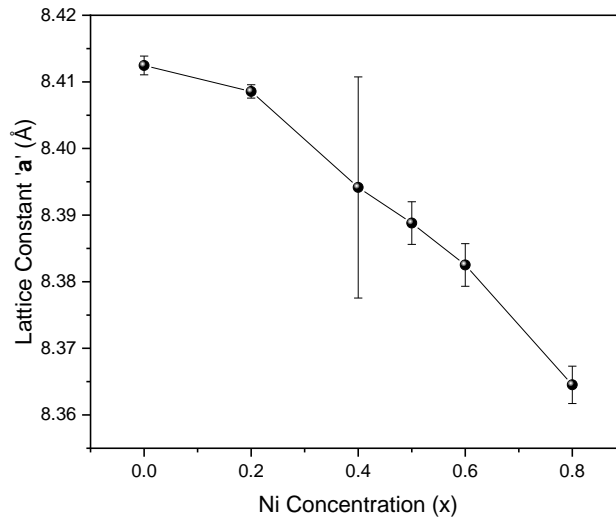


Figure 4.3 - Lattice Constant as function of Nickel concentration

It is evident that both the graphs show an exactly inverse trend. The variation in crystallite size was seen to exhibit an inverse trend with respect to the strain variation [19]. The overall crystallite size was found to increase with $\text{Mn}_{0.6}\text{Ni}_{0.4}\text{Fe}_2\text{O}_4$ and $\text{Mn}_{0.5}\text{Ni}_{0.5}\text{Fe}_2\text{O}_4$ concentrations showing smaller crystallite sizes. The overall increase in crystallite size is due to the complex systems of ferrites in which the nucleation and growth of the particles are expected to be influenced by the probability of the cations occupying the available sites and also by their affinity to these sites. According to the

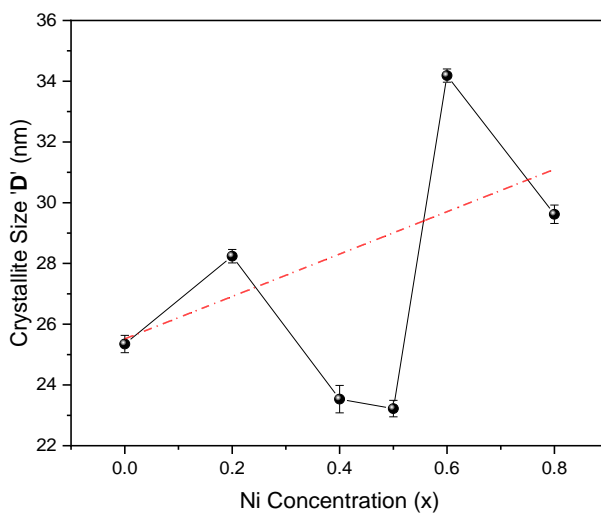


Figure 4.4 - Crystallite Size as a function of Ni Concentration

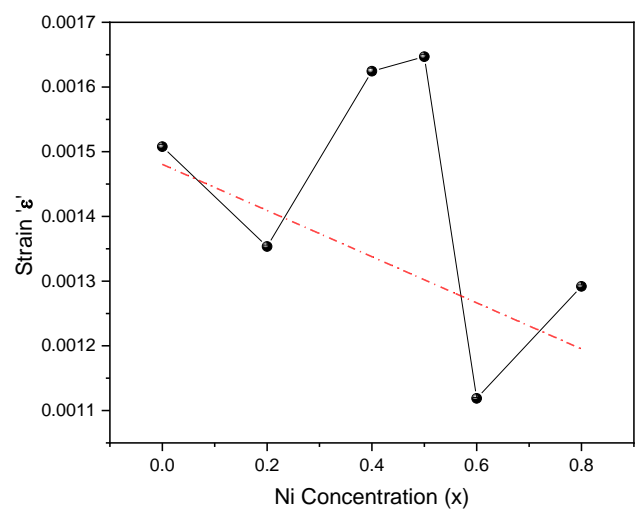


Figure 4.5 - Strain as a function of Ni Concentration

reports, the prime factors influencing crystallite size are ionic radius, cation distribution, preparation method, synthesis temperature and pH of the solution.

The cation distribution is in-turn influenced by various factors such as (a) Elastic energy (b) Madelung energy (c) crystal field stabilization energy (d) polarisation effects ^[21] (e) strong chemical affinity of certain cations to occupy either A- or B-sites and (f) the metastable cation distribution in ferrite nanoparticles ^[22]. In NiFe₂O₄, Ni²⁺ will preferentially occupy octahedral sites and force Fe³⁺ in the remaining octahedral and tetrahedral sites to balance the population between the two. The preference of Ni²⁺ ions for B-site is due to the favourable fit of the charge distribution of this ion in the crystal field of the octahedral site ^[23]. However, in the case of MnFe₂O₄, Mn²⁺ does not have that strong affinity towards tetrahedral sites only and a small fraction (>20%) can occupy octahedral sites. The overall Crystallite size increases with increasing Ni concentration because in MnFe₂O₄, Mn²⁺ cation can occupy any available site (A- or B-site) but in case of NiFe₂O₄, Ni²⁺ has more affinity towards B- site resulting in larger Crystallite size ^[22, 24].

The random trend of Crystallite size ranging from 23.22 nm to 34.19 nm can be attributed to the combined effect of all these competing parameters. Nasir et al. ^[25] also observed a random difference in the crystallite sizes in Mn_{1-x}Ni_xFe₂O₄ nanoparticles via sol-gel technique.

Density plays a major role in controlling the properties of polycrystalline ferrites. The X-ray density ‘D_X’ was computed using the following equation 5 ^[19,20].

$$D_X = \frac{8M}{N_A a^3} \quad \text{Eq. [5]}$$

where 8 is the number of formula units in a unit cell, N is the Avogadro’s number (6.0225 x 10²³atoms/mole), M is the molecular weight of the sample. It was found that the X-ray density increases with increasing Nickel concentration from 5.14 g/cc to 5.30 g/cc as shown in figure 4.6. The results were in agreement with the previous studies ^[12]. This feature can be attributed to the larger atomic weight of Nickel as compared to that of Manganese. Lattice constant also plays decisive role in X-ray density.

For calculating the Mass density, each sample was pressed into pellets of radius ‘R’ ~ 5 mm, thickness ‘t’, measured using a micrometre screw gauge in order to obtain mass and volume. The Mass density “D_M” of the materials was calculated using the following equation 6 ^[19,20].

$$D_M = \frac{M_g}{\pi R^2 t} \quad \text{Eq. [6]}$$

Where M_g is the mass of the pellet and (πR²t) is its volume.

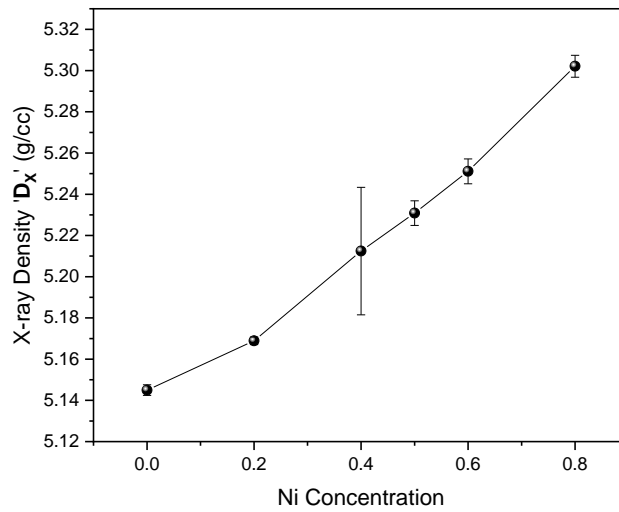


Figure 4.6 - X-ray density as a function of Ni Concentration

The porosity ‘P’ of the sample was analyzed using equation 7

$$P = 100 \left\{ 1 - \left(\frac{D_M}{D_X} \right) \right\} \quad \text{Eq. [7]}$$

Mass density depends on voids and pores created during the synthesis process, and porosity depends on the agglomeration and size of the particles [26]. The effect of the substitution of Ni ions on the mass density and porosity of manganese ferrite is shown in figure 4.7 and figure 4.8 respectively. A random trend has been observed in the case of mass density with $MnFe_2O_4$ having the lowest density and $Mn_{0.4}Ni_{0.6}Fe_2O_4$ having the highest density. The variation in Mass density is analogous to the inverse relation with the variation in porosity which is also observed by Sharmin Akhter et. al. [27].

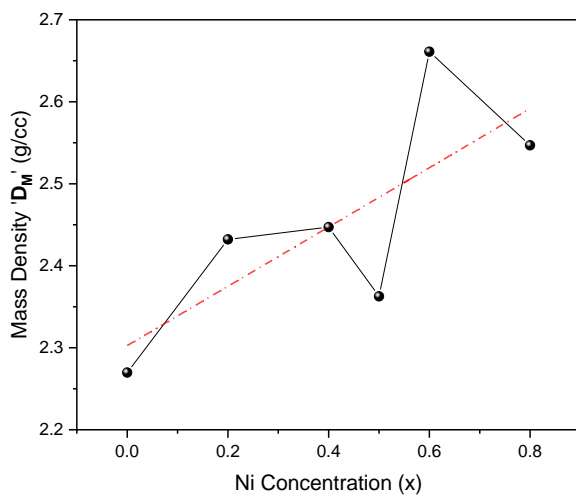


Figure 4.7 - Mass density as a function of Ni Concentration

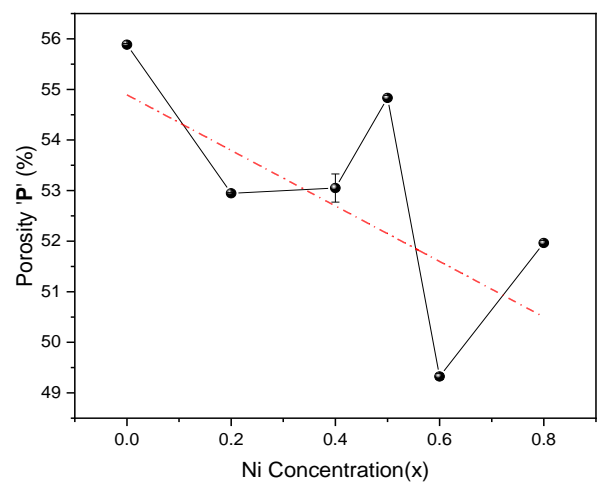


Figure 4.8 - Porosity as a function of Ni Concentration

The nonlinear random trend of mass density can be attributed to irregular grain growth, the chemical affinity of cations, and significant differences in atomic weights of the initial Manganese and doped Nickel cations [27, 28]. The overall increasing value of mass density can be attributed to the fact that replacing Mn^{2+} ions with a larger ionic radius by Ni^{2+} ions with a smaller ionic radius will decrease the volume of the vacancies in between the ions, thereby decreasing the porosity [29]. The overall decrease in porosity with increasing Ni^{2+} ions concentration, thereby gives an impression that Nickel might be helping in the densification of the materials. It is also observed that the overall mass density is lower than the corresponding X-ray density. This may be due to the formation of pores during the sample preparation process [28, 30].

4.2 Scanning Electron Microscope Analysis

The topographical study of all the prepared samples was conducted using Scanning electron microscopy as presented in figure 4.9. The SEM images indicated that the grain size of all the samples lies in nano regime. The grain size was analysed using image j software, and the histograms of grain size distribution along with SEM images are shown in figure 4.10. The average grain size of all the samples is shown in table 4.2.



Figure 4.9 - Carl Zeiss Scanning Electron Microscope

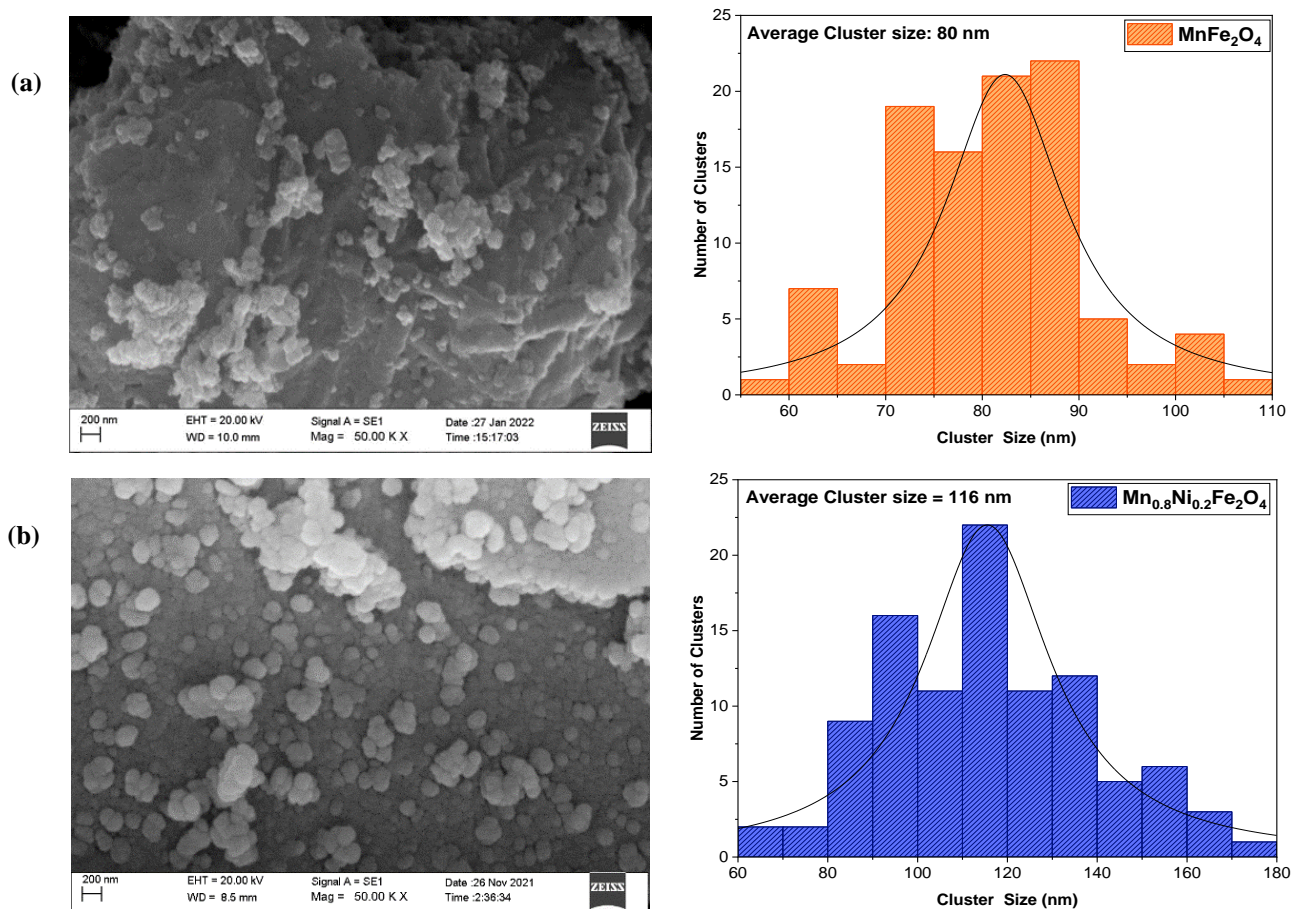


Figure 4.10 - Continued

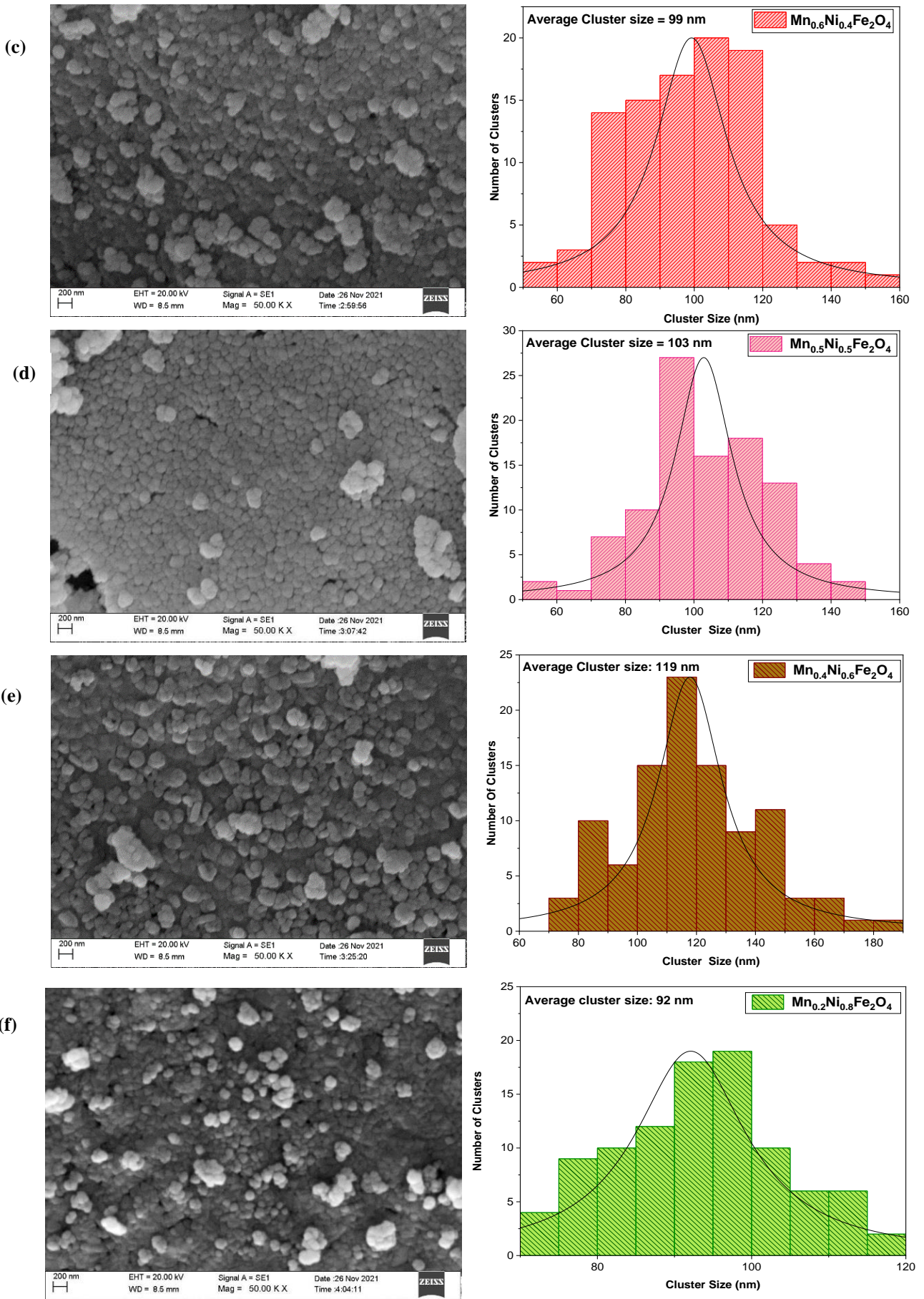


Figure 4.10 - SEM micrographs and their respective histograms of $\text{Mn}_{1-x}\text{Ni}_x\text{Fe}_2\text{O}_4$ [(a) $x = 0.0$, (b) $x=0.2$, (c) $x=0.4$, (d) $x=0.6$ and (e) $x=0.8$]

Table 4.3 - Cluster size of $Mn_{1-x}Ni_xFe_2O_4$

Concentration	0.0	0.2	0.4	0.5	0.6	0.8
Cluster Size (nm)	80	116	99	103	119	92

It is clearly visible that samples consist of almost spherical-shaped clusters of nanoparticles having fairly uniform size with narrow size distribution. Nanoparticles were found to be densely packed and uniformly distributed on the whole area. The formation of agglomerates is evident in some regions of the micrographs with irregular morphology constituted of quite fine particles. This feature can be attributed to the increase in the surface energy of the particles as their size is reduced to nano dimensions.

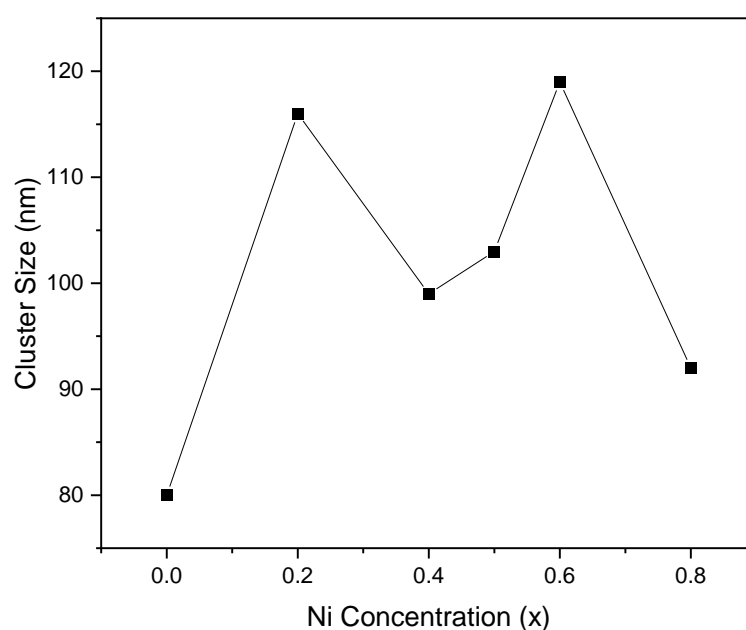


Figure 4.11 - Variation of Cluster size with increasing Ni concentration

An irregular trend in cluster size is observed as Ni concentration is increased as shown in figure 4.11 which was similar to the trend of crystallite size. Airimioaei et al. [31] and Shobana et al. [32] reported increase in particle size with increasing Ni ion concentration in Mn–Ni ferrites. However, S.K. Jesudoss et. al. [6] and B.V. Tirupanyam et al. [11] observed that the particle size decreases as Ni^{2+} ion concentration increases in Mn–Ni ferrites.

4.3 Energy-dispersive X-ray Spectroscopy Analysis

Energy-dispersive X-ray spectroscopy (EDX) is a surface analytical technique where an electron beam hits the sample, exciting an electron in an inner shell, causing its ejection and the formation of an electron hole in the electronic structure of the element. EDX provides useful information on the presence and distribution of different elements in the material under analysis. Chemical composition of the compounds was analysed by energy dispersive X-ray spectroscopy (EDX or EDS). The EDS spectra of the samples $Mn_{1-x}Ni_xFe_2O_4$ ($x = 0, 0.2, 0.4, 0.5, 0.6, 0.8$) are shown in figure 4.12.

Sample 1 - $MnFe_2O_4$

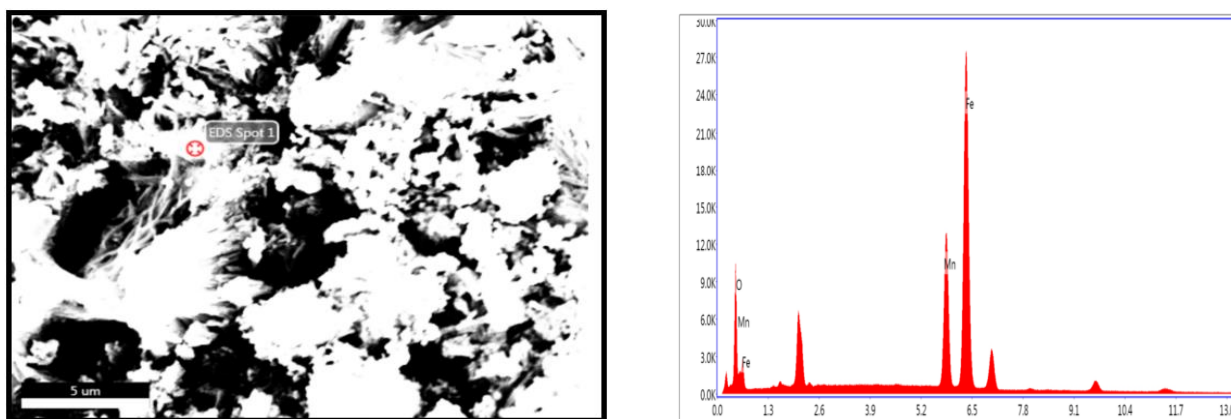


Figure 4.12 - (a) EDX image and EDX spectrum of $MnFe_2O_4$ nanoparticles

Molecular Weight of compound: 230.59

Table 4.4 - (a) Calculated and Observed Atomic percentage of Mn, Fe, O in $MnFe_2O_4$ nanoparticles using EDS data

Element	Molecular Wt. of element	Observed Atomic %	Calculated Composition	Expected Composition
O	15.99	14.56	2.10	4
Fe	55.84	61.91	2.56	2
Mn	54.94	23.53	0.99	1

Expected	$Mn_1Fe_2O_4$
Observed	$Mn_{0.99}Fe_{2.56}O_{2.10}$

Sample 2 - Mn_{0.8}Ni_{0.2}Fe₂O₄

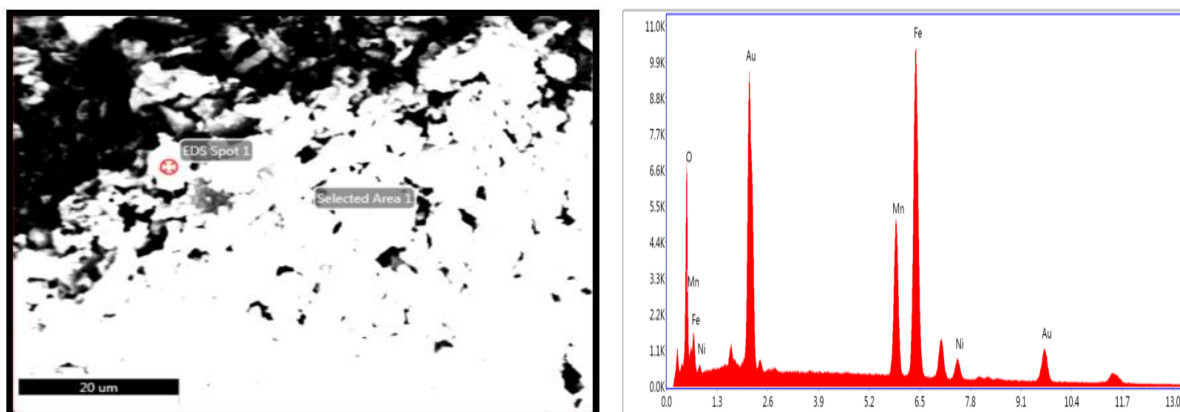


Figure 4.12 - (b) EDX image and EDX spectrum of Mn_{0.8} Ni_{0.2} Fe₂O₄ nanoparticles

Molecular Weight of compound: 231.3406

Table 4.4 - (b) Calculated and Observed Atomic percentage of Mn, Ni, Fe, O in Mn_{0.8} Ni_{0.2} Fe₂O₄ nanoparticles using EDS data

Element	Molecular Wt. of element	Observed Atomic %	Calculated Composition	Expected Composition
O	15.99	28.77	4.16	4
Fe	55.84	40.93	1.70	2
Ni	58.69	03.45	0.14	0.2
Mn	54.94	16.67	0.70	0.8

Expected	Mn _{0.8} Ni _{0.2} Fe ₂ O ₄
Observed	Mn _{0.70} Ni _{0.14} Fe _{1.70} O _{4.16}

Sample 3 - Mn_{0.6}Ni_{0.4}Fe₂O₄

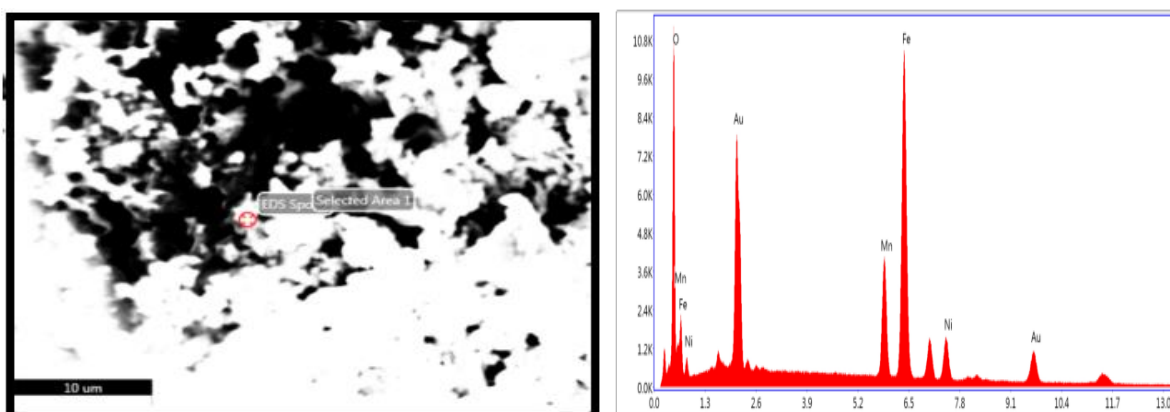


Figure 4.12 - (c) EDX image and EDX spectrum of Mn_{0.6} Ni_{0.4} Fe₂O₄ nanoparticles

Molecular Weight of compound: 232.0912

Table 4.4 - (c) Calculated and Observed Atomic percentage of Mn, Ni, Fe, O in Mn_{0.6}Ni_{0.4}Fe₂O₄ nanoparticles using EDS data

Element	Molecular Wt. of element	Observed Atomic %	Calculated Composition	Expected Composition
O	15.99	39.41	5.72	4
Fe	55.84	35.06	1.46	2
Ni	58.69	6.23	0.25	0.4
Mn	54.94	10.96	0.46	0.6

Expected	Mn _{0.6} Ni _{0.4} Fe ₂ O ₄
Observed	Mn _{0.46} Ni _{0.25} Fe _{1.46} O _{5.72}

Sample 4: Mn_{0.5}Ni_{0.5}Fe₂O₄

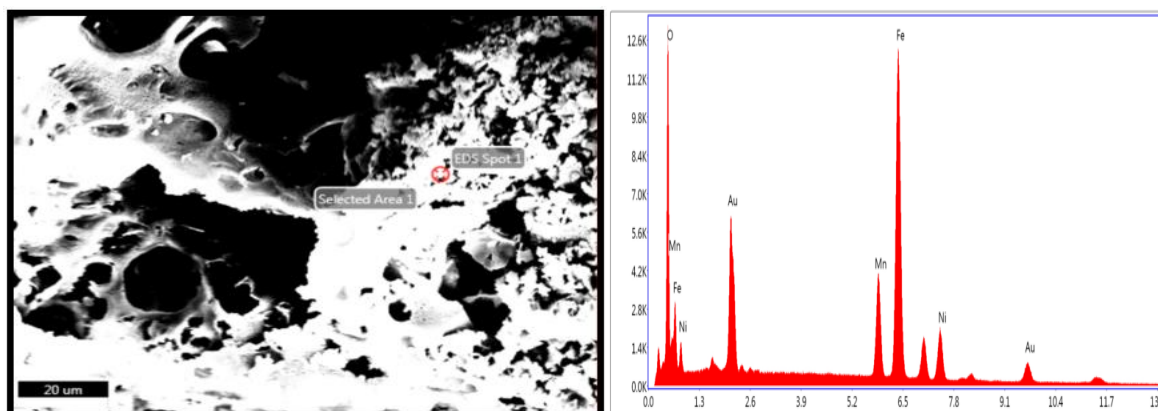


Figure 4.12 - (d) EDX image and EDX spectrum of Mn_{0.5}Ni_{0.5}Fe₂O₄ nanoparticles

Molecular Weight of compound: 232.4665

Table 4.4 – (d) Calculated and Observed Atomic percentage of Mn, Ni, Fe, O in Mn_{0.5}Ni_{0.5}Fe₂O₄ nanoparticles using EDS data

Element	Molecular Wt. of element	Observed Atomic %	Calculated Composition	Expected Composition
O	15.99	38.17	5.55	4
Fe	55.84	38.12	1.59	2
Ni	58.69	7.90	0.31	0.5
Mn	54.94	10.37	0.44	0.5

Expected	$Mn_{0.5}Ni_{0.5}Fe_2O_4$
Observed	$Mn_{0.44}Ni_{0.31}Fe_{1.59}O_{5.55}$

Sample 5: $Mn_{0.4}Ni_{0.6}Fe_2O_4$

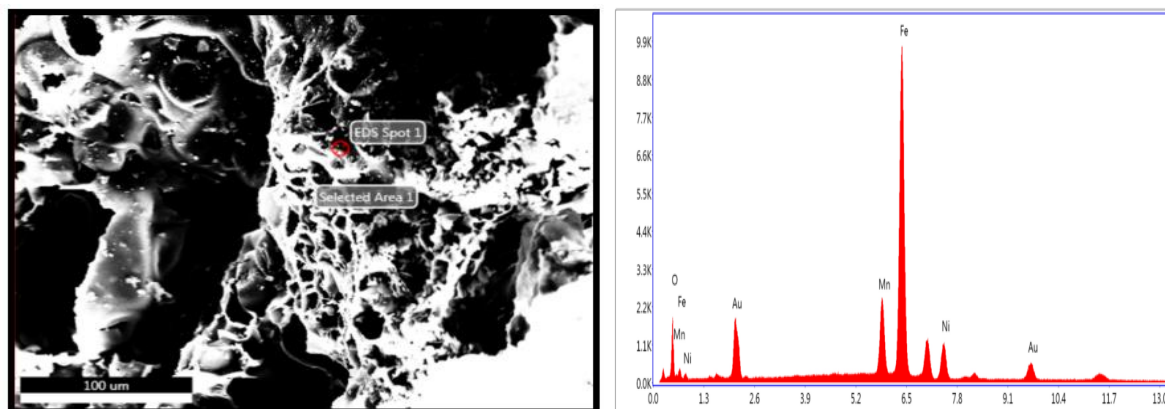


Figure 4.12 - (e) EDX image and EDX spectrum of $Mn_{0.4}Ni_{0.6}Fe_2O_4$ nanoparticles

Molecular Weight of compound: 232.8418

Table 4.4 – (e) Calculated and Observed Atomic percentage of Mn, Ni, Fe, O in $Mn_{0.4}Ni_{0.6}Fe_2O_4$ nanoparticles using EDS data

Element	Molecular Wt. of element	Observed Atomic %	Calculated Composition	Expected Composition
O	15.99	10.13	1.48	4
Fe	55.84	61.33	2.56	2
Ni	58.69	8.58	0.34	0.6
Mn	54.94	12.31	0.52	0.4

Expected	$Mn_{0.4}Ni_{0.6}Fe_2O_4$
Observed	$Mn_{0.52}Ni_{0.34}Fe_{2.56}O_{1.48}$

Sample 6: Mn_{0.2}Ni_{0.8}Fe₂O₄

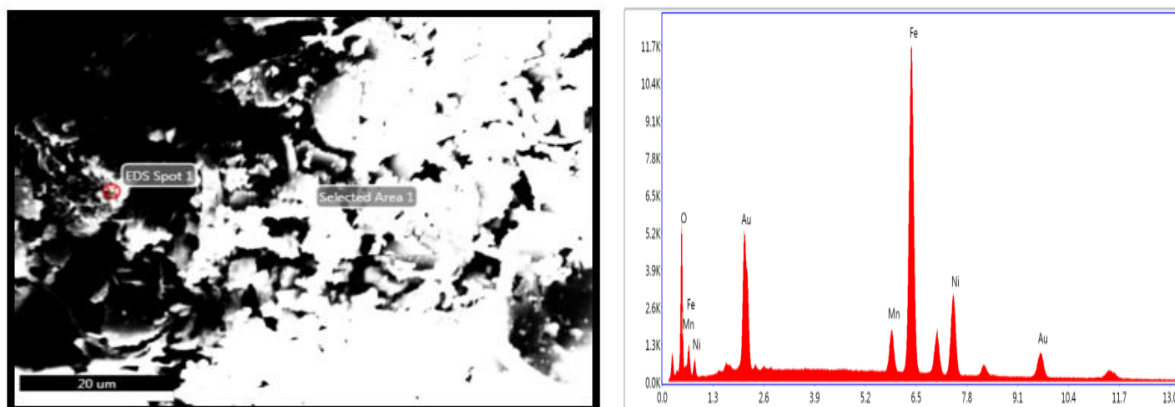


Figure 4.12 - (f) EDX image and EDX spectrum of Mn_{0.2} Ni_{0.8} Fe₂O₄ nanoparticles

Molecular Weight of compound: 233.5924

Table 4.4 – (f) Calculated and Observed Atomic percentage of Mn, Ni, Fe, O in Mn_{0.2} Ni_{0.8} Fe₂O₄ nanoparticles using EDS data

Element	Molecular Wt. of element	Observed Atomic %	Calculated Composition	Expected Composition
O	15.99	21.64	3.16	4
Fe	55.84	47.58	1.99	2
Ni	58.69	16.31	0.65	0.8
Mn	54.94	5.26	0.22	0.2

Expected	Mn _{0.2} Ni _{0.8} Fe ₂ O ₄
Observed	Mn _{0.22} Ni _{0.65} Fe _{1.99} O _{3.16}

EDS spectra of all the samples indicate the presence of desired elements such as Ni, Mn, Fe and O peaks which establishes the purity of the sample [9, 14, 33-40].

The occurrence of peak corresponding to Au is a result of sputtering process that is carried out in order to increase the surface conductivity during EDS measurements [33]. Observed and calculated atomic percentage are found to be in good agreement with permissible error limits indicating that stoichiometry is preserved during this method of sample preparation [9, 14, 33-40].

4.4 Vibrating Sample Magnetometer Analysis

The magnetic measurements of Nickel Substituted Manganese ferrite were performed using Lakeshore Vibrating sample magnetometer (VSM) as shown in figure 4.13. The experiment was conducted at room temperature with an applied field of 1T.



Figure 4.13 - Lakeshore Vibrating sample magnetometer

The hysteresis loop indicates the relationship between the intensity of magnetization \mathbf{M} and the applied magnetic field \mathbf{H} . Figure 4.14 shows the magnetization versus magnetic field data of the as-prepared $\text{Mn}_{1-x}\text{Ni}_x\text{Fe}_2\text{O}_4$ ($x= 0.0, 0.2, 0.4, 0.5, 0.6, 0.8$) samples recorded at room temperature. All the magnetic parameters such as Saturation Magnetisation (M_s), Retentivity (M_r), and Coercivity (H_c) are deduced from the hysteresis loops and are further used to compute the Magnetic moment (μ) and the Squareness ratio (M_r/M_s) of the respective samples and are listed in the table 4.5.

The M-H loops for the samples prepared at room temperature as shown in figure 4.14 reveals that the loops show a saturated hysteresis loop. The area under curve is small and the narrow loops obtained for the samples indicate that all samples are soft magnetic materials [6, 9, 12, 16, 34, 41-44]. This characteristic can be attributed to factors like chemical composition, cation distribution, microstructure, and canting angle which control the shape and width of the hysteresis curve [6, 9, 34, 45].

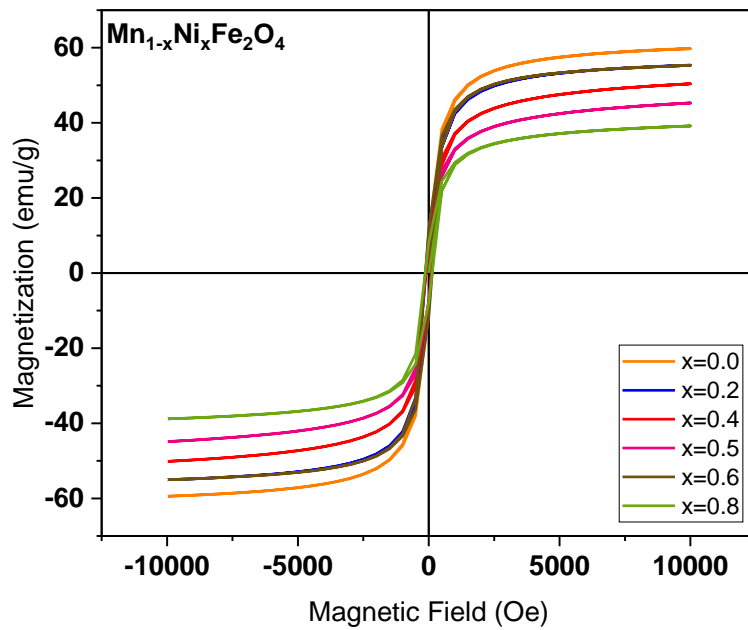


Figure 4.14 - Plots of Magnetic Hysteresis loops of $Mn_{1-x}Ni_xFe_2O_4$ ($x = 0.0, 0.2, 0.4, 0.5, 0.6, 0.8$) nanoparticles

It can be seen from figure 4.15 that the overall saturation magnetisation (M_S) decreases with an increase in Ni^{2+} concentration in $MnFe_2O_4$ nanoparticles. The variation in magnetisation of Mn Ni ferrite can be explained on the basis of Neel's molecular spin model which states that the cationic spins at the tetrahedral and the octahedral sites are arranged anti-parallel. The net magnetic moment of the lattice M_S is given by the algebraic sum of the spins, i.e.

$$M_S = |M_B - M_A| \quad \text{Eq [8]}$$

Where M_B and M_A are the magnetic moments of the octahedral and the tetrahedral sub-lattice respectively. According to the cation distribution of this model, ferromagnetic A-A and B-B interactions are weaker than antiferromagnetic A-B interaction [5, 14, 33, 34, 39, 41, 46, 47].

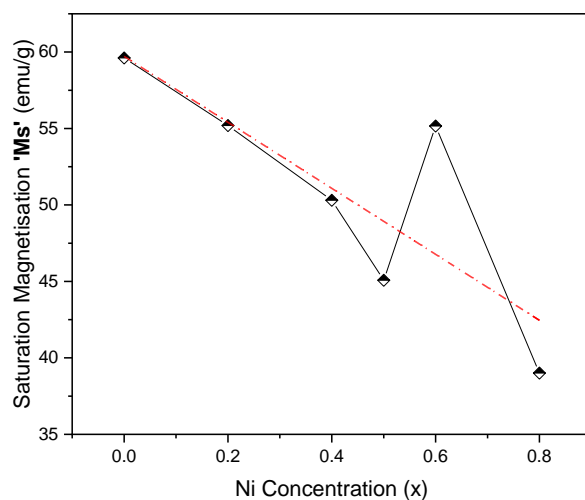


Figure 4.15 - Variation of Saturation Magnetization (M_S) with Nickel concentration (x)

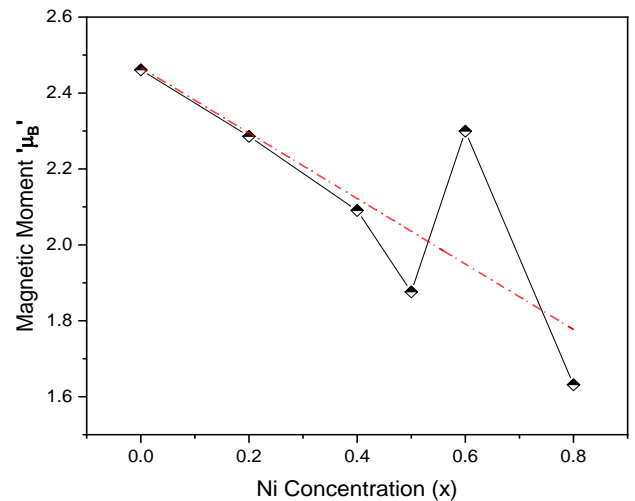


Figure 4.16 - Variation of Magnetic moment with Nickel concentration (x)

Ni²⁺ cations have magnetic moment of 2 μ_B whereas the Mn²⁺ cations have a much larger magnetic moment of 5 μ_B . In Mn-Ni, ferrites, Ni²⁺ ions are expected to occupy the octahedral (B) sites, while Mn²⁺ ions are randomly distributed between tetrahedral (A) and octahedral (B) sites as discussed in previous section. Substituting Ni²⁺ ion with an Mn²⁺ ion, the atomic magnetic moment decreases from 5 μ_B to 2 μ_B thus the increase of the Ni²⁺ cation and reduction of Mn²⁺ cation results in mixed ferrite with reduced effective saturation magnetisation [5, 9, 10, 13, 14, 16, 33, 34, 39, 42, 46-48].

Table 4.5 - Magnetic properties: Saturation Magnetisation (M_s), Retentivity (M_r), Coercivity (H_c), Magnetic Moment(μ), Squareness Ratio (M_{rs}) of Mn_{1-x}Ni_xFe₂O₄ (x = 0.0, 0.2, 0.4, 0.5, 0.6 & 0.8) nanoparticles

Sample Mn _{1-x} Ni _x Fe ₂ O ₄	Saturation Magnetisation M _s (emu/g)	Retentivity M _r (emu/g)	Coercivity H _c (Oe)	Magnetic moment μ (μ_B)	Squareness Ratio M _{rs}
MnFe ₂ O ₄	59.61	10.45	113.33	2.46	0.175
Mn _{0.8} Ni _{0.2} Fe ₂ O ₄	55.19	09.76	113.61	2.29	0.177
Mn _{0.6} Ni _{0.4} Fe ₂ O ₄	50.31	07.36	102.29	2.09	0.146
Mn _{0.5} Ni _{0.5} Fe ₂ O ₄	45.08	07.50	114.61	1.88	0.166
Mn _{0.4} Ni _{0.6} Fe ₂ O ₄	55.16	11.74	129.98	2.30	0.213
Mn _{0.2} Ni _{0.8} Fe ₂ O ₄	39.01	07.96	134.56	1.63	0.204

The Mn²⁺ and Fe³⁺ magnetic moments are approximately the same (5 μ_B). The enhancement in saturation magnetisation at the nickel concentration of x=0.6 can be attributed to the cationic arrangements over the tetrahedral site and the octahedral site [5, 6, 9, 10, 13, 14, 19, 34, 39, 41, 46, 47].

Some other parameters affecting variation in saturation magnetisation are particle size, chemical composition, sample density, surface area, defects, spin canting, microstructure, morphology etc. [5-7, 10, 13, 16, 35, 37, 43, 45, 47-49].

The magnetic moment (μ) per unit formula in Bohr magneton and was calculated from saturation magnetization by using the following formula [9, 19, 34, 39, 41].

$$\mu = \frac{M_w M_s}{N_A \mu_B} \quad \text{Eq. [9]}$$

where

M_w = Molecular weight of a particular ferrite composition

M_s = Saturation magnetization (emu/g)

N_A = Avogadro's Number

μ_B = Bohr Magnetron

The overall magnetic moment per formula unit decreases with the increasing Ni content as depicted in figure 4.16 which evidently explains the variation in M_s as the ratio of M_s/μ is nearly constant [14, 19, 34, 49].

From the Graph of coercivity v/s Ni concentration (Figure 4.17), the overall Coercivity (H_c) was found to increase with an increase in Ni^{2+} concentration in $MnFe_2O_4$ nanoparticles. The coercivity is found to be in the range of 102.29–134.56 Oe indicating soft ferrite nature [42, 44]. The variations in the trend may be attributed to domain structure, critical diameter, lattice strain, spin–orbit coupling at the tetrahedral (A) and octahedral (B) sites, shape anisotropy and magneto crystalline anisotropy of the crystal [9, 12, 16, 41, 45].

The magnetization (M_s) is related to the coercivity through Brown's relation.

$$H_c = \frac{2K_1}{\mu_0 M_s} \quad \text{Eq. [10]}$$

Where K is the effective magnetic anisotropy constant which reveals the energy required to rotate the magnetic moment inside the particle and μ_0 is permittivity of free space [6, 9, 35, 39, 41]. According to this equation, the coercivity (H_c) is inversely proportional to magnetization (M_s), which is in fairly good agreement with our experimental results [6, 39, 41].

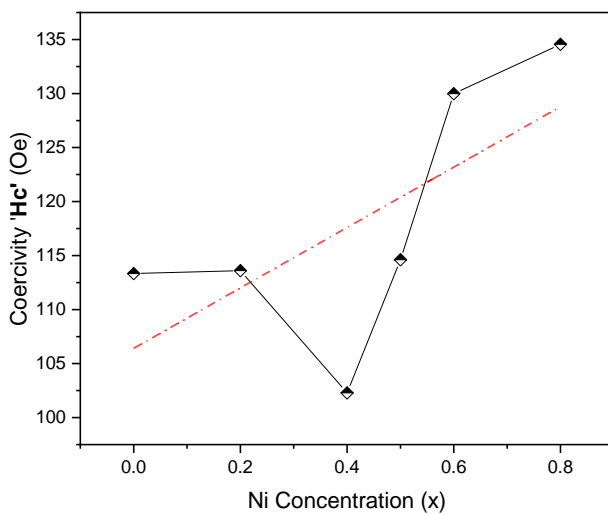


Figure 4.17 - Variation of Coercivity (H_c) with Nickel concentration (x)

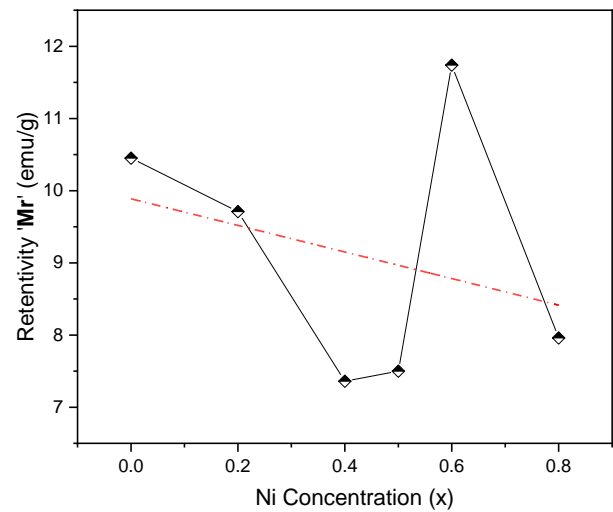


Figure 4.18 - Variation of Retentivity (M_r) with Nickel concentration (x)

The presence of Ni²⁺ ions in the octahedral (B) site has an impact on the magnitude of the effective magnetic anisotropy [6, 12, 45]. The effective magnetic anisotropy and hence coercivity (H_c) increases with an increase in the Ni²⁺ concentration in the Mn-Ni ferrite nanoparticles [6, 35, 41, 45] and finally it reaches the maximum value at higher concentration of Ni²⁺ ions at x=0.8.

The overall retentivity decreases with increase in nickel concentration as seen in figure 4.18 which is in well agreement with previous reports [6, 33]. Mr varies between 7.36 and 11.74 emu/g. Nickel concentration x=0.6 can be correlated to the minimum crystallite strain which signifies that the spins are reluctant to move from their easy axis of magnetisation. These alterations in retentivity values are seen because of cationic distribution.

The squareness ratio is a measure of how square the hysteresis loop is [45]. The magnitudes of squareness ratio (M_{RS}) of the Mn_{1-x}Ni_xFe₂O₄ cubic spinel ferrites were calculated by the following equation [34, 41].

$$M_{RS} = \frac{M_R}{M_S} \quad \text{Eq [11]}$$

The squareness ratio determines the domain state. It can be used to distinguish between single domain, multidomain, and pseudo-single domains. According to the reports theoretical value of M_R/M_S lower than 0.5 indicates the presence of non-interacting uniaxial single domain particle. [34, 45]. In single domain systems, the magnetic anisotropy determines the spin alignment along the easy axis of magnetisation and thermal fluctuations cause these spins to undergo Brownian like motion along their axis [35].

The squareness ratio of the synthesized materials in the current work is less than 0.5, thus indicating that the particles were heading towards single domain magnetic nanoparticles.

4.5 References

- [1] S. Sharifi, A. Yazdani and K. Rahimi. 2020. "Incremental substitution of Ni with Mn in NiFe₂O₄ to largely enhance its supercapacitance properties." Scientific reports (Nature search) 1-15. doi: [10.1038/s41598-020-67802-z](https://doi.org/10.1038/s41598-020-67802-z).
- [2] M. T. Hossain, S. Islam, M. H. Mondala and A. H. Khan. 2006. "Studies on Anomalous Behaviour at Curie Point, T_c of Some Classes of Mixed Ferrites." Bangladesh Journal of Scientific and Industrial Research (Bangladesh Journals Online) 41 (3): 171-180. doi: 10.3329/bjsir.v41i3.287.
- [3] M.A. Kassem, A. AbuEl-Fadl, A.M. Hassan, A.M.Gismelssed and H. Nakamura. 2021. "Structure and cationic distribution dependent soft magnetic properties of single-domain Mg_{1-x}Ni_xFe₂O₄ (0 ≤ x ≤ 1.0) nanocrystals." Materials Science & Engineering B (Elsevier) 274: 1-11. doi: 10.1016/j.mseb.2021.115494.
- [4] P. Thakur, D.Chahara, S. Tanejaa, N. Bhallabd and A. Thakur. 2020. "A review on MnZn ferrites: Synthesis, characterization and applications." Ceramics International (Elsevier) 46 (10): 15740-15763. doi: 10.1016/j.ceramint.2020.03.287
- [5] Aakash, R. Choubey, D. Das, S. Mukherjee. 2016. "Effect of doping of manganese ions on the structural and magnetic properties of nickel ferrite." Journal of Alloys and Compounds (Elsevier) 1-26. doi: 10.1016/j.jallcom.2016.01.198.
- [6] S.K.Jesudossa, J. J. Vijayaa, L. J. Kennedy, P. I. Rajan, H. A.Al-Lohedan, R. J. Ramalingam, K. Kaviyarasude, M. Bououdina. 2016. "Studies on the efficient dual performance of Mn_{1-x}Ni_xFe₂O₄ spinel nanoparticles in photodegradation and antibacterial activity." Journal of Photochemistry and Photobiology B: Biology (Elsevier) 165: 121-132. doi: 10.1016/j.jphotobiol.2016.10.004.
- [7] A. Hussain, T. Abbas, S.B. Niazib. 2012. "Preparation of Ni_{1-x}Mn_xFe₂O₄ ferrites by sol-gel method and study of their cation distribution." Ceramics International (Elsevier) 39 (2): 1221-1225. doi: 10.1016/j.ceramint.2012.07.049.
- [8] H. Ghayour, M. Abdellahi, N. Ozada, S. Jabbrzare and A. Khandan. 2017. "Hyperthermia application of zinc doped nickel ferrite nanoparticles." Journal of Physics and Chemistry of Solids (Elsevier) 111: 464-472. doi: 10.1016/j.jpcs.2017.08.018.

- [9] K. Sasikumar, R. Bharathikannan, G. Sujithkumar, S. Raja, G. Johnsy Arputhavalli, M. Vidhya, R. Marnadu and R. Suresh. 2021. “Structural, Optical, and Magnetic Properties of Mn-Doped Nickel Ferrite ($\text{Ni}_{1-x}\text{Mn}_x\text{Fe}_2\text{O}_4$) Thin Films Deposited by Jet Nebulizer Spray Pyrolysis Technique.” *Journal of Superconductivity and Novel Magnetism (Springer Link)* 2189–2198. doi: 10.1007/s10948-021-05948-1.
- [10] T. F. Marinca, I. Chicinaş, O. Isnard, B. V. Neamţu. 2015. “Nanocrystalline/nanosized manganese substituted nickel ferrites – $\text{Ni}_{1-x}\text{Mn}_x\text{Fe}_2\text{O}_4$ obtained by ceramic-mechanical milling route.” *Ceramics International (Science Direct)* 42 (4): 1-45. doi: 10.1016/j.ceramint.2015.11.155.
- [11] B.V.Tirupanyama, Ch.Srinivas, S.S.Meena, S.M.Yusuf, A.S. Kumar, D.L. Sastrye, V. Seshubaif. 2015. “Investigation of structural and magnetic properties of co-precipitated Mn–Ni ferrite nanoparticles in the presence of $\alpha\text{-Fe}_2\text{O}_3$ phase.” *Journal of Magnetism and Magnetic materials (Elsevier)* 392: 101-106. doi: 10.1016/j.jmmm.2015.05.010.
- [12] R. Kesavamoorthi, C. R. Raja. 2016. “Studies on the Properties of Manganese Substituted Nickel Ferrite Nanoparticles.” *Journal of Superconductivity and Novel Magnetism (Springer Link)* 29: 2729–2734. doi:10.1007/s10948-016-3792-8.
- [13] Jian-Jun Gu, Li-Hu Liu, Yun-Kai Qi, Qin Xu, and Hui-Yuan Sun. 2011. “Synthesis and Magnetic Characterization of Nickel Ferrite Nanowire Arrays Doped with Manganese.” *Advance material research* 233-235: 1799-1802.
- [14] S. Mirzaee, Y. Azizian-Kalandaragh, P. Rahimzadeh. 2019. “Modified co-precipitation process effects on the structural and magnetic properties of Mn- doped nickel ferrite nanoparticles.” *Solid State Sciences (Elsevier)* 99: 1-24. doi:10.1016/j.solidstatesciences.2019.106052.
- [15] H.E.Hassan, T.Sharshar, M.M.Hessien, O.M.Hemeda. 2013. “Effect of γ -rays irradiation on Mn–Ni ferrites: Structure, magnetic properties and positron annihilation studies.” *Nuclear Instruments and Methods in Physics Research Section B: Beam Interactions with Materials and Atoms (Elsevier)* 304: 72-79. doi: 10.1016/j.nimb.2013.03.053.
- [16] Y. Köseoğlu, 2012. “Structural, magnetic, electrical and dielectric properties of $\text{Mn}_x\text{Ni}_{1-x}\text{Fe}_2\text{O}_4$ spinel nanoferrites prepared by PEG assisted hydrothermal method.” *Ceramics International* 39 (4). doi:10.1016/j.ceramint.2012.11.004.
- [17] R. Iyer, R. Desai, R. V. Upadhyay. 2008. “Low temperature synthesis of nanosized $\text{Mn}_{1-x}\text{Zn}_x\text{Fe}_2\text{O}_4$ ferrites and their characterizations.” *Indian Journal of Pure and Applied Physics (Research Gate)* 32 (2): 141-147. doi:10.1007/s12034-009-0021-0.

- [18] Q. Wei, J.B. Li & Y.J. Chen. 2001. "Cation distribution and infrared properties of $\text{Ni}_x\text{Mn}_{1-x}\text{Fe}_2\text{O}_4$ ferrites." *Journal of Materials Science (Springer Link)* 36: 5115–5118. doi:10.1023/A:1012473207424.
- [19] P. P. Naik, R.B. Tangsali, S.S. Meena, S.M. Yusuf. 2017. "Influence of rare earth (Nd^{3+}) doping on structural and magnetic properties of nanocrystalline manganese-zinc ferrite." *Materials Chemistry and Physics (Elsevier)* 191: 215-224. doi:http://dx.doi.org/10.1016/j.matchemphys.2017.01.032.
- [20] D. V. Kurnude, R. S. Barkule, A. V. Raut, D. R. Shengule and K. M. Jadhav. 2013. "X-Ray Diffraction and Cation Distribution Studies in Zinc-Substituted Nickel Ferrite Nanoparticles." *Journal of Superconductivity and Novel Magnetism (Springer Link)* 27 (2): 547–553. doi:10.1007/s10948-013-2305-2.
- [21] R. Valenzuela, 2012. "Novel Applications of Ferrites." *Physics Research International (Hindawi Publishing Corporation)*. doi:10.1155/2012/591839.
- [22] C. Rath, R. P. Das, K.K. Sahu, S.D. Kulkarni, S.D. Date, N. C. Mishra. 2002. "Dependence on cation distribution of particle size, lattice parameter and magnetic properties in nanosize Mn–Zn ferrite." *Journal of Applied Physics (AIP Publishing)* 91: 2211-2215. doi:10.1063/1.1432474.
- [23] M. Siddique, N. M. Butt, M. Shafi, T. Abbas & I. Misbah. 2003. "Cation distribution in Ni-substituted Mn-ferrites by Mössbauer technique." *Journal of Radioanalytical and Nuclear Chemistry (Springer Nature)* 258: 525–529. doi:10.1023/B:JRNC.0000011746.68066.f5.
- [24] J. P. Chen, C. M. Sorensen, K. J. Klabunde, G. C. Hadjipanayis, E. Devlin, and A. Kostikas. 1996. "Size-dependent magnetic properties of MnFe_2O_4 fine particles synthesized by coprecipitation." *Phys. Dev. B. (American Physical Society)* 54 (13): 9288-9296. doi:10.1103/PhysRevB.54.9288.
- [25] S. Nasir, G. Asghar, M. A. Malik & M. A.Rehman. 2011. "Structural, dielectric and electrical properties of zinc doped nickel nanoferrites prepared by simplified sol–gel method." *Journal of Sol-Gel Science and Technology (Springer Nature)* 59: 111–116. doi:10.1007/s10971-011-2468-x.
- [26] D. Ahmad, N. Mehboob, A. Zaman, N. Ahmed, K. Ahmed, M. Mushtaq, K. Althubeiti, A. Ali, F. Sultana and K. Bashir. 2021. "Synthesis and Characterization of Ce^{3+} -Doped $\text{Ni}_{0.5}\text{Cd}_{0.5}\text{Fe}_2\text{O}_4$ Nanoparticles by Sol–Gel Auto-Combustion Method." *Coatings (MDPI)* 11 (10): 1-12. doi:10.3390/coatings11101156.

- [27] S. Akhter, P. Roy, A. Anwar, , M. A. Hossain, M. N. I. Khan, S. S. Sikder. 2020. "Effect of Y³⁺ Substitution on Structural and Magnetic Properties of Ni_{0.25} Zn_{0.75}Y_xFe_{2-x}O₄." Dhaka University Journal of Science (Bangladesh Journals Online) 68 (2): 111-116. doi:10.3329/dujs.v68i2.54607.
- [28] Dahham, N.A. 2018. "Influence of cobalt substitution on the properties of Ni_{0.95-x}CoxCu_{0.05}Fe₂O₄ ferrite nanoparticles." Iraqi Journal of Physics (University of Baghdad) 16 (38): 42-55. doi:10.20723/ijp.16.38.42-55.
- [29] C. Aziz, B. Azhdar. 2022. "Synthesis of dysprosium doped cobalt ferrites nanoparticles by solgel auto-combustion method and influence of grinding techniques on structural, Morphological, and magnetic properties." Journal of Magnetism and Magnetic Materials (Elsevier) 542: 1-12. doi:10.1016/j.jmmm.2021.168577.
- [30] A. Poddar, S. Halder , S.I. Liba, S. M. Hoque and S.S. Sikder. 2022. "Study of the Effect of Quenching on Microstructural and Magnetic Properties of Cu-Doped Mg-Ferrite." Advances in Condensed Matter Physics (Hindawi) 2022: 1-10. doi:10.1155/2022/3354087.
- [31] M. Airimioaei, C.E. Ciomaga, N. Apostolescu, L. Leontie, A.R. Iordana, L. Mitoseriub, M.N. Palamaru. 2011. "Synthesis and functional properties of the Ni_{1-x}MnxFe₂O₄ ferrites." Journal of Alloys and Compounds (Elsevier) 509 (31): 8065–8072. doi: 10.1016/j.jallcom.2011.05.034.
- [32] M.K. Shobana, S. Sankar. 2009. Journal of Magnetism and Magnetic Materials (Elsevier) 321 (14): 2125-2128. doi:10.1016/j.jmmm.2009.01.046.
- [33] G. Mathubala, A. Manikandan,S. Arul Antony,P. Ramar. 2016. "Photocatalytic degradation of methylene blue dye and magneto-optical studies of magnetically recyclable spinel Ni_xMn_{1-x}Fe₂O₄ (x=0.0-1.0) nanoparticles." journal of Molecular Structure (Elsevier) 79-87. doi: [10.1016/j.molstruc.2016.02.032](https://doi.org/10.1016/j.molstruc.2016.02.032).
- [34] C. Sedrati, S. Alleg,H. Boussafel,A. Hacine. 2021. "Structure and magnetic properties of nickel ferrites synthesized by a facile co-precipitation method: effect of the Fe/Ni ratio." Journal of Materials Science 24549-24559. doi: [10.1007/s10854-021-06932-0](https://doi.org/10.1007/s10854-021-06932-0).
- [35] K. Maaz, J.L. Duan, S. Karim, Y.H. Chen, P.F. Zhai, L.J. Xu, H.J. Yao, J. Liu. 2016. "Fabrication and size dependent magnetic studies of Ni_xMn_{1-x}Fe₂O₄ (x = 0.2) cubic nanoplates." Journal of Alloys and Compounds 1-11. doi: [10.1016/j.jallcom.2016.05.246](https://doi.org/10.1016/j.jallcom.2016.05.246).

- [36] P. Koli, K. Kapadnis, and U. Deshpande. 2019. "Nanocrystalline modified nickel ferrite films: an effective sensor for industrial and environmental gas pollutant detection." *Journal of Nanostructure in Chemistry* (Springer). doi: [10.1007/s40097-019-0300-2](https://doi.org/10.1007/s40097-019-0300-2).
- [37] R. E. Kumar, A. S. Kamzin, T. Prakash. 2014. "Effect of particle size on structural, magnetic and dielectric properties of manganese substituted nickel ferrite nanoparticles." *Journal of Magnetism and Magnetic Materials* (ELSEVIER) 389-396. doi: [10.1016/j.jmmm.2014.11.019](https://doi.org/10.1016/j.jmmm.2014.11.019).
- [38] R. Pazik, E. Zachanowicz, B. Poźniak, M. Małecka, A. Zięcina and L. Marciniak. 2017. "Non-contact Mn_{1-x}Ni_xFe₂O₄ ferrite nano-heaters for biological applications – heat energy generated by NIR irradiation." *Royal Society of Chemistry* 18162–18171. doi: [10.1039/c7ra01904a](https://doi.org/10.1039/c7ra01904a).
- [39] R.S. Pandav, R.P. Patil, S.S. Chavan, I.S. Mulla, P.P. Hankare. 2016. "Magneto-structural studies of sol-gel synthesized nanocrystalline manganese substituted nickel ferrites." *Journal of Magnetism and Magnetic Materials* doi: [10.1016/j.jmmm.2016.04.090](https://doi.org/10.1016/j.jmmm.2016.04.090).
- [40] S. Yuvaraj, N. Manikandan, G. Vinitha. 2018. "Structural and nonlinear optical properties of nickel substituted manganese ferrite nanoparticles." *Ceramics International* 34-39. doi: [10.1016/j.ceramint.2018.09.033](https://doi.org/10.1016/j.ceramint.2018.09.033).
- [41] A. A. Ati, A. H. Abdalsalam, A.S. Hassan. 2021. "Thermal, microstructural and magnetic properties of manganese substitution cobalt ferrite prepared via co-precipitation method." *J Mater Sci: Mater Electron* 3020-3037. doi: [10.1007/s10854-020-05053-4](https://doi.org/10.1007/s10854-020-05053-4).
- [42] K. P. Chae, W. O. Choi, J. Lee, B.S. Kang, and S. H. Choi. 2013. "Crystallographic and Magnetic Properties of Nickel Substituted Manganese Ferrites Synthesized by Sol-gel Method." *Journal of Magnetism*. doi: [10.4283/JMAG.2013.18.1.021](https://doi.org/10.4283/JMAG.2013.18.1.021).
- [43] W. Wang, Z. Ding, X. Zhao. 2015. "Microstructure and magnetic properties of MFe₂O₄ (M = Co, Ni, and Mn) ferrite nanocrystals prepared using colloid mill and hydrothermal method." *Journal Of Applied Physics*. doi: [10.1063/1.4917463](https://doi.org/10.1063/1.4917463).
- [44] E. Ranjit Kumar, R. Jayaprakash, and S. Kumar. 2013. "Effect of annealing temperature on structural and magnetic properties of manganese substituted NiFe₂O₄ nanoparticles." *Materials Science in Semiconductor Processing* 173-177. doi: [10.1016/j.mssp.2013.09.003](https://doi.org/10.1016/j.mssp.2013.09.003).
- [45] T. Dippong, E. A. Levei, I. G. Deac, I. Petean, O. Cadar. 2022. "Dependence of Structural, Morphological and Magnetic Properties of Manganese Ferrite on Ni-Mn Substitution." *International Journal of Molecular Sciences* 1-15. doi: [10.3390/ijms23063097](https://doi.org/10.3390/ijms23063097).
- [46] P.P. Naik, R.B. Tangsali, B. Sonaye, S. Sugur. 2015. "Radiation induced structural and magnetic transformations in nanoparticle Mn_xZn_(1-x)Fe₂O₄ ferrites." *Journal of Magnetism and Magnetic Materials* 377-385. doi: [10.1016/j.jmmm.2015.03.032](https://doi.org/10.1016/j.jmmm.2015.03.032).

- [47] S. Thota, S. C.Kashyap, S. K.Sharma,V.R. Reddy. 2016. "Micro Raman, Mossbauer and magnetic studies of manganese substituted zinc ferrite nanoparticles: Role of Mn." Journal of Physics and Chemistry of Solids 136-144. doi: [10.1016/j.jpcs.2015.12.013](https://doi.org/10.1016/j.jpcs.2015.12.013).
- [48] J. Hua, H. Qina,Y. Wang, Z. Wang,S. Zhang. 2000. "Magnetic properties and magnetoresistance effect of Ni_{1-2x}Mn_xFe₂O₄ sintered ferrites." Solid State Communications 233-235.
- [49] K. Zhou, Q. Liqin, W. Xuehang, W. Wenwei, S. Yuexiao, T. Yulin, and L. Jieyue. 2014. "Structure and magnetic properties of manganese-nickel ferrite with lithium substitution." Ceramics International 1-23. doi: [10.1016/j.ceramint.2014.09.052](https://doi.org/10.1016/j.ceramint.2014.09.052).

CHAPTER V: CONCLUSION

The nanocrystalline Nickel doped Manganese ferrite with composition $Mn_{1-x}Ni_xFe_2O_4$ ($x = 0.0, 0.2, 0.4, 0.5, 0.6, 0.8$) were successfully prepared using combustion method. All the samples were found to exhibit mixed spinel structure with lattice constant ranging between 8.4125 \AA to 8.3645 \AA . The overall crystallite size was seen to increase with increasing Ni concentrations which is attributed to smaller ionic radii of Ni^{+2} ion reducing the strain in ferrite structure. The mass density was seen to increase with increasing Ni concentration. The surface morphology studied using SEM micrographs revealed the formation of spherical particles with agglomerations. The EDS spectra of the nano samples show only Ni, Mn, Fe and O peaks revealing no impurities in the samples. The observed compositions were in good agreement to that of the theoretical stoichiometric calculations indicating that the method of sample preparation employed in the present work preserves the material/samples stoichiometry. The saturation magnetisation was found to decrease with increase in nickel concentration which can be attributed to the cationic distribution between tetrahedral and octahedral sites. The low value of coercivity confirms that prepared ferrites are of soft nature. The squareness ratio of the synthesized materials in the current work was found to be much below 0.5, thus indicating that the prepared ferrites exhibit single domain magnetic nanoparticles.

FUTURE SCOPE

Apart from the magnetic properties, ferrites have been considered as efficient electrodes for next generation energy storage devices. The spinel ferrites such as $MnFe_2O_4$, $CoFe_2O_4$, $ZnFe_2O_4$ and $NiFe_2O_4$ are being relentlessly being explored for the applications like supercapacitors and photovoltaics. The poor electrical conductivity is the main limitation to be used them in fast charging/discharging supercapacitor. However mixed ferrites such as Mn-Ni ferrite are still not adequately explored. In ferrites, the charge storage arises from the fast-reversible surface redox reactions at the electrode/electrolyte interface. In particular, the electrode material with high specific capacitance, wide range of operating potential, low synthesis cost and its availability on the earth are highly desirable to fabricate a supercapacitor. Ferrites with mixed oxidation states have proved as promising electrodes in supercapacitors. Hence one can measure electrical transport properties along with electrochemical properties of Ni doped Mn ferrite to investigate the potential candidature of this material in the field of supercapacitors. Also the effect of composite preparation of these materials with graphene oxide may be investigated.